CORRELATION IN THE ONE DIMENSIONAL ELECTRON GAS

BY

LUKE NATHAN SHULENBURGER

B.S., Massachusetts Institute of Technology, 2002
B.S., Massachusetts Institute of Technology, 2002
M.S., University of Illinois at Urbana-Champaign, 2004

DISSERTATION

Submitted in partial fulfillment of the requirements
for the degree of Doctor of Philosophy in Physics
in the Graduate College of the
University of Illinois at Urbana-Champaign, 2008

Urbana, Illinois

Doctoral Committee:

Professor David Ceperley, Chair
Professor Richard Martin, Director of Research
Professor James Eckstein
Professor Paul Debevec

Abstract

We explore the role of electron correlation in quasi one dimensional quantum wires. We consider the effects of experimental parameters on the interaction, including screening by gates and other wires as well as the strength of the confinement to one dimension. We present the results of highly accurate quantum Monte Carlo calculations of the energy of the electron gas at various densities and polarizations. This data which is available along with this dissertation allows the construction of exchange-correlation functionals suitable for density functional calculations. We present sample functionals which are valid at any given density.

In the case of unscreened interactions with a long range $1/x$ tail there is a crossover from a liquid to a quasi Wigner crystal state as the density decreases. When this interaction is screened, quasi long range order is prevented from forming, although a significant correlation with $4k_F$ periodicity is still present at low densities. At even lower electron density, exchange is suppressed and the electrons behave like spinless fermions. These results are also supported by calculations of the momentum resolved spin and charge excitation energies. The long wavelength portions of these spectra also are used to calculate the spin susceptibility and charge compressibility of the electron gas.

Our calculations are quantitatively exact which allows us to compare with recent experiments [Steinberg *et al.*, Phys. Rev. B **77**, 113307 (2006)], by introducing an accurate model for the screening in the experiment and explicitly including the finite length of the sample in our simulations. We find that decreasing the electron density drives the system from a liquid to a state with rather strong $4k_F$ correlations. This crossover takes place around 22 μm^{-1}, near the density where the electron localization occurs in the experiment. The charge and spin velocities determined from the long wavelength excitation spectra are also in good agreement with the experimental findings.

We argue that correlation effects play an important role at the onset of the localization transition.

For my beloved wife, Alexandra

Acknowledgements

This work would never have been possible without the support and encouragement of a number of people. Firstly I would like to thank my parents for all of their love and dedication without which I would never have made it to MIT, much less the University of Illinois.

I would also like to thank my undergraduate lab partner and hall mate Francis Lam. It was during many long hours of data analysis and quantum physics study sessions that I developed a passion for physics and affinity for computer simulation. I would not have had nearly the depth of experience and fondness for this time without the camaraderie and insight of such a brilliant peer.

Richard Martin has been an advisor without rival. His ability to take complicated material and distill it to an intuitive kernel has astounded me regularly during my time in Urbana. In addition he has been an incredibly patient advisor who has gone above and beyond the call of duty countless times in helping me become the scientist I am today. Richard is one of the kindest people I have ever met and I wish him all the best in California.

I am at a loss for how to properly thank Michele Casula. Michele has been like a second advisor to me, having a hand in every facet of the research contained in this dissertation as well as providing endlessly useful advice. Whenever I encountered a roadblock in my work I could always count on Michele to pitch in with a smile. It is my sincerest desire to aspire to the level of competence and brilliance that Michele exemplifies.

I have benefitted greatly from interaction with many outstanding scientists as I have pursued this research. Discussions with Smitha Vishveshwara and Matthew Grayson were of great help in forming my understanding the onset of correlations in the electron gas and the observation of these correlations in experiment. Gaetano Senatore suggested the inclusion of the second wire as a screening medium in the study of the momentum resolved tunneling experiment. The opportunity to correspond with Ophir Auslaender has increased my understanding of experimental techniques in semiconductors quantum wires by leaps and bounds. David Ceperley provided me with crucial insights in the study of the excitations of the electron gas, furnishing me with both references and clear discussions the CFMC technique. I have also learned a great deal from Jeongnim Kim about writing electronic structure codes. I would also like to thank my office mate of several years Todd Beaudet. His friendship and coffee machine have been appreciated more than he knows.

Finally I would like to thank my wife Alexandra for her love and support. I could not have done this without her. From helping me choose the University of Illinois to proofreading my dissertation she has been with me every step of the way.

The work in this dissertation was supported by the NSF grant DMR-0404853 and the Materials Computation Center grant DMR-0325939. I would also like to acknowledge the support of a University Fellowship during my first year at the University of Illinois. Calculations were performed on the Turing cluster at the University of Illinois at Urbana-Champaign.

Table of Contents

List of Tables

List of Figures

List of Abbreviations

1D	One Dimension
1DEG	One Dimensional Electron Gas
2D	Two Dimensions
3D	Three Dimensions
CFMC	Correlation Function Monte Carlo
CLL	Chiral Luttinger Liquid
DFT	Density Functional Theory
DMC	Diffusion Monte Carlo
GFMC	Green Function Monte Carlo
GRPA	Generalized Random Phase Approximation
HF	Hartree-Fock
LL	Luttinger Liquid
LSDA	Local Spin Density Approximation
LRDMC	Lattice Regularized Diffusion Monte Carlo
LW	Lower Wire
MSA	Mean Spherical Approximation
NSF	Noninteracting Spinless Fermions
QMC	Quantum Monte Carlo
RPA	Random Phase Approximation
STLS	Singwi, Tosi, Land and Sjölander

TE	Transient Estimate
UW	Upper Wire
VMC	Variational Monte Carlo
WKB	Wentzel, Kramers and Brillouin

Chapter 1

Introduction

This dissertation is concerned with calculating the properties of the one dimensional electron gas both in an effort to further the theoretical understanding of correlations in one dimension and also to provide insight into the experimental observation of quasi one dimensional fermions. This introduction will present a summary of the current theory of the one dimensional electron gas with emphasis on the areas where this dissertation will add to the understanding.

The electron gas is an important model in condensed matter physics. The Fermi Liquid theory of electrons provides a method of mapping the physics of nearly free electrons onto the physics of materials. This insight has proved endlessly useful and is a crucial underpinning of one of the most successful techniques in computational electronic structure theory, Density Functional Theory (DFT). The study of the electron gas in one or two spatial dimensions was originally considered a theoretical curiosity with little practical application. However, now systems of two dimensional electrons are routinely used in semiconductor devices, and one dimensional electrons are realized by several different experimental techniques. In one dimension the Fermi liquid theory fails completely and as a result the electron gas has several characteristics not seen in higher dimensions. Specifically, the elementary excitations of the one dimensional electron liquid no longer carry both charge and spin, but are separated into entities that carry only one or the other.

1.1 Luttinger Liquid Theory

The very successful Luttinger liquid (LL) theory of one dimensional fermions was proposed by Luttinger and Tomonaga [1, 2]. This theory predicts several important phenomena, such as a power law decay in the occupation number at the Fermi Surface and spin charge separation. There have been several extensive presentations of the properties of Luttinger liquids in the literature, for examples see references [3, 4, 5, 6, 7]. This section will give a brief overview of the Luttinger liquid theory and will summarize some of its most important results. The notation in this section is consistent with that used by Giamarchi in chapter 2 of *Quantum Physics in One Dimension* [5].

It is possible to construct a general model that has all of the essential features of the LL. This LL model was proposed by Luttinger in 1963 [1], but its proper solution was left to Mattis and Lieb in 1965 [8]. As this model is intended to describe the low energy excitations of the 1D electron gas, the one-electron dispersion relation is linearized about the Fermi points. This linearization has two immediate consequences. Firstly, the electrons now have a different dispersion relation depending whether they are moving toward the left or toward the right. Secondly, this linearization results in a drastic simplification of the Hamiltonian. It is possible to write the Hamiltonian in terms of bosonic fields

$$\phi_\rho(x) = -\frac{i\pi}{L}\sum_{p\neq 0}\frac{1}{p}e^{-ipx}\left[\rho_+(x) + \rho_-(x)\right] \tag{1.1}$$

$$\phi_\sigma(x) = -\frac{i\pi}{L}\sum_{p\neq 0}\frac{1}{p}e^{-ipx}\left[\sigma_+(x) + \sigma_-(x)\right] \tag{1.2}$$

where $\rho_{+,-}(p)$ and $\sigma_{+,-}(p)$ are the usual charge and spin density operators for the left or right going fermions. Additionally $\Pi's$ are defined which are momenta conjugate to those fields. Using these definitions, the Hamiltonian separates into two commuting parts involving only charge and spin terms

$$\begin{aligned}
\hat{H} &= \hat{H}_\sigma + \hat{H}_\rho \\
\hat{H}_\rho &= \frac{1}{2\pi}\int dx\left[u_\rho K_\rho(\pi\Pi_\rho(x))^2 + \frac{u_\rho}{K_\rho}(\nabla\phi_\rho(x))^2\right] \\
\hat{H}_\sigma &= \frac{1}{2\pi}\int dx\left[u_\sigma K_\sigma(\pi\Pi_\sigma(x))^2 + \frac{u_\sigma}{K_\sigma}(\nabla\phi_\sigma(x))^2\right] \\
&\quad + H_{bs}\int dx\cos(2\sqrt{2}\phi_\sigma(x))
\end{aligned} \tag{1.3}$$

where H_{bs} describes the scattering from the left moving branch to the right moving branch and vice versa, K_σ and K_ρ describe the correlations and u_σ and u_ρ the spin and charge velocities. All of these are the interaction dependent LL parameters that describe the correlations in the system. The spin rotation invariance of the system enforces $K_\sigma = 1$ and when the system has continuous translational invariance the Galilean invariance requires that $K_\rho = v_F/u_\rho$. Therefore the behavior of the LL is reduced to just two parameters in the case of a translationally invariant Hamiltonian. In the case of noninteracting electrons the spin and charge velocities are exactly equal to 1 and the properties of the model are determined. However for repulsive interactions the charge velocity is increased relative to v_F and the spin velocity is suppressed.

The primary significance of Eq. 1.3 is that the Hilbert space of the problem can be written as a direct product of a charge and spin spaces. This phenomenon is known as spin charge separation and is a striking feature of one dimensional physics. The consequence of this is that no single particle excitations (which would necessarily carry both charge and spin) are possible in one dimension. Additionally the momentum distribution of the electrons can be found yielding

$$n(k) \propto |k - k_F|^{\frac{1}{4}\left(K_\rho + K_\rho^{-1} + K_\sigma + K_\sigma^{-1}\right) - 1}, \tag{1.4}$$

which vanishes algebraically at the Fermi level. This has a consequence for tunneling experiments where the probability to tunnel into the LL is proportional to the density of states at the Fermi level. Eq. 1.4 means that for a LL, the tunneling current is proportional to a power law of the temperature instead of the exponential behavior of a Fermi liquid. The Hamiltonian can be solved exactly when H_{bs} is zero as well as having low energy solutions via the renormalization group for finite H_{bs} [9]. Given this solubility, physical properties of the system such as the compressibility and the long range behavior of the correlation functions can be determined. For instance the pair correlation function of the electron gas becomes

$$\langle \rho(x)\rho(0) \rangle \propto \cos(2k_F x)\left(\frac{1}{x}\right)^{1+K_\rho} + \cos(4k_F x)\left(\frac{1}{x}\right)^{4K_\rho}, \tag{1.5}$$

where we note that all of these properties apply only to systems with short range interactions.

1.2 Long Range Interactions in One Dimension

Although there are physical systems (e.g. ultracold gases) where particles confined to one dimension have interactions with an extremely short range, electrons in semiconductors typically interact via a long range pair potential. The behavior of one dimensional electrons in the presence of such a long range potential was studied in a seminal paper by H. Schulz [10]. He found that for a potential that decays as $1/x$ at long range, the pair correlation function has components that decay more slowly than any power law. Specifically he found that the $2k_F$ and $4k_F$ components of the pair correlation function had the slowest decay and at long range were

$$\langle \rho(x)\rho(0)\rangle \propto A_1 \cos(2k_F) e^{-c_2\sqrt{\ln x}}/x + A_2 \cos(4k_F) e^{-4c_2\sqrt{\ln x}} + \ldots \tag{1.6}$$

where A_1, A_2 and c_2 are interaction dependent constants. Schulz was also able to show that it was only the long range behavior of the interaction that was responsible for this behavior and not the strength of the interaction. Specifically he found that for an interaction that decayed as $1/x^{\alpha}$ at long range, if $\alpha < 1$ a full crystalline order developed, if $\alpha = 1$ the quasi order of Eq. 1.6 was present and if $\alpha > 1$, the power law decay of the standard LL theory applied.[10, 11, 12]

In this work we study the results of calculations of the static structure factor (which is related to the pair correlation function by a Fourier transform) for several forms of the interactions at several interaction strengths. Our results confirm the predictions of Schulz, but find for high densities (weak interaction strength) that the prefactor of these correlations is vanishingly small and only as the interaction strength increases do these correlations become important. This crossover and its significance is discussed in chapter 6.

1.3 Comparison to Experiments

Although the general properties of the LL are known this theory is not predictive because its parameters are not determined. It is possible to compute them given a microscopic interaction by determining the spin and charge velocities or alternatively the charge compressibility and spin susceptibility as was carried out by Häusler *et al.* [13, 14]. This work is necessary because experiments have many methods of confining the electrons and experience various degrees of screening from a variety of sources as will be discussed in chapter 2. Thus one of the primary results of this work is providing an ab initio quantitative connection between the properties of the one dimensional electron gas and the LL paradigm for several different experimentally relevant interactions.

1.4 Organization

This dissertation will use electronic structure techniques to study the relations between the theory of one dimensional systems of Fermions and experimental realizations of one dimensional electrons. Chapter 2 presents an overview of the experimental systems in which quasi one dimensional Fermions are observed. Chapters 3 and 4 will present a model for calculating the properties of the one dimensional electron gas and the methods to perform these calculations in the ground state. Chapter 5 develops an understanding of the energy of the electron gas as a function of the density and electronic polarization, calculating this energy via quantum Monte Carlo techniques and parameterizing the results for use in Density Functional Theory calculations. Chapter 6 studies the onset of $4k_F$ correlations in the electron gas as the interactions are changed. Then chapters 7, 8, and 9 present methods for calculating the momentum resolved excitation energy of the electron gas and explore the dynamical properties of the gas in terms of these excitations. Finally chapter 10 introduces a series of recent experiments studying the properties of the electron gas in one dimensional wires, finding both the velocities of the excitations and a localization transition. Chapter 11 uses methods and theories developed throughout the dissertation to understand the phenomena observed in these experiments and to make quantitative comparison between our calculations and the experimentally observed quantities.

Chapter 2

Experimental Realizations of Quasi One Dimensional Fermions

There is a long history of experimental attempts to observe the physics of Luttinger Liquids. Although it is not possible to reduce the dimensionality of a particular sample per se, the physics of a system can take on a reduced dimensionality whenever the degrees of freedom in the various dimensions become decoupled. For one dimensional samples this means that the particles must maintain quantum coherence in the transverse directions while moving in the other.

Attempts to create and observe such localization have been complicated by two competing difficulties. The first of these is that for systems where the effective mass of the particles is low, the kinetic effects dominate and the signatures of one dimensional behavior become very small corrections to the dominant free particle behavior. Conversely when the interactions are much stronger than the kinetic contributions the effect of impurities dominates often leading to Coulomb Blockade physics where the charging of the impurity suppresses tunneling in the experiment[15]. Therefore many of the most successful experiments have focused on systems where extremely clean samples can be prepared and the electrons have a relatively high degree of mobility. This chapter will catalog some of the most important experimental tests of one dimensional phenomena.

2.1 Quantum Hall Edge States

The edges of two dimensional electron gas in a high magnetic field exhibit some strikingly one dimensional features. In fact a seminal work by X.-G. Wen proposed that these edge states would behave as a *chiral* Luttinger Liquid (CLL) [16]. Physically the reason for this chirality is straightforward, the large magnetic field in the plane of the electron gas causes the two directions of procession to have vastly different energy scales. Functionally this CLL shares many of the properties of the traditional LL, including spin charge separation and the power law decay of the occupation at the Fermi level (Eq. 1.4) [17].

One of the most influential observations of a CLL was made by Grayson *et al.* who observed the tunneling of electrons from a metal into the CLL [18]. This experiment allowed the observation of a power law suppression of the tunneling current at low voltages which is a hallmark of LL's. Also influential in this field is an experiment by Roddaro *et al.* which measured the tunneling of fractionally charged quasiparticles between two different quantum Hall Edge States, finding a direct correspondence between this behavior and that predicted for backscattering of electrons in a conventional LL [19].

2.2 Carbon Nanotubes

Carbon nanotubes also provide a useful laboratory in which to observe one dimensional physics. Depending on the coordination, these tubes may either be conducting or insulating [20]. In the case of conducting nanotubes two bands cross the Fermi level in each direction, so they can be viewed as having two different species of fermions roughly corresponding to electrons propagating clockwise and counterclockwise. Despite this complication, electrons in nanotubes exhibit many properties of a LL.

There has been a large amount of interest in carbon nanotubes both theoretically and experimentally. Experimentally Yao *et al.* were able to probe the conductance of a nanotube with a kink, finding that the tunneling current between the legs obeys a power law as a function of the temperature with an exponent close to that predicted by Luttinger liquid theory [21]. Experiments on bundles of nanotubes have also shown similar properties [22]. Of primary interest to this work there has been recent experimental evidence of a Wigner Crystal formed in a carbon nanotube,[23] which is analogous to the localized electrons found in semiconductor devices. This localization is discussed in chapter 10.

2.3 Ultra Cold Atoms

A relatively new method for studying one dimensional physics has been realized in ultra cold trapped atoms. In this case the atoms can be confined to one dimension by utilizing standing waves formed by lasers. This creates an array of elongated traps or"tubes" in which the atoms can interact. Much interest has been focused on Bose gases where the use of Fano-Feshbach resonances has allowed the s-wave scattering characterizing contact interactions to be tuned.[24, 25, 26] For these short range interactions, the "tubes" behave as if they were isolated and one dimensional. When the interparticle interaction becomes very strong and repulsive the bosons actually fermionize, acting as a gas of noninteracting fermions.[27, 28] This phenomenon was originally predicted by Tonks and Girardeau.[29] A similar phenomenon was proposed by Fogler termed the coulomb Tonks gas[30, 31] for interacting fermions in which the short range repulsion prevents exchange of electrons but at longer ranges the tail of the potential still has a significant effect. This prediction will be discussed in chapter 9. Finally recent theoretical proposals indicate that Luttinger Liquid behavior should be observable using currently available techniques in an ultracold ^{6}Li [32].

2.4 Semiconductors

The search for one dimensional physics in semiconductor quantum wires has a long and diverse history. Here two primary difficulties arise: firstly it is difficult to create a one dimensional trap for the electrons without impurities spoiling the physics and secondly it is difficult to observe the properties of the wires once they have been made. The first problem has been addressed in a variety of ways with one of the most successful being the development of the cleaved edge overgrowth technique [33]. In this method a one dimensional electron gas is created by making a wire at the edge of a two dimensional electron gas. Here a two dimensional electron gas is created by growing two atomically smooth layers of a semiconductor (in this case GaAs and AlGaAs) that have a mismatched band gap. Then this sample is cut perpendicular to the electron gas and another semiconductor layer is grown on the top, forming a "t" like structure. Stated simply, the wave function can spread out more at the junction, reducing the kinetic energy with little corresponding increase in potential energy. This effect is responsible for the formation of a bound state running along the line defined by the intersection of the two planes. This process and the sample geometry is depicted in Fig. 2.1.

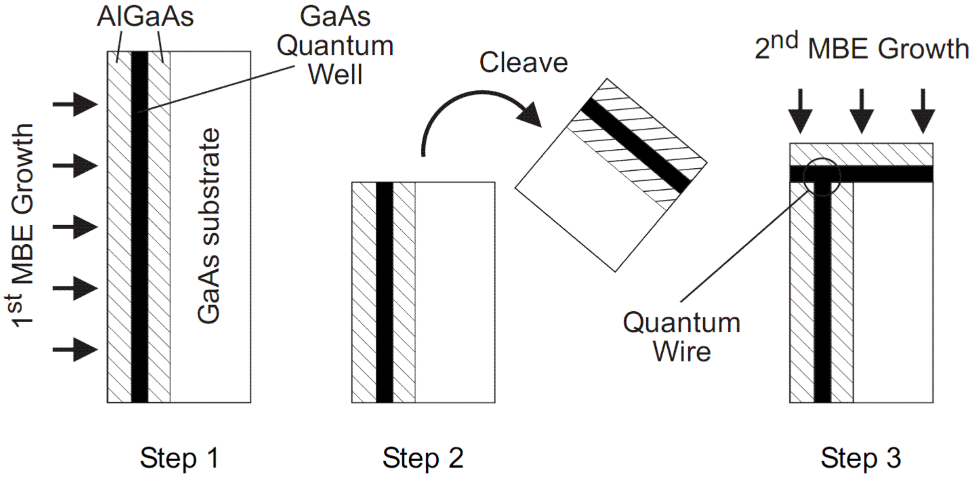

Figure 2.1: Molecular Beam Epitaxy growth sequence for fabricating quantum wires. The technique is called cleaved edge overgrowth. Figure is from Schuster *et al.*[34]

The observation of one dimensional physics in semiconductors has recently been greatly improved by a technique of momentum resolved tunneling between two quantum wires[35, 36, 37, 38, 39, 40, 41]. We will study this further and provide several comparisons between theory and experiment in chapters 10 and 11.

Chapter 3

A Model For Quasi One Dimensional Semiconductor Wires

This chapter develops a model for electrons confined to one dimension in semiconductors. This model will be used extensively throughout the rest of this work to perform numerical calculations. It consists of three dimensional electrons constrained to a wire by means of a harmonic confinement potential. This model we use was developed elsewhere in the literature and has been used extensively in the study of the quasi one dimensional electron gas.[42, 43, 44]. Throughout this and subsequent chapters we will use units of the effective Bohr radius ($a_0^\star = \frac{\hbar^2 \epsilon}{m^\star e^2}$) for length and the effective Rydberg ($Ryd^\star = \frac{e^2}{2\epsilon a_0^\star}$) for energy where ϵ is the dielectric constant of the embedding medium and $m^\star$ is the effective electron mass. In a typical GaAs quantum wire, $\epsilon = 13.1$, $m^\star = 0.067 m_e$, and $a_0^\star \approx 10nm$. The density of the electron gas is given in terms of the Wigner-Seitz radius ($n = \frac{1}{2r_s}$) which is a parameter measuring the radius of the n-dimensional sphere enclosing on average one electron.

3.1 Quasi 1D Electrons with Harmonic Confinement

For the purposes of our study, three dimensional electrons interact via the standard coulomb potential. These are then confined to a one dimensional wire by means of harmonic confinement potential that is constant along the wire, but increases as the square of the electron's distance from the wire.

$$V_{ext}(x, y, z) = \frac{y^2 + z^2}{4b^4} \tag{3.1}$$

Here b is a parameter that tunes the strength of the confinement potential. The electrons are assumed to be in the ground state of this transverse confinement potential, leading to a wavefunction of the form

$$\Psi(x,y,z) = \frac{1}{(2\pi b^2)^{\frac{1}{4}}}\, e^{-\frac{y^2+z^2}{4b^2}}\, \Psi(x) \tag{3.2}$$

Henceforth b controls the width of the wire with larger b's corresponding to wider wires and smaller b's corresponding to thinner wires.

If the density of the electrons in the wire is low enough, the degrees of freedom along the wire have a much lower energy scale than the transverse modes. This is the case when the Fermi energy of noninteracting one dimensional electrons is much less than the difference between the ground state and first excited state energy of the two dimensional harmonic oscillator defined by the potential in Eq. 3.1. This relation yields:

$$r_s \gg \frac{\pi b}{4}. \tag{3.3}$$

Integrating out these transverse degrees of freedom yields one dimensional electrons interacting via an effective potential:

$$\begin{aligned} V_b(x) &= \int\int d\vec{r}\,d\vec{r}\,' \frac{\rho_b(\vec{r})\rho_b(\vec{r}\,')}{\sqrt{(\vec{r}-\vec{r}\,')^2+x^2}} \\ &= \frac{\sqrt{\pi}}{b}\exp\left(\frac{x^2}{4b^2}\right)\operatorname{erfc}\left(\frac{|x|}{2b}\right) \end{aligned} \tag{3.4}$$

where $\vec{r}$ and $\vec{r}\,'$ are the transverse vectors and $\rho_b(\vec{r}) = \frac{1}{b\sqrt{2\pi}}\exp\left(-\frac{r^2}{2b^2}\right)$ is the ground state charge distribution of a two dimensional harmonic oscillator with the wire's confining potential: $V_{\text{wire}}(r) = \frac{r^2}{4b^4}$. This potential is finite at the origin with a value determined by the width of the wire ($V_b(0) = \sqrt{\pi}/b$) and it decays as $1/r$ at long range.

3.2 Periodic Boundary Conditions

Much of this work is concerned with properties of the electron gas in the thermodynamic limit, so in order to reduce finite size effects periodic boundary conditions for the wavefunction are used extensively throughout. Effectively this means that an electron interacts with the other electrons in the cell, their periodic images, its own images and a positive background that is introduced to preserve charge neutrality. For this reason it is useful to create an effective pair potential that sums the interaction of an electron with another electron located x away from the first, all of that electron's images and the positive background. This produces a periodic function:

$$V(x) = \sum_n \left[V_b(x + nL) - \frac{1}{L} \int_{-L/2}^{L/2} dy V_b(x + nL + y) \right] \tag{3.5}$$

where $L = 2Nr_s$ is the size of the simulation cell for N electrons at density r_s. The above potential can be Fourier transformed to give

$$\tilde{V}(G_n) = \frac{1}{L} \sum_n V(n\delta x) e^{iG_n k} \tag{3.6}$$

where the summation is finite because of the periodicity of the simulation cell and $G_n = 2\pi n/L$ is a reciprocal lattice vector of the 1D Bravais lattice with $\delta x = \frac{L}{2N}$. Here

$$\tilde{V}_b(k) = 2E_1(b^2k^2) \exp(b^2k^2) \tag{3.7}$$

is the Fourier transform of the bare pair potential $V_b(x)$ given in Eq. 3.4, and E_1 is the exponential integral function.

The bare interparticle is long range and because of this the summation in Eq. 3.5 converges only conditionally. In order to evaluate this potential we utilize an Ewald-like method [45]. This approach divides the potential into short and long range pieces. The short range piece is then summed in real space while the long range part is handled in reciprocal space. Specifically,

$$\begin{aligned} V(x) &= V_{\mathrm{sr}}(x) + V_{\mathrm{lr}}(x), && (3.8) \\ V_{\mathrm{sr}}(x) &= \frac{\sqrt{\pi}}{b} \sum_{-\infty}^{\infty} \exp\left[\frac{(x - nL)^2}{4b^2}\right] \mathrm{erfc}\left(\frac{|x - nL|}{2b}\right) \\ &\quad - \sum_{-\infty}^{\infty} \frac{2}{|x - nL|} \mathrm{erf}\left(\frac{|x - nL|}{2b}\right) && (3.9) \\ V_{\mathrm{lr}}(x) &= 2 \sum_{n>0} \frac{\cos(G_n x)}{L} e^{-(bG_n)^2} \tilde{V}_b(G_n). && (3.10) \end{aligned}$$

Using this notation, the final Hamiltonian is

$$H = -\sum_{i=1}^{N} \nabla_i^2 + \sum_{i<j} V(|x_i - x_j|) + \frac{N}{2}(V(0) - V_b(0)) \tag{3.11}$$

where $\frac{N}{2}(V(0) - V_b(0))$ is the Madelung energy which corresponds to the interaction of the particles with their own images.

3.3 Screening

Experimentally quantum wires are often fabricated in the presence of external metallic gates which are used to control the wire. These gates screen the interaction of the electrons at large distances, resulting in a shorter range potential. The form of this potential can be found assuming that the gate is placed parallel to the wire and it is perfectly conducting. In this approximation the potential between two electrons on the wire can be found via the electrostatic method of images[46], whereby electrons in the quantum wire induce image charges of equal and opposite sign in the gate located twice as far from the wire as the gate. This geometry is shown in Fig. 3.1 as compared to the unscreened interaction.

The equation for this potential is

$$\begin{aligned} V_{b,R}(x) = & \int\int d\,\vec{r} d\,\vec{r}' \frac{\rho_b(\vec{r})\rho_b(\vec{r}')}{\sqrt{(\vec{r}-\vec{r}')^2 + x^2}} - \\ & \int\int d\,\vec{r} d\,\vec{r}' \frac{\rho_b(\vec{r})\rho_b(\vec{r}')}{\sqrt{(\vec{r}-\vec{r}'-2\vec{R})^2 + x^2}} \\ = & V_b(x) - V_{int}(x, R) \end{aligned} \tag{3.12}$$

where $\vec{r}$ and $\vec{r}'$ are transverse vectors, $\rho_b(\vec{r}) = \frac{1}{b\sqrt{2\pi}} \exp\left(-\frac{r^2}{2b^2}\right)$ is the ground state charge distribution of a two dimensional harmonic oscillator with the wire's confining potential: $V_{\mathrm{wire}}(r) = \frac{r^2}{4b^4}$. The first integral gives the effective unscreened inter-particle potential $V_b(x)$ described in the previous section and the second one is the potential due to the image charge on the screening wire: $V_{int}(x, R)$. Note that this is only one type of screening that may be present in the system and that in general screening from the closest source dominates the form of the interaction. Another screened interaction

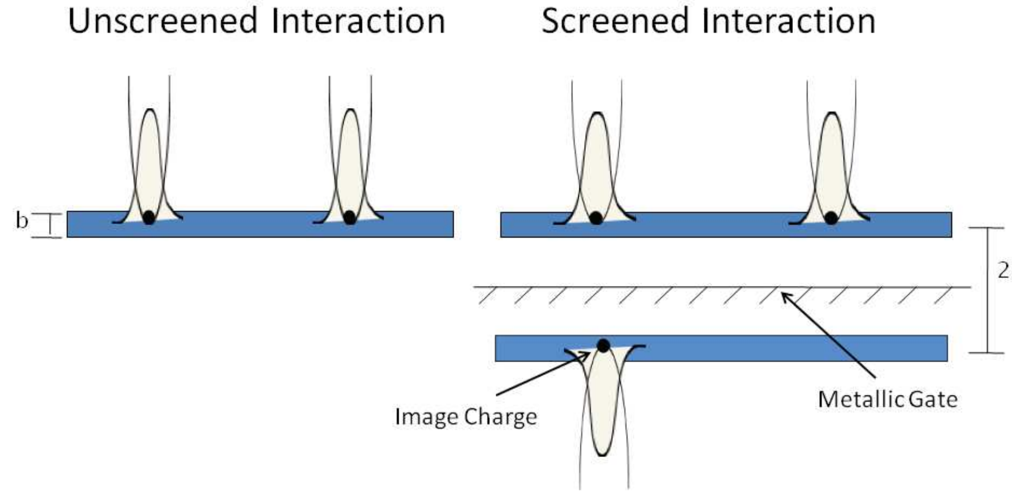

Figure 3.1: Schematic of the interaction in quantum wires. On the left the unscreened interaction with two electrons confined to a wire of width b interact. The right hand side introduces a metallic gate parallel to the wire a distance R away. The electron on the right hand side feels the repulsion from its neighbor and also from the image charge induced in the gate.

involving the electrons in a real wire parallel to the first one will be discussed in Sec. 11.1

In contrast to the unscreened interaction which decays like $1/x$ at long range, the interaction screened by a semi infinite metallic gate behaves as $V(x) = 4R^2/x^3$ as $x \to \infty$. This means that instead of the Ewald-like procedure of section 3.2, this interaction may be summed directly. As a practical consideration, the terms in the asymptotic expansion of the summation $V(x) = \sum_n V_{b,R}(x + n2Nr_s)$ can be summed analytically

$$\lim_{n\to\infty} \sum_{i=n}^{\infty} V_{b,R}(x + i2Nr_s) = \frac{2R^2\psi_2(n - \frac{x}{2Nr_s})}{(2Nr_s)^3} \tag{3.13}$$

where $\psi_2(x)$ is the second order polygamma function. So the total interaction is calculated by summing several terms in the interaction and this long range form:

$$
\begin{aligned}
V(x) &= V_{\mathrm{sr}}(x) + V_{\mathrm{lr}}(x) \\
V(x) &= V_{b,R}(x) + \sum_{n=1}^{m-1} V_{b,R}(x + 2Nr_s) + \sum_{n=-1}^{1-m} V_{b,R}(x + 2Nr_s) \\
&\quad + \frac{2R^2\psi_2(m - \frac{x}{2Nr_s})}{(2Nr_s)^3} + \frac{2R^2\psi_2(-m + \frac{x}{2Nr_s})}{(2Nr_s)^3} \qquad (3.14)
\end{aligned}
$$

Chapter 4

Calculating Ground State Properties via QMC

Although there have been many great advances in the study of the one dimensional electron gas via analytical methods, it is still not possible to make quantitatively accurate calculations of many of the properties of the electron gas via analytical means. There are however several numerical methods for performing calculations of these properties. When the single particle states of the system can be described via a relatively small set of basis functions, as is the case for many model systems, it is possible to exactly diagonalize the many body problem via methods such as Lanczos when the number of particles is small[47, 48, 49]. In one dimension larger systems may be treated via the density matrix renormalization group algorithm[50].

In the case of a continuous Hamiltonian, a slightly different approach is necessary. Density Functional Theory is a natural choice for such cases because of its small computational cost and ability to treat complicated geometries and potentials with ease. Unfortunately the typical functionals used to determine the correlation energy in such calculations are not suitable for one dimensional systems as they are derived for a three dimensional electron gas. Following the work of Casula *et. al.*[43], there have been DFT calculations of quantum wires which use QMC calculations of the energy of the quasi one dimensional electron gas as a reference [51]. This work suggests the need for a spin dependent energy functional, a functional we endeavor to create in chapter 5 using the methods developed in this chapter.

In this case, the quantum Monte Carlo method allows the ground state properties of the electron gas to be calculated with no uncontrolled approximations and with a relatively modest computational cost. In one dimension, the computational cost of the QMC calculations performed in this work scales as the square of the number of electrons, with further refinements possibly allowing even better scaling. This chapter will provide a detailed description of the quantum Monte Carlo method as it is applied to the study of the ground state properties of the one dimensional electron gas.

4.1 Quantum Monte Carlo Methods

Quantum Monte Carlo (QMC) is an extraordinarily powerful tool for calculating the properties of many body systems. This section will endeavor to present a general introduction to the QMC methods used to calculate the properties of the ground state of the one dimensional electron gas.

4.1.1 Variational Monte Carlo

The Variational Monte Carlo method can be used to calculate matrix elements of a complicated wave function whose evaluation would be extraordinarily costly via conventional means. These matrix elements are typically written as ND dimensional integrals where N is the number of electrons and D is the dimensionality of the space. If these integrals are approximated using a grid-based method, the computational cost will scale with the size of the grid. For the simple case of a uniform grid with M points per dimension this cost is of the order M^{ND}, which is too large for all but the smallest numbers of electrons. Monte Carlo techniques allow the evaluation of these ND dimensional integrals with a cost that scales only as the square root of the number of dimensions, making these methods much more suitable for these problems.

Variational Monte Carlo uses the Monte Carlo method to calculate the matrix element of a particular observable $\hat{O}$ with a known trial wavefunction Ψ. Specifically,

$$\left\langle \hat{O} \right\rangle = \frac{\int \Psi^{\star}(\mathbf{R}) O(\mathbf{R}) \Psi(\mathbf{R}) d\mathbf{R}}{\int \Psi^{\star}(\mathbf{R}) \Psi(\mathbf{R}) d\mathbf{R}} \tag{4.1}$$

where $\mathbf{R}$ are the N spatial coordinates of the particles. This integral is rewritten so that the coordinates are sampled according to the square of the trial wave function Ψ:

$$\left\langle \hat{O} \right\rangle = \frac{\int \left|\Psi(\mathbf{R})\right|^2 \frac{\hat{O}\Psi(\mathbf{R})}{\Psi(\mathbf{R})} d\,\mathbf{R}}{\int \left|\Psi(\mathbf{R})\right|^2 d\,\mathbf{R}}. \tag{4.2}$$

Now all that is needed is an algorithm to sample these coordinates $\mathbf{R}$. The coordinates are chosen via the Metropolis algorithm[52]. This algorithm is a method of drawing samples from an arbitrary probability distribution. It accomplishes this by creating a Markov chain, which is a random walk that samples the appropriate distribution after an equilibration phase. A sufficient condition for any such Markov chain to have equilibrated is that the rate at which a walker moves from $\mathbf{R}$ to another point $\mathbf{R}'$ is equal to the rate at which walkers move from $\mathbf{R}'$ back to $\mathbf{R}$.

In order to accomplish this, the probability of making a given move is then broken into two parts. The first is a probability distribution from which trial moves are taken (P_{trial}) and the second is the probability that these trial moves are accepted (P_{accept}). Typically the distribution of trial moves is taken to be something simple like a constant probability inside of a hypercube around the initial configuration or a Gaussian centered around the previous location, although in principle it should be chosen to minimize the autocorrelation of the quantity being observed ($\hat{O}$ in Eq.4.1) between subsequent samples. The acceptance probability then is chosen so that the total probability of making a move is

$$P(\mathbf{R} \rightarrow \mathbf{R}') = P_{\text{trial}}(\mathbf{R} \rightarrow \mathbf{R}')P_{\text{accept}}(\mathbf{R} \rightarrow \mathbf{R}'). \tag{4.3}$$

In order for the system to have an equilibrium distribution of Ψ^2, a sufficient condition is

$$\Psi^2(\mathbf{R})P(\mathbf{R} \rightarrow \mathbf{R}') = \Psi^2(\mathbf{R}')P(\mathbf{R}' \rightarrow \mathbf{R}), \tag{4.4}$$

which is known as detailed balance and requires that the flux from one configuration to another is equal to the flux in the opposite direction.

The Metropolis algorithm uses this condition to determine the acceptance probability

$$P_{\text{accept}}(\mathbf{R} \rightarrow \mathbf{R}') = \min\left(1, \frac{P_{\text{trial}}(\mathbf{R}' \rightarrow \mathbf{R})\Psi^2_{\text{trial}}(\mathbf{R}')}{P_{\text{trial}}(\mathbf{R} \rightarrow \mathbf{R}')\Psi^2_{\text{trial}}(\mathbf{R})}\right). \tag{4.5}$$

Finally the matrix element is computed as the average over these configurations of the following quantity

$$\left\langle \hat{O} \right\rangle = \frac{1}{N} \sum_{\mathbf{R}} \frac{\hat{O}\Psi_{\text{trial}}(\mathbf{R})}{\Psi_{\text{trial}}(\mathbf{R})}. \tag{4.6}$$

It is thus vitally important to choose a good approximation to the true many body wavefunction whenever these VMC calculations are performed.

4.1.2 Trial Wave Function

As a starting point, we choose a simple wavefunction that maintains the translational invariance of the system as well as the antisymmetry of the fermions. Additionally we include a two body term that correlates the behavior of the electrons at both short and long range. This is the Slater-Jastrow wave function

$$\Psi_T = D^{\uparrow} D^{\downarrow} \exp\left(-\sum_{i<j} u(x_{ij})\right), \tag{4.7}$$

where each determinant D^{σ} is the antisymmetrized product of N^{σ} plane waves occupied up to the Fermi momentum for that species:

$$k_F = \frac{\pi(1 \pm \zeta)}{4r_s} \tag{4.8}$$

with $\zeta = (N^{\uparrow} - N^{\downarrow})/N_{\text{tot}}$ where the plus is for the majority spin species and the minus the minority. As a technical point, a general antisymmetrized product of these N^{σ} orbitals may be calculated in $O(N^3)$ operations. In one dimension with a filled Fermi sea of states, this determinant can be written as a Van der Monde determinant, which can be calculated in only $O(N^2)$ operations:

$$D^{\sigma}(x_1^{\sigma}, \ldots, x_{N^{\sigma}}^{\sigma}) = \prod_{1 \le i < j \le N^{\sigma}} \sin\left(\frac{G}{2}(x_i^{\sigma} - x_j^{\sigma})\right), \tag{4.9}$$

with $G = 2\pi/L$, and $L = 2r_sN$ the length of the simulation cell. Further simplifications to reduce the complexity of this calculation are possible.

We follow Ref. [53] to determine the Jastrow function $u(x)$. Its Fourier components are

$$2\rho\tilde{u}(k) = -S_0(k)^{-1} + \sqrt{S_0(k)^{-2} + \frac{\tilde{V}_b(k)}{2r_sk^2}} \tag{4.10}$$

with $S_0(k) = (k/2k_F)\theta(2k_F - k) + \theta(k - 2k_F)$ the structure factor of a noninteracting 1DEG, $\rho = \frac{1}{2r_s}$ the density, and $\tilde{V}_b(k)$ the Fourier transform of $V_b(x)$. This Jastrow function is repulsive at short range to produce a wavefunction where the electrons are less likely to approach each other. This Jastrow also includes the proper long wavelength correlations from the Random Phase Approximation. More elaborate Jastrow functions have been tried for this system, but a simple rescaling of the Jastrow in Eq. 4.10 was found to have very similar properties for less computational overhead.[43]

4.1.3 Diffusion Monte Carlo

The diffusion Monte Carlo (DMC) algorithm allows matrix elements of the ground state of the many body Schrödinger equation to be calculated with less dependence on the trial wavefunction than the VMC method.[54, 55, 56] The DMC algorithm works by considering the Schrödinger equation in imaginary time.

$$\frac{\partial \left|\psi\right\rangle}{\partial \tau} = -\hat{H} \left|\psi\right\rangle \tag{4.11}$$

which has the solution

$$\left|\psi(\tau)\right\rangle = e^{-\tau \hat{H}} \left|\psi(0)\right\rangle > \tag{4.12}$$

Any wavefunction $\left|\Psi\right\rangle$ can be expanded in terms of the eigenstates of $\hat{H}$: $\left|\Psi\right\rangle = \sum_i a_i \left|\phi_i\right\rangle$. Substituting this into Eq. 4.12, it is plain that as τ becomes large, all higher excited states are exponentially suppressed

$$\lim_{\tau \to \infty} \left|\psi(\tau)\right\rangle = c_0 e^{-\epsilon_0 \tau} \left|\psi_0\right\rangle . \tag{4.13}$$

In light of this we rewrite the imaginary time Schrödinger equation in first quantized form with an arbitrary energy offset:

$$\frac{1}{2}\nabla^2 \psi(\mathbf{R},\tau) + \left[E_T - V(\mathbf{R})\right] \psi(\mathbf{R},\tau) = \frac{\partial \psi(\mathbf{R},\tau)}{\partial \tau}. \tag{4.14}$$

This has the form of an N dimensional diffusion equation where the wavefunction takes the place of the density of the particles. Following Reynolds *et al.* [54] this can be transformed into an importance sampled integral equation

$$f(\mathbf{R},\tau) = \int G(\mathbf{R},\mathbf{R}';\tau') f(\mathbf{R}',\tau)) d\,\mathbf{R}' \tag{4.15}$$

where $f(\mathbf{R}, \tau + \tau') = \psi(\mathbf{R}, \tau)\Psi_T(\mathbf{R})$ is a product of a known trial wavefunction Ψ_T and the eigenfunction ψ.[54, 57] $G(\mathbf{R}, \mathbf{R}'; \tau)$ is the Green's function for

$$\frac{1}{2}\nabla^2 f(\mathbf{R}, \tau) + \nabla \cdot \left[\nabla \ln |\Psi_T(\mathbf{R})| \, f(\mathbf{R}, \tau)\right] + \left[E_T - \frac{\hat{H}\Psi_T(\mathbf{R})}{\Psi_T(\mathbf{R})}\right] f(\mathbf{R}, \tau) = \frac{\partial f(\mathbf{R}, \tau)}{\partial \tau}. \tag{4.16}$$

The importance sampling has two main roles. The first is to greatly increase the efficiency of the sampling if the trial wavefunction is reasonable. The second role is to allow the simulation of fermionic systems by imposing boundary conditions on the diffusion process. The true ground state of the system is assumed to have the same nodes as the trial wavefunction, thereby preventing a collapse to the bosonic ground state. This approximation and its effects will be further discussed in Section 4.1.5

The task now is to calculate this Green's function. Introducing the drift velocity $v_D(\mathbf{R}) = \nabla \ln |\Psi_T(\mathbf{R})|^2$, the Green's function for a diffusion process with no potential is known:

$$G_{\text{diff}}(\mathbf{R}, \mathbf{R}'; \tau) = \frac{1}{(2\pi\tau)^{N/2}} \exp\left(-\frac{(\mathbf{R} - \mathbf{R}' - \tau v_D(\mathbf{R}'))^2}{2\tau}\right). \tag{4.17}$$

The part of Eq. 4.16 involving the potential and the trial energy is just a rate equation whose Green's function is approximated by

$$G_{\text{rate}}(\mathbf{R}, \mathbf{R}'; \tau) = \exp\left(-\tau \frac{E_L(\mathbf{R}) + E_L(\mathbf{R}') - 2E_T}{2}\right) \tag{4.18}$$

where

$$E_L(\mathbf{R}) = \hat{H}\Psi_T(\mathbf{R})/\Psi_T(\mathbf{R}). \tag{4.19}$$

The full Green's function can now be approximated in the limit of a small time-step τ using the Trotter-Suzuki formula [58, 59]

$$G(\mathbf{R}, \mathbf{R}'; \tau) = G_{\text{diff}}(\mathbf{R}, \mathbf{R}'; \tau) G_{\text{rate}}(\mathbf{R}, \mathbf{R}'; \tau). \tag{4.20}$$

Configurations can be sampled from this Green's function by using drift diffusion dynamics

$$\mathbf{R}' = \mathbf{R} + \tau v_D(\mathbf{R}) + \chi\sqrt{2\tau} \tag{4.21}$$

where χ is a normally distributed Gaussian random variable and a proposed move to $\mathbf{R}'$ is accepted with probability

$$P_{\text{accept}}(\mathbf{R} \to \mathbf{R}') = \min\left(1, \frac{G(\mathbf{R}, \mathbf{R}'; \tau)\Psi_T(\mathbf{R})^2}{G(\mathbf{R}', \mathbf{R}; \tau)\Psi_T(\mathbf{R}')^2}\right), \tag{4.22}$$

a step that is only necessary because of the approximate Green's function G. Note that as $\tau \to 0$, the acceptance probability goes to 1.

4.1.4 Lattice Regularized Diffusion Monte Carlo

We also make extensive use of the lattice regularized diffusion Monte Carlo (LRDMC) algorithm in this work. This section will follow the discussion of LRDMC in Casula *et al.* [43]. The LRDMC method was originally introduced to eliminate the localization error with nonlocal pseudopotentials [60]. LRDMC operates on a regularized Hamiltonian in a way that the Green function Monte Carlo (GFMC) algorithm on a lattice can be applied to continuous systems [61, 62, 63].

Regularization of the Hamiltonian involves separate approaches for both the potential and the kinetic terms. Firstly, the Laplacian is discretized using a finite difference approximation

$$\Delta = \nu\left[p\Delta^a + (1-p)\Delta^{a'}\right] + O(a^2) \tag{4.23}$$

where Δ^a is a Hermitian operator having the action

$$\Delta^a\psi(x_i) = \frac{1}{a^2}\left(\psi(x_i + a) + \psi(x_i - a) - 2\psi(x_i)\right) \tag{4.24}$$

with a being the size of the finite difference mesh and p being a constant that sets the relative importance of the two meshes a and a'. In general, p can vary spatially, a freedom that is not exploited in homogeneous systems. The different lattice spacings a and a' are chosen to be incommensurate so that the random walk may sample all of the continuous configuration space. In this way, the bias due to the discretization of the continuous operator is greatly reduced.

The second step in the lattice regularization involves the potential. The potential is regularized subject to three constraints: i) the final Hamiltonian H^a becomes equal to the continuous Hamiltonian H when the lattice spacing $a \to 0$; ii) given the trial wave function Ψ_T, for any lattice spacing a and configuration $\mathbf{R}$ the local energy (Eq.4.19) of the discretized Hamiltonian is equal to that of the continuous Hamiltonian; and iii) The discretized kinetic energy is equal to the continuous kinetic energy when calculated on the state Ψ_T. Condition (iii) fixes the constant ν, while the condition (ii) constrains the form of the regularized potential V^a:

$$V^a(\mathbf{R}) = V(\mathbf{R}) + \frac{1}{2}\left[\frac{\sum_i(\Delta_i^a - \Delta_i)\Psi_T}{\Psi_T}\right](\mathbf{R}). \tag{4.25}$$

The condition (ii) yields another important property for H^a: if Ψ_T is an eigenstate of H, it is also an eigenstate of H^a for any a. Thus, as the quality of Ψ_T increases the dependence of the LRDMC energy on a decreases.

The lattice regularized Hamiltonian H^a reads:

$$H^a_{\mathbf{R}',\mathbf{R}} = \begin{cases} -\nu\ p/a^2 & \text{if } \mathbf{R}' = \mathbf{R} + \delta_a \\ -\nu\ (1-p)/a'^2 & \text{if } \mathbf{R}' = \mathbf{R} + \delta_{a'} \\ 2N\nu\left(\frac{p}{a^2} + \frac{1-p}{a'^2}\right) + V^a(\mathbf{R}) & \text{if } \mathbf{R}' = \mathbf{R}, \end{cases} \tag{4.26}$$

where δ_a ($\delta_{a'}$) is a N dimensional vector composed of one particle displacements of length $\pm a$ ($\pm a'$). This means that there are $2N$ possible δ_a ($\delta_{a'}$) and the lattice discretized Hamiltonian contains $4N$ off diagonal elements. Thus when defining the importance sampled Green's function

$$G_{\mathbf{R}',\mathbf{R}} = \Psi_T(\mathbf{R}')\frac{\Lambda\delta_{\mathbf{R}',\mathbf{R}} - H_{\mathbf{R}',\mathbf{R}}}{\Psi_T(\mathbf{R})}, \tag{4.27}$$

a configuration $\mathbf{R}$ is connected only to a finite number of $\mathbf{R}'$. This property allows the now discrete Green's function to be sampled using the heat bath algorithm just as in the standard GFMC scheme[61, 62, 63]. It is also necessary to take the limit $\Lambda \to \infty$ because Hamiltonian H^a is not bounded from above.

4.1.5 Fixed-Node Approximation

In both the DMC and LRDMC methods there is a problem that is introduced by interpreting the imaginary-time Schrödinger equation as a diffusion equation. This procedure rests on interpreting the wavefunction as a probability density for Monte Carlo sampling. The difficulty comes because a probability density must be strictly nonnegative, which is manifestly not the case for a many body fermion wavefunction.

The first approach to this problem was proposed by Anderson [64]. He used a trial wavefunction as reference and killed any walker that made a move that crossed the node of that wavefunction. This solution imposes boundary conditions on the nodal pockets of the wavefunction. This is a variational approximation, yielding an upper bound on the ground state energy for any choice of trial wavefunction [65].

It was later found that in addition to the bias caused because the nodes of the trial wavefunction are not the same as the nodes of the true ground state wavefunction, Anderson's approximation caused a bias that was proportional to the time step used in the calculation [55]. This bias can be reduced by simply rejecting any move that crosses the nodes of the trial wavefunction. This is the approach that is employed in our calculations. In DMC this is a straightforward method to apply, while a somewhat subtle nuance is introduced in LRDMC. For LRDMC, the heat bath algorithm is affected by effectively removing any configurations that lead to the crossing of the nodes. This can be remedied by including their contributions in the term which has the walker remain in its current position. To wit, the effective fixed node Hamiltonian becomes

$$H^{\mathrm{eff}}_{\mathbf{R},\mathbf{R}'} = \begin{cases} H^a_{\mathbf{R},\mathbf{R}'} & \text{if } \mathbf{R} \neq \mathbf{R}' \text{ and } \frac{\Psi_T(\mathbf{R}')H^a_{\mathbf{R},\mathbf{R}'}}{\Psi_T(\mathbf{R})} \leq 0 \\ 0 & \text{if } \mathbf{R} \neq \mathbf{R}' \text{ and } \frac{\Psi_T(\mathbf{R}')H^a_{\mathbf{R},\mathbf{R}'}}{\Psi_T(\mathbf{R})} > 0 \\ H^a_{\mathbf{R},\mathbf{R}} + \mathcal{V}_{sf}(\mathbf{R}) & \text{if } \mathbf{R} = \mathbf{R}', \end{cases} \tag{4.28}$$

where $\mathcal{V}_{sf}(\mathbf{R}) = \sum_{\mathbf{R}' \neq \mathbf{R}} \frac{\Psi_T(\mathbf{R}')H^a_{\mathbf{R}',\mathbf{R}}}{\Psi_T(\mathbf{R})} > 0$, the so called sign-flip term, is the sum over all the terms that cause a negative sign problem in the Monte Carlo sampling [60].

Fortunately, in one dimension, the nodes of the ground state wavefunction are known *exactly*. This is possible because in one dimension the nodal structure of the ground state is exactly defined by the coalescence planes $x_i = x_j$, where x_i and x_j are the coordinates of electrons with the same spin. Thus the nodes of the wavefunction are completely determined by the antisymmetry of the particles [66]. This property allows the ground state properties of the 1D electron gas to be calculated exactly within DMC.

4.1.6 Mixed Estimators and Forward Walking

For operators that do not commute with the Hamiltonian both the LRDMC and DMC methods suffer from the so called mixed estimator bias. This means that if the configurations are simply sampled from the mixed distribution $\Psi_T(\mathbf{R})\phi(\mathbf{R})$, and an observable that does not commute with the Hamiltonian is calculated at these configurations, then there will be a bias because the matrix element calculated is:

$$\frac{\langle\Psi_T|\,\hat{O}\,|\psi_0\rangle}{\langle\Psi_T|\phi_0\rangle} \tag{4.29}$$

instead of the desired matrix element

$$\frac{\langle\phi_0|\,\hat{O}\,|\phi_0\rangle}{\langle\phi_0|\phi_0\rangle} \tag{4.30}$$

This bias may be eliminated by using the forward walking algorithm.[67, 62] The algorithm consists of using the Green's function to propagate the trial wave function on both sides of the matrix element. This is accomplished by using the standard DMC or LRDMC technique to generate a sequence of configurations distributed as $\Psi_T\phi_0$. Then the observable is calculated using a configuration at time t, but with the product of the weighting factors from t' iterations previous $W(t,t') = \prod_{i=t-t'}^{t} w_i$ rather than simply the weight of the walker at the current time. Therefore the final observable is calculated as

$$\frac{\langle\phi_0|\,\hat{O}\,|\phi_0\rangle}{\langle\phi_0|\phi_0\rangle} = \sum_{l,t}\frac{W(t,t')O(\mathbf{R}_l,t)}{W(t,t')} \tag{4.31}$$

where $O(\mathbf{R}_l,t)$ is the value of the observable calculated for walker l at imaginary time t with the trial wavefunction. This algorithm is limited because the variance of weight term $W(t,t')$ diverges in the large t' limit. As such the convergence of the quantity being considered must be monitored closely. An example of the convergence of a quantity under forward walking is presented in Fig. 8.1.

4.1.7 Finite Population Bias

The population of walkers is controlled via stochastic reconfiguration. Periodically a new population of walkers is chosen randomly from the current population where a walker's chance of being selected is proportional to its relative weight. These new walkers are all taken to have a weight of 1. It is necessary to implement the G_{rate} term with a fixed number of walkers because without any sort of population control, the variance of the weights of the walkers will become infinite [68]. This bias is eliminated by using the forward walking algorithm presented in section 4.1.6.

4.2 Comparison of LRDMC and DMC

A peculiar difficulty of one dimensional simulations makes the exchange of electrons exponentially unlikely as the strength of the interaction increases. This origin of this difficulty is due to the Jastrow factor which makes the approach of two electrons unlikely.

If the spin configurations are not accurately sampled the Markov chain is not ergodic and the Monte Carlo calculation is no longer exact for the spin properties of the system. Fortunately the energy of the spin degrees of freedom is exponentially small at low density, so the approximation is small in the calculation of total energies.

LRDMC is better suited to sample the spin degrees of freedom for two reasons. The first is that the drift term in DMC enhances the effect of the pseudo nodes by pushing particles away from their neighbors whenever they become close. To understand the second it is first necessary to note that the time step controls the diffusion constant in the simulation which in turn controls the exchange rate. As shown in Fig. 4.1, for a given diffusion constant LRDMC has a much smaller error in the energy than DMC. Because of this, for a given tolerated error in the energy, the LRDMC has a larger diffusion constant and thus a much larger exchange rate. This increased ergodicity does not spoil the spin properties of the system for moderate lattice spaces as confirmed by the agreement between the LRDMC and WKB spin susceptibilities at moderate density in Fig. 9.3.

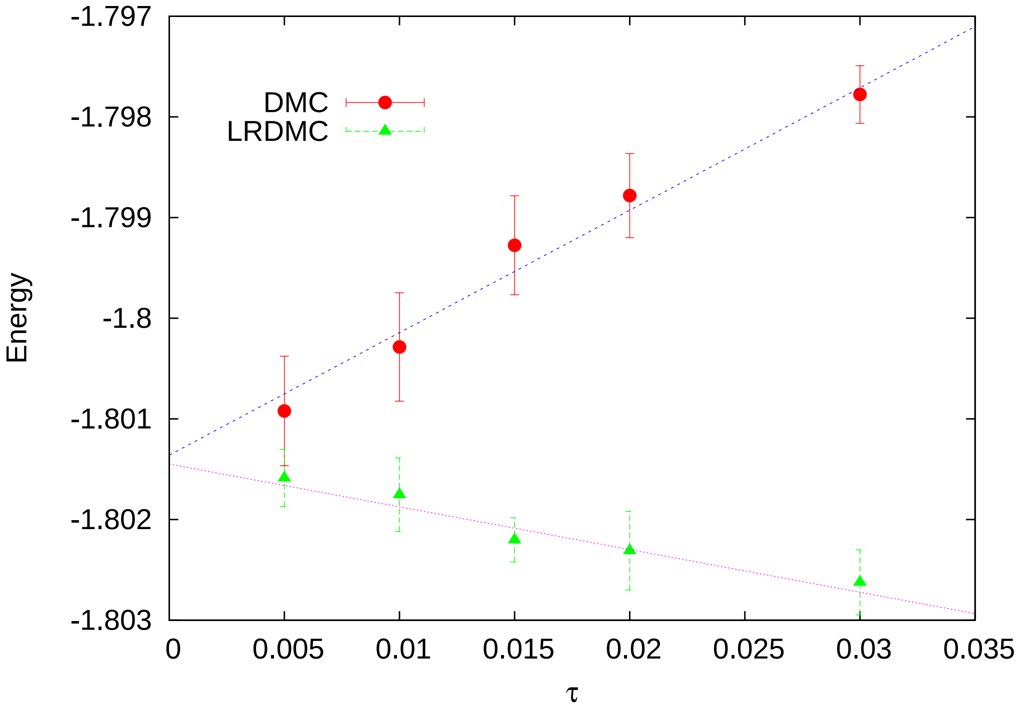

Figure 4.1: DMC and LRDMC energies for 22 electrons with $r_s = 1$ and $b = 0.1$. The time-step is chosen so that the diffusion constant is the same between the DMC and LRDMC simulations, namely $2\tau = a^2$ where τ is the DMC time-step and a is the LRDMC lattice space

In Fig. 4.2, the exchange rate is plotted as a function of the density. Although for higher densities the exchange rates are quite similar, at low density the exchange rate is nearly two orders of magnitude higher in LRDMC than DMC.

4.3 Finite Size Corrections

In order to determine the energies in the thermodynamic limit, it is necessary to understand how the energy is affected by the size of the system. There are three different terms in the finite size correction used in this work. The first is a one body term due to the incomplete sampling of the kinetic energy. The other two terms are due the sampling of the long range part of the structure factor. The discussion in this section follows the notation of Chiesa *et al.* [69].

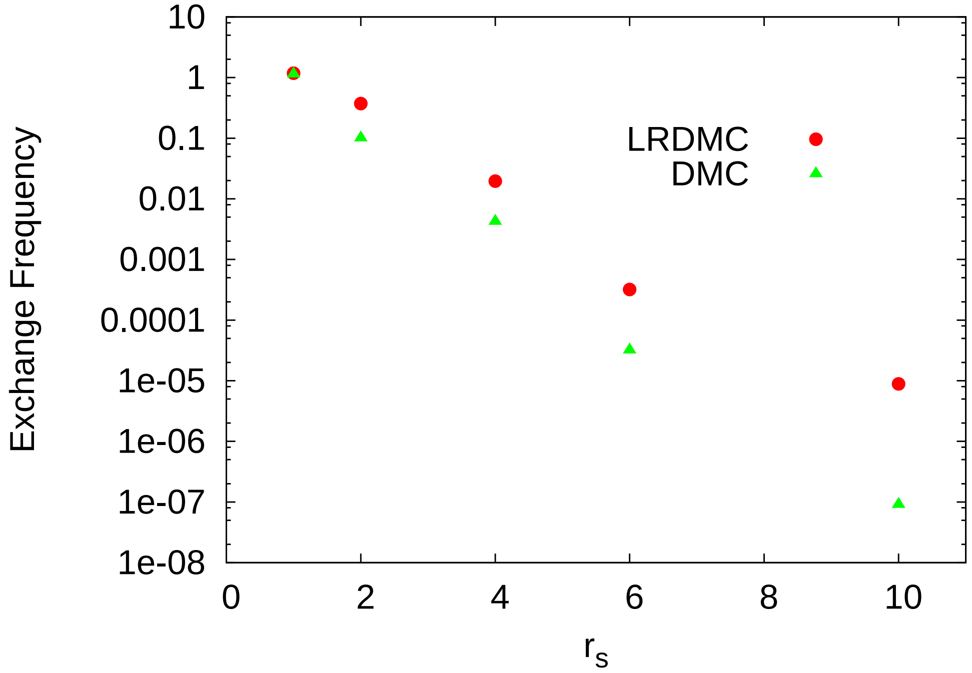

Figure 4.2: Exchange frequency for DMC and LRDMC computed with 22 electrons for several densities.

4.3.1 One Body Corrections

An approximation is made in calculating the kinetic energy using a finite simulation cell. This error is due to the quantization of momentum in a finite size calculation. To understand this error the kinetic energy can be written in terms of the momentum distribution

$$T = \sum_{\mathbf{G}} n_N(\mathbf{G})\mathbf{G}^2 \tag{4.32}$$

where n_N is the momentum distribution of N electrons. Assuming $n_N = n_\infty$ (the momentum distribution in the thermodynamic limit) as the system size grows, the allowed momenta G become more closely spaced and this sum approaches an integral. This error is familiar from mean field calculations where it is necessary to integrate over k points to sample the Brillouin zone. The error made by using a finite number of electrons can now be calculated using the twist averaging method [70]. However in 1D, this may be calculated directly assuming the effective mass of the electrons is one:

$$\Delta T = \int_{-k_F}^{k_F} k^2 d\,k - \sum_G \mathbf{G}^2 \tag{4.33}$$

where $k_F = \frac{\pi}{4r_s}$ is the Fermi momentum of the unpolarized electron gas in the thermodynamic limit and T is the kinetic energy. This correction scales as c/N^2 as the number of electrons in the system N changes where c is a density dependent constant. A more difficult problem arises from the change in n_N as N increases, a many body effect due to electron correlations which is discussed in the next section.

4.3.2 Two Body Corrections

There exist additional many body finite size effects that come from the long wavelength correlations in the electron gas. In this work we use finite size correction by Chiesa *et al.* to calculate the effect on the energy of these long range correlations [69]. In order to calculate these finite size effects, they notice that in a finite size simulation, it is only possible to determine the static structure factor on a finite grid of points given by the reciprocal lattice vectors. They note the majority of the error due to long range correlations comes from the incomplete sampling of the long wavelength portion of the structure factor ($k \to 0$).

Fortunately, the long wavelength behavior of the electron gas is known analytically within the random phase approximation (RPA). Within this approximation the ground state of the system is described by a collection of dressed particles interacting via short range forces and also plasmon collective excitations. In this case the many-body wave function factorizes as

$$\Psi = \Psi_{\text{sr}} \exp\left[-\frac{1}{2\Omega}\sum_{G\neq 0} u_G \rho_G \rho_G^{\dagger}\right], \tag{4.34}$$

where Ψ_{sr} contains only short range correlations and u_G decays quickly to 0 as G increases [71]. Using this knowledge, it is possible to write the difference between the kinetic and potential energy calculated for a finite size simulation cell and the infinite limit:

$$\Delta B = \frac{1}{4\pi}\int_{-\infty}^{\infty} V(k)S(k)dk - \frac{1}{2\Omega}\sum_{i=1}^{\infty} v(k_i)S(k_i) \tag{4.35}$$

$$\Delta T = -\frac{1}{4\pi}\int_{-\infty}^{\infty} k^2 u(k)(S(k)-1) + \frac{1}{2\Omega}\sum_{i=1}^{\infty} k_i^2 u(k_i)(S(k)-1) \tag{4.36}$$

where $V(k)$ is the Fourier transform of the interparticle potential and

$$\tilde{u}(k) = -r_s S_0(k)^{-1} + \sqrt{S_0(k)^{-2} + \frac{\tilde{V}_b(k)}{2r_s k^2}} \tag{4.37}$$

as per the Mean Spherical Approximation (MSA) which becomes equal to the RPA at small k [72]. These corrections both scale as

$$\Delta U \propto \Delta T \propto \frac{\sqrt{\ln N}}{N} \tag{4.38}$$

with system size N which is slower than the one body contributions.

In Fig. 4.3 calculations of the total energy have been performed for several different values of r_s and several different numbers of electrons. In addition, the finite size corrections in Eq. 4.33, Eq. 4.36 and Eq. 4.35 are applied for each number of electrons. These results show that these finite size corrections are quite accurate both for the high density regime where the one body kinetic effects dominate and also for the low density regime where the long range two body effects are the most important. The figures also include a fit of all of the finite size corrections

$$E(N) = E_0 + \frac{c}{N^2} + \frac{c_2\sqrt{\ln N}}{N} \tag{4.39}$$

to the data. The striking agreement between the energy E_0 determined by this fit and the energies calculated using the above corrections is a testament to the power of the method of Chiesa *et al.* to calculate the finite size effects without performing an expensive extrapolation.

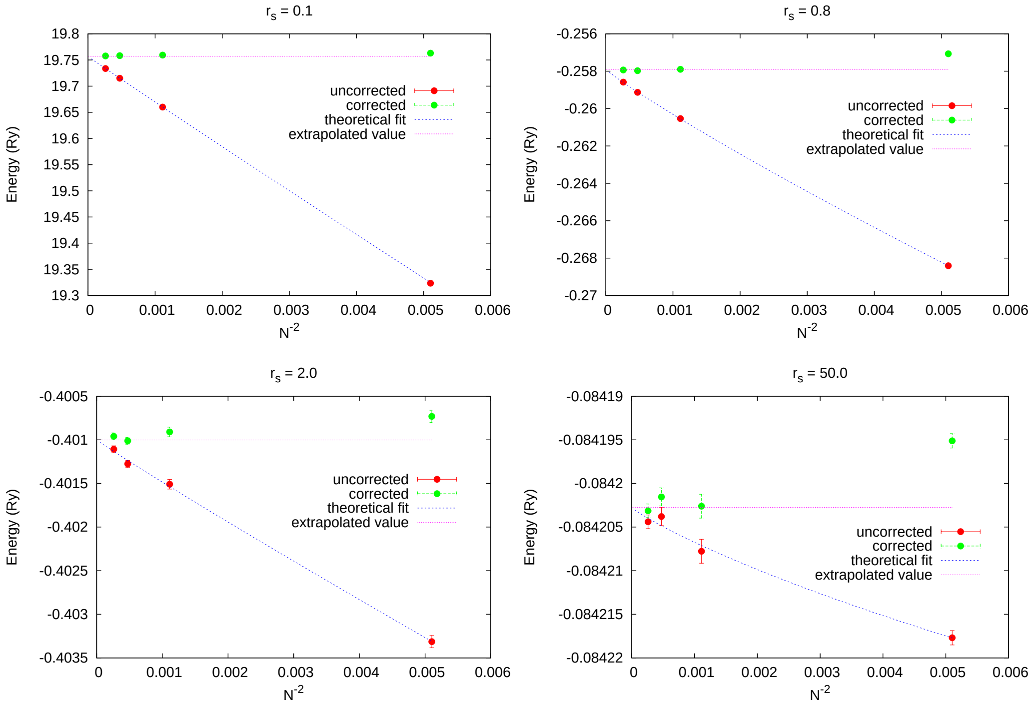

Figure 4.3: Scaling of the ground state energy per particle with number of electrons in the simulation for several densities. The curve shows the extrapolation using both the one body and many body corrections $(E_0 + \frac{c}{N^2} + \frac{c_2\sqrt{\ln N}}{N})$ from Chiesa *et al.*[69]. The green points show the corrected values based on the calculations and the straight horizontal line shows the extrapolated value.

Chapter 5

Correlation Energy and Construction of an LSDA Functional

In this chapter we will endeavor to provide an understanding of the properties of the ground state energy of the quasi one dimensional electron gas as a function of density and spin polarization. This work is a natural extension of that by Casula et. al. who studied the density dependence of the quasi-one dimensional electron gas at zero spin polarization [43]. The chapter will first catalog the theoretically known properties of the electron gas in various limits. With the knowledge of these limits in hand, a careful series of calculations of the total energy of the ground state of the electron gas is undertaken via means of QMC. Finally, a parameterization of this energy suitable for use in DFT calculations is summarized with full details in appendix A.

5.1 Theoretical Constraints on the Total Energy

One of the most powerful predictions about the behavior of the ground state energy of the one dimensional electron gas is the Lieb-Mattis theorem[8]. This simple theorem states that in one dimension the total energy of a system of fermions must be a strictly increasing function of the spin polarization. This theorem precludes the existence of a Bloch instability such as that predicted by an STLS-like theory of the total energy due to Calmels and Gold [73, 74].

This section will also present the theoretical dependence of the total energy on the density and spin polarization in several limits via means of the random phase approximation (RPA) at high density and the mapping of the spin degrees of freedom to the Heisenberg model at low density. In keeping with convention we separate the total energy into three parts:

$$\epsilon = \epsilon_t + \epsilon_x + \epsilon_c \tag{5.1}$$

where ϵ_t is the kinetic energy of the noninteracting system, ϵ_x is the exchange energy calculated for the noninteracting wavefunction and ϵ_c is the correlation energy which includes corrections to both the potential energy and also the kinetic energy due to the interactions. The first two terms are known analytically, with the simplest being the kinetic energy which is

$$\epsilon_t = \frac{\pi^2(1+3\zeta^2)}{48r_s^2}, \tag{5.2}$$

where r_s is the familiar Wigner-Seitz radius and $\zeta = (N^{\uparrow} - N^{\downarrow})/N_{\text{tot}}$ measures the spin polarization of the electron gas. The exchange energy is also known analytically:

$$\epsilon_x = \frac{1+\zeta}{2b}\int_0^{2k_F^{\uparrow}} dk\, \tilde{V}_b(k)(1 - S_0(k, k_F^{\uparrow})) + \frac{1-\zeta}{2b}\int_0^{2k_F^{\downarrow}} dk\, \tilde{V}_b(k)(1 - S_0(k, k_F^{\downarrow})) \tag{5.3}$$

where $S_0(k, k_F)$ is the static structure factor of a noninteracting electron gas with Fermi momentum k_F:

$$S_0(k, k_F) = \theta(k - 2k_F)\frac{k}{2k_F} + \theta(2k_F - k) \tag{5.4}$$

where θ is the step function:

$$\theta(x) = \begin{cases} 1 & \text{if } x < 0 \\ 0 & \text{if } x \geq 0. \end{cases} \tag{5.5}$$

The next two sections will be concerned with finding the behavior of the correlation energy at both high and low densities.

5.1.1 High Density Correlation Energy

The RPA is very successful in describing the energy of the one dimensional electron gas at high density[73, 43]. Here we derive the fully spin dependent RPA for the one dimensional electron gas with the effective interaction from Eq. 3.4.

In a previous work [43], it was shown that the correlation energy at the lowest order in r_s in the unpolarized wire is

$$\epsilon_c^{RPA}(r_s, \zeta = 0) = -\frac{A}{\pi^4 b^2} r_s^2, \tag{5.6}$$

with $A = b^2 \int_0^{+\infty} dz\ z\ \tilde{V}_b^2(z) = 4.9348$, where ζ measures the wire polarization.

This result turns out to be the same as a high density extrapolation of the correlation energy for the same interaction studied here, obtained by Gold and Calmels within the mean spherical approximation (MSA).[73] We obtained the result in Eq. 5.6 starting from the general expression of the RPA correlation energy[75]:

$$\begin{aligned} \epsilon_c^{RPA} &= \frac{L}{2\pi} \int_{-\infty}^{+\infty} dk\ \epsilon(k), \\ \epsilon(k) &= \frac{1}{4\pi} \frac{|k|}{N} \int_{-\infty}^{+\infty} d\lambda\ \ln(1 - \tilde{V}_b(k)\chi^0(k, ik\lambda)) \\ &\quad + \tilde{V}_b(k)\chi^0(k, ik\lambda), \end{aligned} \tag{5.7}$$

where $\tilde{V}_b(k)$ is the Fourier transform of the potential, and χ^0 is the real part of the density-density response function for the free 1D electron gas. We extend the previous work by computing the RPA correlation energy in the presence of polarization, χ^0 must include now the explicit contribution from the two spin species:

$$\begin{aligned} \chi^0(k, \omega) &= \chi^0_\uparrow(k, \omega) + \chi^0_\downarrow(k, \omega) \\ \chi^0_\sigma(k, \omega) &= \frac{1}{4\pi k} \ln\left(\frac{\omega^2 - (k^2 - v_F^\sigma k)^2}{\omega^2 - (k^2 + v_F^\sigma k)^2}\right), \end{aligned} \tag{5.8}$$

with v_F^σ the Fermi velocity of the σ (=$\uparrow, \downarrow$) component. After some algebra, and a change of variables ($k = k_F q$,$\omega = i k_F q v_F u$), Eq. 5.7 can be rewritten at the leading order in r_s as follows:

$$\begin{aligned} \epsilon_c^{RPA} &\simeq -\frac{1}{8(2\pi)^3} \int_0^{+\infty} dq\ q\ \tilde{V}_b^2\left(\frac{q}{\alpha r_s}\right) \\ &\quad \int_0^{+\infty} du (Q_q^\uparrow(u) + Q_q^\downarrow(u))^2, \end{aligned} \tag{5.9}$$

with $\alpha = 4/\pi$ in 1D. The derivation reported in Ref. [43], follows the work of Gell-Mann and Brueckner [76] in 3D, and Rajagopal and Kimball [77] in 2D. The "propagator" $Q_q^\sigma(u)$ now depends on the spin polarization, and reads:

$$\begin{aligned} Q_q^\sigma(u) &= \int_{-\infty}^{+\infty} dk \int_{-\infty}^{+\infty} dt \; f_\sigma(k)(1 - f_\sigma(k+q)) \\ & \quad e^{-ituq} \exp(-|t|(\frac{1}{2}q^2 + kq)), \end{aligned} \tag{5.10}$$

where $f_\uparrow(x) = \theta(|x| - (1+\zeta))$, $f_\downarrow(x) = \theta(|x| - (1-\zeta))$ are the zero temperature Fermi distributions for the two spin components, θ being the step function.

In order to factor out explicitly the r_s order dependence in Eq. 5.9 we apply another change of variables ($q \longrightarrow \alpha r_s q$) and we integrate over u. After these steps, the RPA correlation energy reads:

$$\begin{aligned} \epsilon_c^{RPA}(r_s, \zeta) &\simeq -\frac{1}{8(2\pi)^3} (\alpha r_s)^2 \int_0^{+\infty} dz \; z \; \tilde{V}_b^2(z) \\ & \quad \sum_{\sigma,\sigma'} F_{\sigma,\sigma'}\left(\frac{\alpha r_s}{b} z, \zeta\right), \end{aligned} \tag{5.11}$$

where we have defined the set of functions:

$$\begin{aligned} F_{\sigma,\sigma'}(q, \zeta) = \frac{2\pi}{q} \int_{-\infty}^{+\infty} & dk_1 f_\sigma(k_1)(1 - f_\sigma(k_1)) \\ & \int_{-\infty}^{+\infty} dk_2 f_{\sigma'}(k_2)(1 - f_{\sigma'}(k_2)) \frac{1}{q^2 + q(k_1 + k_2)}, \end{aligned} \tag{5.12}$$

where the ζ dependence is included in the zero temperature Fermi distributions $f_\sigma(k)$. From the above equation it is apparent that $F_{\downarrow,\uparrow} = F_{\uparrow,\downarrow}$.

For $\zeta = 1$, $F_{\uparrow,\uparrow}(q, 1) \neq 0$, while $F_{\downarrow,\downarrow}(q, 1) = F_{\uparrow,\downarrow}(q, 1) = 0 \; \forall q$. Therefore, in the case of the fully polarized 1DEG, at the leading order in r_s we obtain :

$$\epsilon_c^{RPA}(r_s, 1) \simeq -\frac{1}{8(2\pi)^3} (\alpha r_s)^2 \int_0^{+\infty} dz \; z \; \tilde{V}_b^2(z) F_{\uparrow,\uparrow}(0, 1). \tag{5.13}$$

Notice that we have performed the limit $r_s \to 0$ of $F_{\uparrow,\uparrow}\left(\frac{\alpha r_s}{b} z, \zeta\right)$, and it is easy to show that $F_{\uparrow,\uparrow}(0, 1) = \pi/2$. Therefore, our fully polarized RPA correlation energy reads:

$$\epsilon_c^{RPA}(r_s, \zeta = 1) = -\frac{A}{8\pi^4 b^2} r_s^2, \tag{5.14}$$

reproducing the result of Casula *et al.* [43].

To evaluate $E_c^{RPA}(r_s,\zeta)$ at intermediate polarizations, we need to compute the limits:

$$\lim_{x\to 0} F_{\sigma,\sigma'}(x,\zeta) \quad \text{with } \zeta < 1. \tag{5.15}$$

It turns out that $F_{\uparrow,\uparrow}(0,\zeta) = \pi/(1+\zeta)$, $F_{\uparrow,\downarrow}(0,\zeta) = \pi$, and $F_{\downarrow,\downarrow}(0,\zeta) = \pi/(1-\zeta)$. Thus, our final result for the spin dependent RPA correlation energy is the following:

$$\epsilon_c^{RPA}(r_s,\zeta) = \begin{cases} -\frac{A}{2\pi^4 b^2}(1+\frac{1}{1-\zeta^2})r_s^2 & \text{if } 0 \le \zeta < 1 \\ -\frac{A}{8\pi^4 b^2} r_s^2 & \text{if } \zeta = 1 \end{cases} \tag{5.16}$$

Notice that when $\zeta = 0$ we recover the RPA correlation energy for the unpolarized 1DEG in Eq. 5.6, calculated in the previous paper[43]. On the other hand, in the limit $\zeta \to 1$ the coefficient of the leading term (r_s^2) diverges as $1/(1-\zeta)$. This is not surprising, since a non analytic behavior of the RPA correlation energy for $\zeta \to 1$ is present also in 2D[78] and 3D[79]. In these higher dimensions the correlation energy is continuous as $\zeta \to 1$, while its first derivative with respect to ζ is diverging. This behavior is reproduced accurately in the correlation energy parameterization of appendix A. Thus the non-analyticity is stronger as the dimensionality is reduced. In any case, the pathological behavior in 1D deserves an accurate analysis. We take into account the function $F_{\downarrow,\downarrow}(q,\zeta)$, where the $1/(1-\zeta)$ divergence comes from. For $q \ge 0$, and $0 \le \zeta \le 1$, its analytic form is:

$$F_{\downarrow,\downarrow}(q,\zeta) = \frac{4\pi}{q^2}\left(X^+ \ln\frac{2X^+}{X^+ + X^-} + X^- \ln\frac{2X^-}{X^+ + X^-}\right), \tag{5.17}$$

with $X^+ = q/2 + 1 - \zeta$, and $X^- = |q/2 - (1-\zeta)|$. As already mentioned, $F_{\downarrow,\downarrow}(q,1) = 0 \ \ \forall q$, while $F_{\downarrow,\downarrow}(0,\zeta) = \pi/(1-\zeta)$ for $\zeta < 1$. In the (q,ζ) domain with $q \ge 0$, and $0 \le \zeta \le 1$, the function $F_{\downarrow,\downarrow}(q,\zeta)$ is non analytic for $q = 2(1-\zeta)$, which is a line of cusps. Therefore a Taylor expansion of $F_{\downarrow,\downarrow}$ around $(q = 0, \zeta < 1)$ is possible, but its radius of convergence given by $2(1-\zeta)$ is getting smaller as $\zeta \to 1$. This means that the behavior $-\frac{A}{2\pi^4 b^2}(1+\frac{1}{1-\zeta^2})r_s^2$ of the correlation energy is valid for $\zeta < 1$ in a region where $r_s << 2(1-\zeta)b/\alpha$. Outside this region the asymptotic behavior of the RPA correlation energy breaks down and one must compute the integral in Eq. 5.11 with the full dependence of $F_{\sigma,\sigma'}\left(\frac{\alpha r_s}{b}z,\zeta\right)$ on its first argument. In other words, one needs to include higher order terms in the RPA expansion.

5.1.2 Low Density Correlation Energy

The low density dependence of the correlation energy can be determined approximately by noting that the spin dependence of the one dimensional electron gas can be mapped to that of a Heisenberg spin chain[80]. The reason for this mapping is that in low density the electron gas occupies a locally antiferromagnetic Wigner lattice[13]. In fact at these densities the electron gas has strong quasi Wigner crystal correlations as discussed in Ch. 6. This result is confirmed by our calculations of the spin dependent density-density correlation function shown for $b = 1$, $r_s = 4$ using LRDMC in Fig. 5.1.

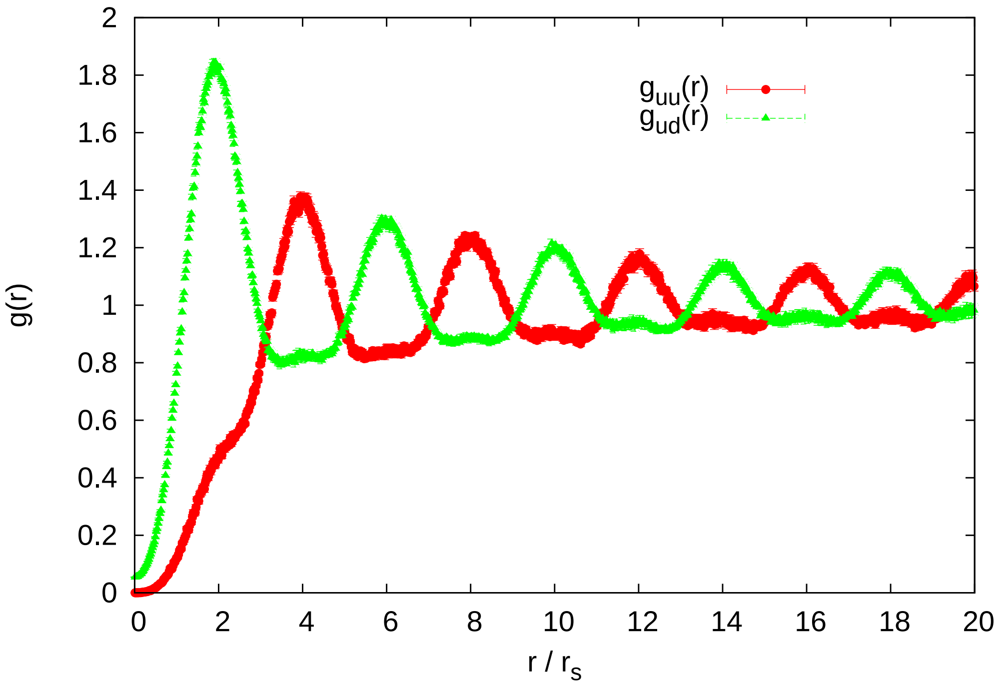

Figure 5.1: Density-density correlation function, $g(r)$, between electrons of like spin ($g_{uu}(r)$) and unlike spin ($g_{ud}(r)$). The peaks of the correlation functions occur at alternate multiples of the mean interparticle spacing ($2r_s$), suggesting a locally antiferromagnetic Wigner lattice of electrons.

The coupling of this Heisenberg spin chain can be determined by noting that on this lattice electrons can only exchange by tunneling between lattice sites. This tunneling can be calculated within the WKB approximation as is detailed in Sec. 9.2.1. This quantum tunneling will be exponentially suppressed at low density and so the form of the coupling as a function of density is[81]:

$$J(r_s) = \frac{J^\star}{r_s^{1.25}} e^{-\nu\sqrt{r_s}} \tag{5.18}$$

where $J^\star$ and ν are interaction dependent constants.

The energy dependence of the antiferromagnetic Heisenberg spin chain is known from theory to be

$$E(\zeta) = \frac{\pi}{2}\left(1 + \frac{1}{2\ln\zeta}\right)\zeta^2 \tag{5.19}$$

plus higher order terms[82]. Also the difference in energies between the polarized and unpolarized spin chains is $J(1+\ln 2)$[83]. These calculations define the spin dependence of the total energy of the electron gas at low density.

At low density the correlation energy must cancel the power law and logarithmic terms in spin dependence of both the exchange and kinetic terms above in order to provide the exponentially small spin dependence given by Eq. 5.19. Assuming that there are no spin independent terms in this correlation energy, this means that to the first two orders in r_s, the correlation energy must scale as

$$\lim_{r_s\to\infty} \epsilon_c(r_s) = \frac{C}{r_s^2} + \frac{C_2 \ln r_s}{r_s}, \tag{5.20}$$

at fixed ζ where the prefactors C and C_2 are determined by the low density behavior of the kinetic and exchange energies. It is also possible to use this information to make an assumption for the density dependence of the total energy at low density: $\epsilon \approx C \ln r_s / r_s$. This approximation does not hold exactly for the electron gas, suggesting that there are some polarization independent terms in the low density limit of the energy. This result was found previously for $\zeta = 0$ by Casula *et al.* [43].

5.2 QMC Calculations of Total Energy

Great care is taken to remove all biases in the calculation of the energy in the thermodynamic limit via QMC. First the finite lattice space error is removed by calculating the energy for several numbers of electrons at several lattice spacings and fitting the result to

$$E(a) = E + ca^2, \tag{5.21}$$

where E is the energy in the limit of zero lattice spacing, a is the lattice spacing and c is an arbitrary constant. Using this methodology, the energy is calculated for several different numbers of electrons and the result is extrapolated to the thermodynamic limit both by directly calculating the finite size corrections in Sec. 4.3 and by fitting the data to a form with free parameters given by calculating the finite size effects using the MSA Jastrow wavefunction

$$E(N) = E + \frac{c\sqrt{\log N}}{N^2} + \frac{c_2}{N^2}, \tag{5.22}$$

where E is the energy extrapolated to the thermodynamic limit N is the number of electrons in the calculation and the constants c and c_2 are fitting parameters determining the size of the one-body and two-body finite size corrections. Additionally the number of electrons N is chosen in each calculation so that the number of electrons in each spin species is odd, thus avoiding degeneracy effects. These two methods agree well for a wide range of densities and spin polarizations as shown in Fig. 4.3.

The results of these calculations yield a series of total energies as a function of density and spin polarization. Calculations have been performed for $b = 0.1, 1, 2$ and $b = 4$ for densities from $r_s = 0.1$ to 50.0 at $\zeta = 0, 0.25, 0.5, 0.75$ and 1. The results of these calculations are summarized by Fig. 5.2 and Fig. 5.3 which show the behavior of the correlation energy as a function of the density and the polarization respectively. These calculations show a good agreement with the theory in Sec. 5.1. Specifically, correlation energy at high density ($r_s = 0.1$) as a function of the polarization shows vestiges of the discontinuity in the correlation energy at $\zeta = 1$ (Eq. 5.16). The density dependence for each polarization also agrees well with the quadratic behavior in r_s predicted by the RPA.

5.3 Parameterization of Correlation Energy

We have developed two parameterizations of the energies presented in section 5.2. One of these gives a functional form for the correlation energy as a

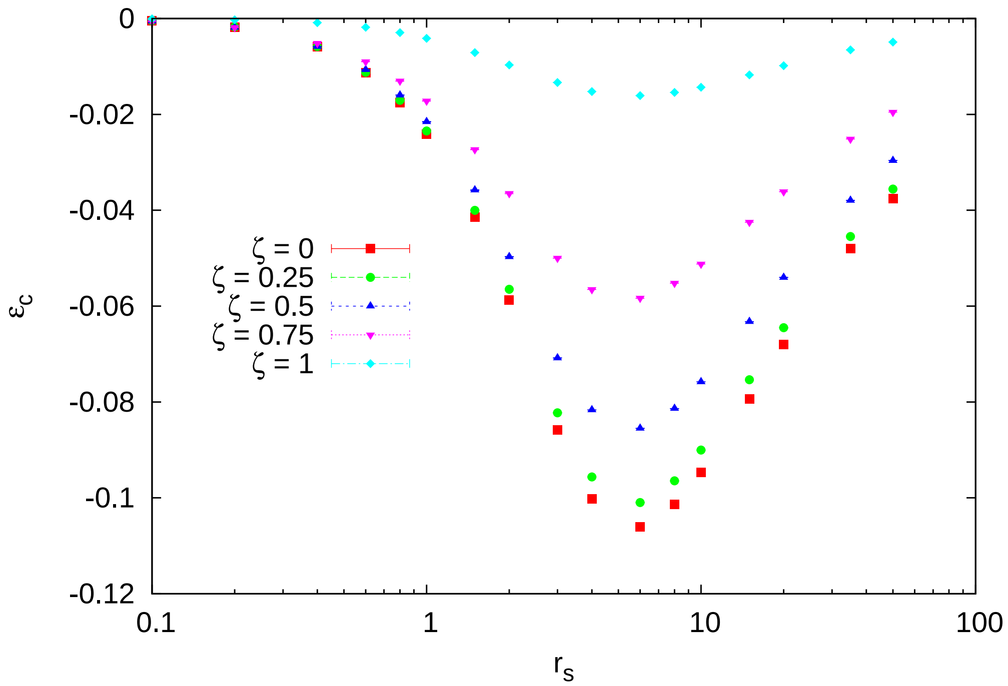

Figure 5.2: The correlation energy of the electron gas as a function of the density r_s is plotted for $b = 1$ at five values of the polarization, ζ. The correlation energy shows a quadratic behavior in the high density limit as a function of r_s as predicted by the RPA.

function of r_s and ζ and has an excellent agreement with all of the theoretical predictions in the high density limit. The other parameterization yields a functional form of the sum of the exchange and correlation energies. This functional form is able to reproduce the exponential low density decay of the spin susceptibility as well as the density dependence of the total energy at high density. Both of these parameterizations provide an excellent fit to the QMC data with $\chi^2 = 4.33$ for the correlation parameterization and $\chi^2 = 9.97$ for the exchange correlation parameterization. The functional forms and other details of these parameterizations is given in appendix A.

These parameterizations do suffer from theoretical difficulties as well in various limits with both violating at least one of the limits obtained in Sec. 5.1. The total energy obtained from the correlation functional violates the Lieb-Mattis theorem at low density and the exchange correlation functional exhibits unphysical oscillations in the correlation energy near $\zeta = 1$ at high density. For this reason these parameterizations may only be recommended for use in DFT calculations with caveats. The correlation functional

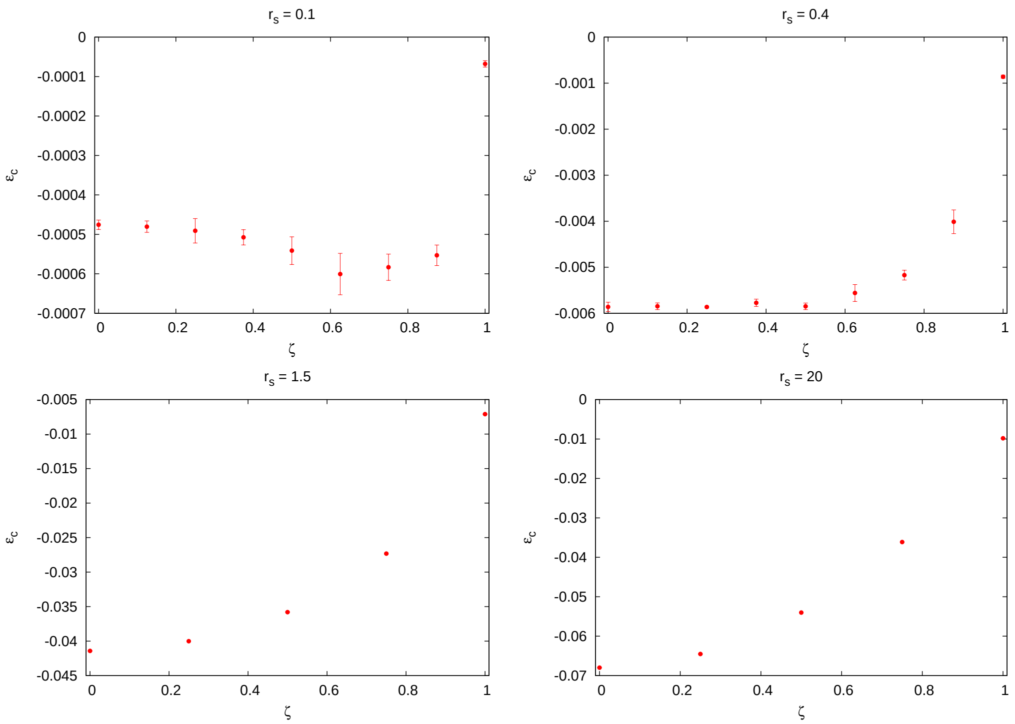

Figure 5.3: The correlation energy of the electron gas as a function of the polarization ζ is plotted for $b = 1$ at four values of the density, r_s. The upper right panel shows evidence of the RPA behavior, quadratically as a function of ζ near $\zeta = 0$ and then assuming a vastly different value at $\zeta = 1$. The upper right and lower left panels show the intermediate case where the RPA behavior is giving way to a spin dependence that allows for an exponentially small spin velocity. The lower right panel shows the ζ dependence at low density.

should be used only if the density remains greater than $r_s \approx 4$ for the entire system under interest. Likewise calculations using the exchange correlation functional should take care the polarization of the electron gas does not exceed 0.5 for densities greater than $r_s = 0.4$.

Nevertheless these functionals are successful in determining the charge compressibility as a function of the density. These results are presented in Fig. 9.1 where the compressibility determined from the correlation function as

$$\chi_\rho = 1/\frac{\partial^2 \epsilon}{\partial r_s^2} \tag{5.23}$$

is found to be in very good agreement with the compressibility determined from the long wavelength excitations of the electron gas. The results found using the exchange correlation functional lay on top of the solid line in

Fig. 9.1. The spin velocity determined from the second derivative of the total energy with respect to ζ using the exchange correlation functional is also in good agreement with the spin velocities calculated both using the WKB approximation and the long wavelength spin excitations.

Chapter 6

Quasi Wigner Crystal Crossover

In two and three dimensions, Wigner found that that as the density of the electron gas decreases, the potential energy of the electron gas which scales as $1/r_s$ will eventually dominate the kinetic energy which scales as $1/r_s^2$ [84]. In this regime the electrons crystallize in order to minimize their potential energy, a state which is known as a Wigner crystal. In one dimension the situation is different. The one dimensional electron gas does not undergo any phase transitions as the density is varied because of the increased importance of quantum and thermal fluctuations in one dimension [85]. A seminal work by Schulz shows that when long range interactions are included within the bosonization framework, a quasi Wigner Crystal order appears in one dimension[10]. In this chapter we will present the theory of the quasi Wigner Crystal derived by Schulz and then will perform QMC calculations to observe these correlations in the one dimensional electron gas. While Schulz argues that these correlations are present at all densities, we find that the strength of the quasi Wigner Correlations becomes effectively zero at high density and there is a crossover behavior as the density decreases.

6.1 Theory of the Quasi Wigner Crystal

Schulz begins with a second quantized Hamiltonian where the dispersion has been linearized around the Fermi points.

$$\hat{H} = \sum_{k,\sigma} \left[(k - k_F)\hat{n}^L_{k,\sigma} + (-k - k_F)\hat{n}^R_{k,\sigma} \right] v_F + \frac{1}{2L}\sum_q V(q)\hat{n}_q\hat{n}_{-q} + \hat{H}_{bs} \quad (6.1)$$

where $\hat{n}^{L,R}_{k,\sigma}$ is the number operator for left (right) moving electrons with momentum k and spin σ and $\hat{n}_q$ is the Fourier component of the total particle density. $\hat{H}_{bs}$ describes the processes that scatter the electrons from the left to the right moving branches and vice versa. The linear energy-momentum relation in Eq. 6.1 makes it soluble with the Bosonization technique. In this case, that means introducing the phase fields

$$\phi_\nu = -\frac{i\pi}{L}\sum_{p\neq 0}\frac{1}{p}e^{-ipx}\left[\nu^R(p)+\nu^L(p)\right] \tag{6.2}$$

where $\nu(p) = \rho(p), \sigma(p)$ are the usual charge or spin density operators. This transformation allows the Hamiltonian to be split into commuting parts for the charge and spin degrees of freedom. In this case the charge piece is of particular interest:

$$\begin{aligned}\hat{H}_\rho = {} & \frac{v_F}{2\pi}\int dx\left[\pi^2(1+\tilde{g}_1)\Pi_\rho^2 + (1-\tilde{g}_1)(\partial_x\phi_\rho)^2\right] \\ & + \frac{1}{\pi^2}\int dx\, dx' V(x-x')\partial_x\phi_\rho\partial_{x'}\phi_\rho \end{aligned} \tag{6.3}$$

where Π_ρ is the momentum density conjugate to ϕ_ρ and $\tilde{g}_1$ characterizes the backscattering and involves the matrix element at $q \approx 2k_F$. Again using the Bosonization method the density at a point x can be written using the expression

$$\begin{aligned}\rho(x) = {} & -\frac{\sqrt{2}}{\pi}\partial_x\phi_\rho(x) + \frac{1}{2\pi\alpha}e^{2ik_Fx}e^{-i\sqrt{2}\phi_\rho(x)}\cos\left[\sqrt{2}\phi_\sigma(x)\right] \\ & + Ce^{4ik_Fx}e^{-i\sqrt{8}\phi_\rho(x)} + H.c. \end{aligned} \tag{6.4}$$

where C is an interaction dependent constant. Now the charge-charge correlation function can be written as:

$$\langle\rho(x)\rho(0)\rangle = A_1\cos(2k_F)e^{-c_2\sqrt{\ln x}}/x + A_2\cos(4k_F)e^{-4c_2\sqrt{\ln x}} + \ldots \tag{6.5}$$

where A_1, A_2 and c_2 are interaction dependent factors and only the most slowly decaying Fourier components are given. Schulz concluded that the extremely slow decay (slower than any power law) of the $4k_F$ component of this correlation function corresponded to a charge density wave sort of behavior. Because the periodicity of this charge density wave is the same as the mean interparticle spacing in the electron gas, this has the nature of a quasi Wigner crystal.

The relation in Eq. 6.5 can be Fourier transformed on a finite segment of the wire in our QMC calculations to yield the $4k_F$ component of the static structure factor of the electron gas[44].

$$\int_{c_0}^{L} \mathrm{d}x\ \exp(-i4k_F x)\left\langle \rho(0)\rho(x)\right\rangle = aL\exp(-4c\sqrt{\log L}) + b, \tag{6.6}$$

where we explicitly include the dependence on the system size L by taking the Fourier transform over the simulation cell. The short-distance cutoff c_0 is introduced because the LL theory provides only the asymptotic behavior for $\langle\rho(0)\rho(x)\rangle$. Further logarithmic corrections could be included[86] in Eq. 6.6, but we take just the leading order expansion which should be the most relevant for the system sizes computed here. One would need much larger systems which are beyond our current numerical capabilities to resolve further corrections.

6.2 Calculation of the Quasi Wigner Crystal Correlations

This section uses QMC calculations of the electron gas at several densities to characterize the presence of Quasi Wigner Crystal Correlations in the quasi one dimensional electron gas. All calculations are performed using either LRDMC or DMC and the mixed estimator bias is corrected using the forward walking technique. As indicated in Sec.6.1, the static structure factor is an invaluable tool for analyzing the correlations of the electron gas. The structure factor $S(k) = \frac{1}{N}\langle\rho(-k)\rho(k)\rangle$, where $\rho(k) = \sum_j e^{ikr_j}$ are the Fourier components of the electron density is calculated for several values of r_s and for many different numbers of electrons for $b = 0.1$. The results of these calculations are shown in Fig. 6.1. In all cases, the functional dependence of the structure factor at $4k_F$ agrees with the Bosonization prediction made by Schulz in Eq. 6.6. However, there is no prediction made for the size of the prefactor of these correlations. Although the scaling of the structure factor has previously been calculated in realistic systems[44], to our knowledge this is the first work to systematically study the prefactor.

It is apparent that the $4k_F$ correlations are much more significant for lower densities where the scaling with the number of electrons is readily apparent. Apparently the prefactor determining the strength of these correlations un-

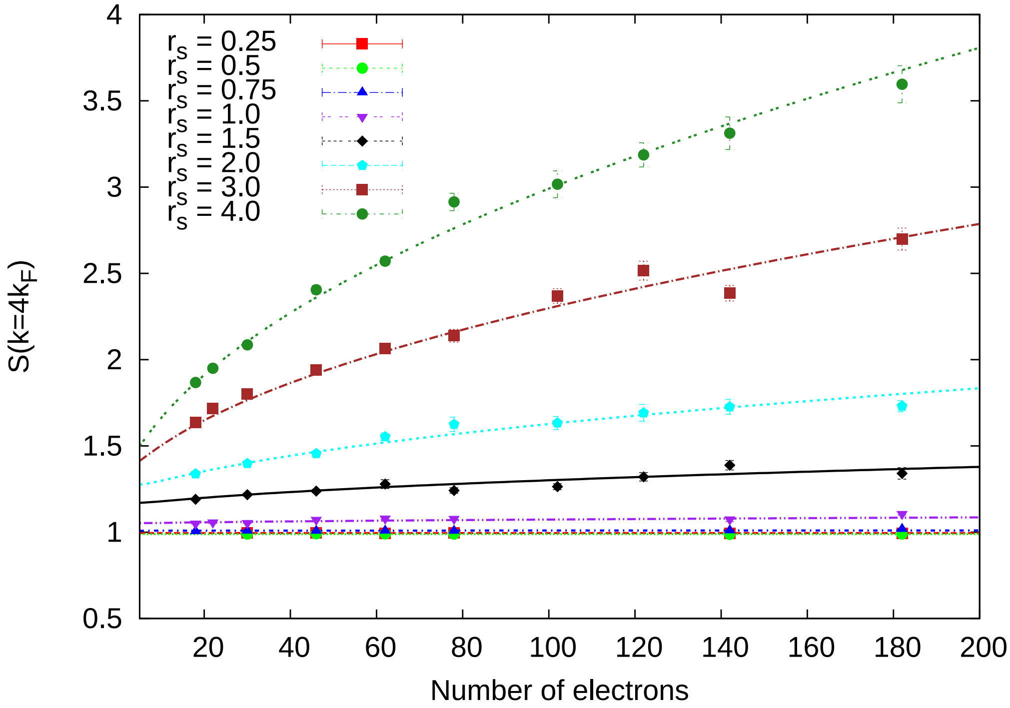

Figure 6.1: Scaling of the $4k_F$ component of the structure factor with respect to the number of particles. The scaling is reported for various densities with $b = 0.1$. The lines are the best fit of the function in Eq. 6.6 given by the LL theory found in Schulz [10].

dergoes a drastic change as the density decreases. Efforts have been made to fit the available data to the form in Eq. 6.6. Although the data agrees with the theory for all densities, it is very difficult to extract the exact values of the various parameters a, b and c because of logarithmic form of the scaling and the limited range of calculations available. The best approximation to the data is presented in Fig. 6.2.

Again, this scaling shows a transition where the correlations at $4k_F$ have a small prefactor at high density and a larger one at low density. The best explanation of this behavior may be found by directly considering the full momentum resolved structure factor. At high density the structure factor is very similar to the MSA prediction $S_{\mathrm{MSA}}(k) = S_0(k)/(1 + 2\rho\tilde{u}(k)S_0(k))$[87] as expected (see Fig. 6.3), since in the limit $r_s \to 0$ the MSA becomes exact [43]. Specifically, there is no peak at $4k_F$ up to $r_s = 0.5$ ($r_s = 0.2$) for $b = 0.1$ ($b = 0.0001$), namely there are no correlations with the mean interparticle spacing (Fig. 6.4). As the density decreases, a peak develops at $4k_F$. This peak is a necessary feature for a one dimensional quasi Wigner crystal and it

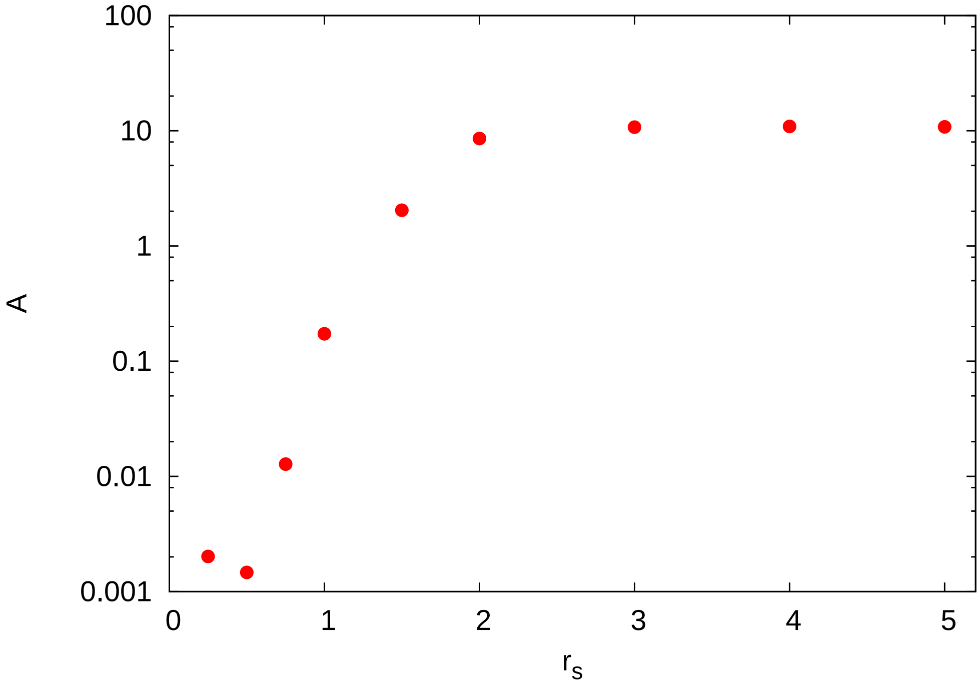

Figure 6.2: Prefactor of the scaling of the $4k_F$ component of the structure factor as given in Eq. 6.6. Calculations are performed for $b = 0.1$. Estimates of the errors on the values are not included because the data set was too small for reliable estimates.

is absent in the MSA prediction which has no structure at $4k_F$. For $b = 0.1$ we carried out simulations with up to 450 particles for $r_s = 0.5$ and $r_s = 0.75$, to check the convergence of the $S(k)$ in the liquid regime close to the onset of the $4k_F$ charge correlations (Fig. 6.4).

6.3 Screening Restores Conventional LL Predictions for Correlations

The quasi Wigner crystal correlations derived by Schulz[10] apply only when the interaction is long range $(1/x)$. In the case of the screened interaction above the potential decays as $4R^2/x^3$ at large distances, so a simple scaling argument shows that the Wigner crystal correlations should be absent at very low densities. Indeed, if $r_s > 8R^2/\pi$ the typical kinetic energy of the electrons, the Fermi energy E_F, is larger than the potential energy computed at the mean interparticle distance $(2r_s)$. At these low densities Matveev[81]

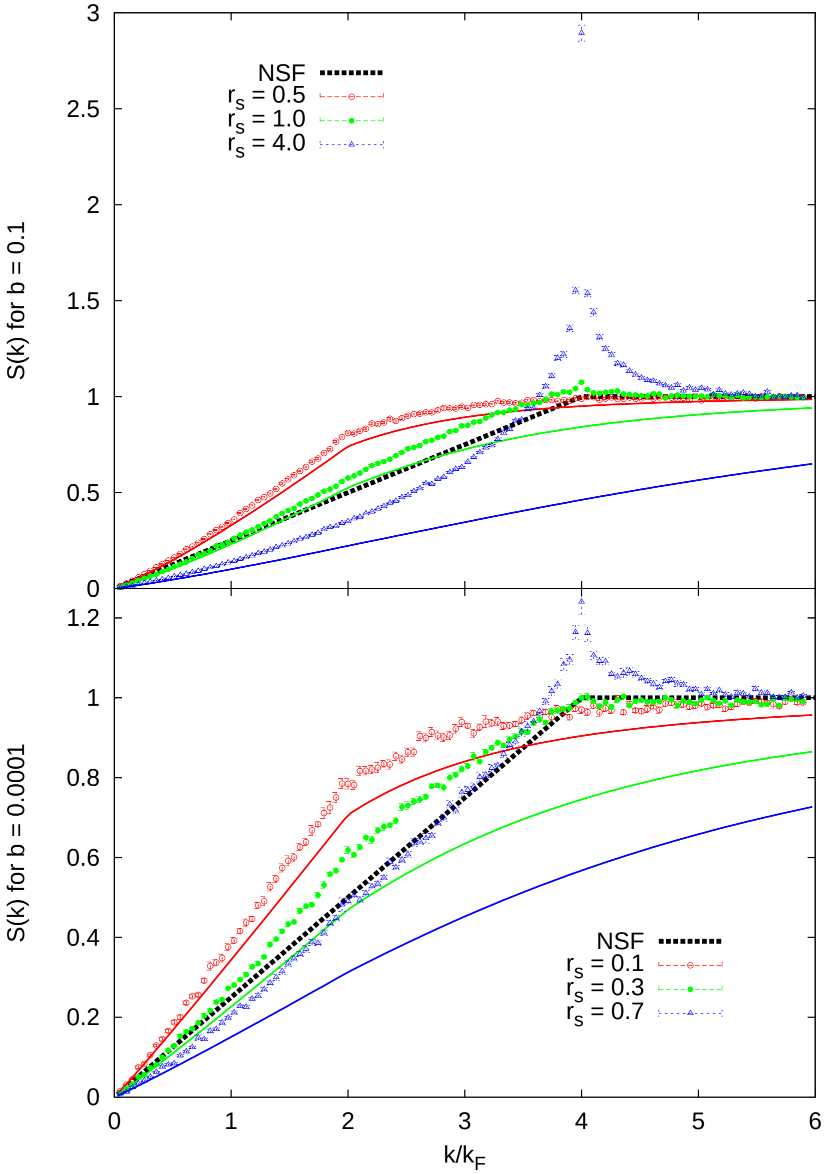

Figure 6.3: Structure factor for $b = 0.1$ (upper panel), and $b = 0.0001$ (lower panel), computed for a system with 78 electrons. The QMC (points) and MSA (solid lines) structure factors are reported for different densities (r_s). Also the noninteracting spinless fermion (NSF) structure factor is drawn (solid black line) for comparison.

has pointed out that it is possible to map the screened short-range interaction into a repulsive contact potential

$$V(x) = U\delta(x), \tag{6.7}$$

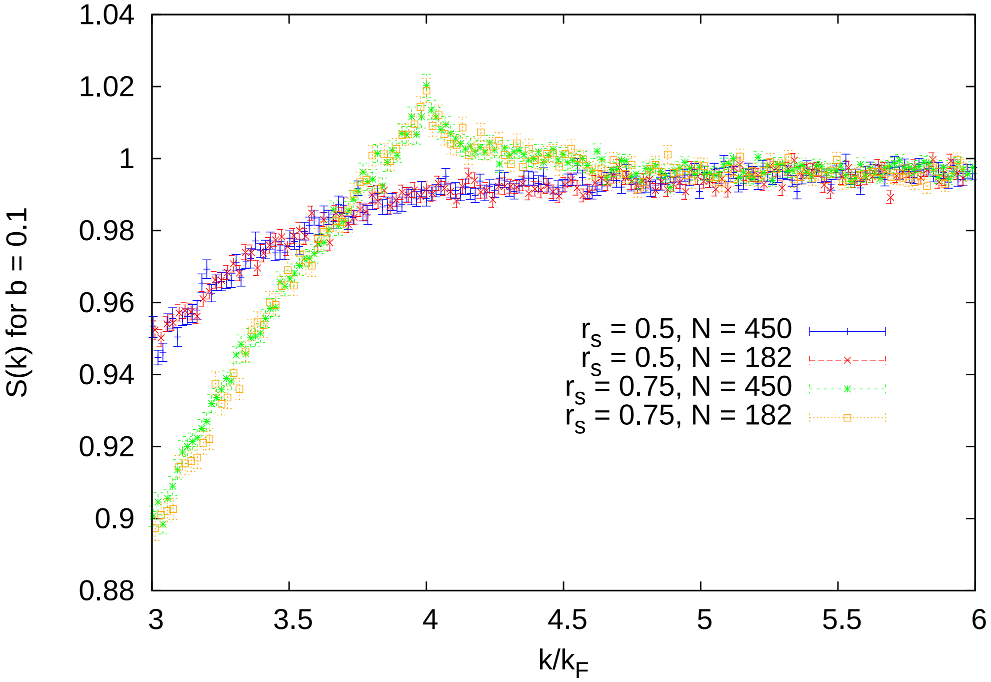

Figure 6.4: Detail for the structure factor near $4k_F$ for $b = 0.1$, computed for $N = 182$ and $N = 450$ at two densities ($r_s = 0.5$ and $r_s = 0.75$) in the proximity of the crossover from a liquid to a quasi-crystal.

where the constant U is chosen so the delta function potential and the screened one have equal transmission coefficients. On the other hand, in the density range $1 \ll r_s < 8R^2/\pi$ the $1/x$ shoulder of the potential can induce $4k_F$ correlations, which are strong but not strong enough to stabilize any sort of quasi-order. Calculations of the finite size scaling of the $4k_F$ peak of the structure factor for $b = 0.1$ and $R = 200$ show the saturation of its height for $N \gtrsim 100$, and so demonstrate the absence of the quasi Wigner crystal correlations when screening is introduced despite quite a large distance to the metallic gate (Fig.6.5). Only in the limit of $R \to \infty$ does one recover the unscreened potential and the possibility for a quasi long-range charge order.

In addition to our work, Hausler *et al.* have studied the case of a screened interaction in one dimension [13]. They used a world line Monte Carlo algorithm to calculate the LL parameters of the electron gas on a lattice for a long range $1/x$ interaction that was screened by a semi infinite metallic gate, just as in our work. The results found were in good agreement with

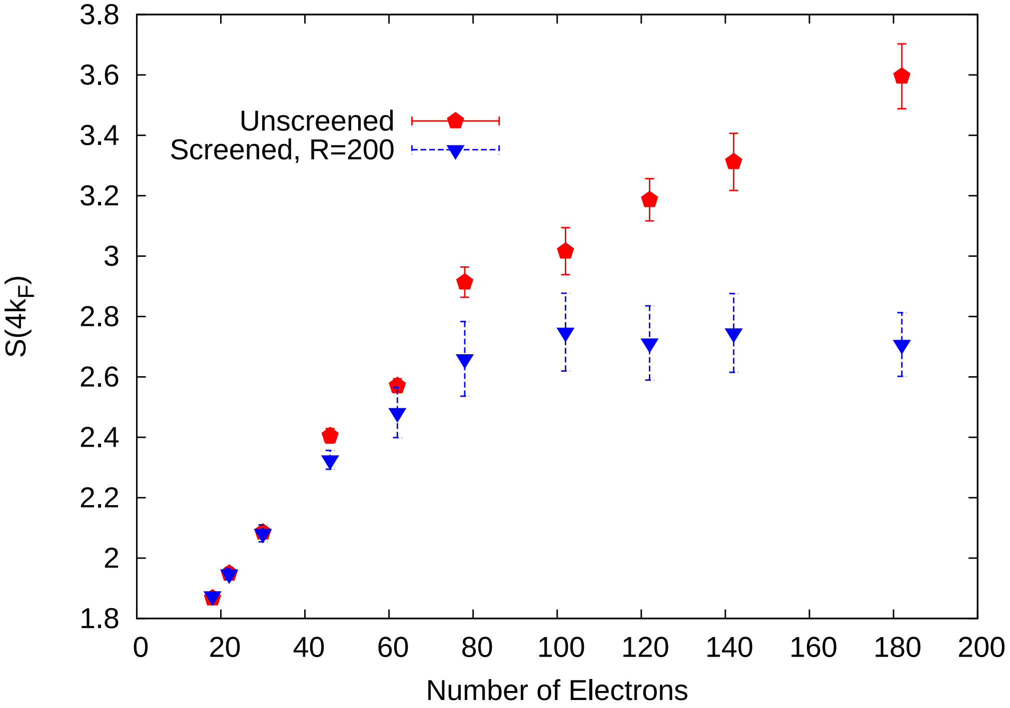

Figure 6.5: Scaling of the $4k_F$ component of the structure factor with respect to the number of particles for $b = 0.1$, and $r_s = 4$. For comparison, the scaling is reported for the unscreened V_b interaction, and the screened potential in Eq. 3.12 with $R = 200$.

the expected behavior, showing a suppression of the spin velocity and an enhancement of the charge velocity which was also good agreement with perturbative estimates at high density.

Chapter 7

Calculating Excited State Energies via QMC

This chapter will discuss three methods for obtaining excited state energies within quantum Monte Carlo. The simplest of these is to simply change the trial wavefunction in a DMC or LRDMC calculation and let the fixed node constraint prevent the wavefunction from collapsing to the ground state [56]. Proceeding in order of sophistication is the transient estimate (TE) method[88] which attempts to extract the excited state energies from the imaginary time behavior of the simulation. Finally, the correlation function Monte Carlo method (CFMC)[89] allows the energy for the excited states to be calculated by projecting a set of trial excited state wavefunctions in imaginary time and diagonalizing the resulting basis. This chapter will compare the relative benefits of these methods for calculating the momentum resolved excitation energies of the one dimensional electron gas.

7.1 Fixed Node Excited State Energies

The simplest method of computing the excited state energy with a DMC or LRDMC calculation is to change the trial wave function so that it has a different nodal surface than the ground state. The projection nature of DMC and LRDMC cause these methods to find the lowest state consistent with the provided nodal surface. The difference in symmetry between the excited state wave function and the ground state wavefunction causes the Monte Carlo procedure to find the lowest energy state consistent with the excited state rather than the ground state when an excited state trial wavefunction is used. This method has been used extensively throughout the QMC literature (eg. [56, 90, 91, 92]). In one dimension this task is simplified because the nodes of the ground state wave function are commensurate with the nodes of all of the excited state wave functions. This is the case because the nodes of the ground state are fully determined by the coincidence points where electrons of the same spin are at the same location. The antisymmetry of the wavefunction requires that these points be nodes in any dimension for any wave function, be it a ground or excited state. While this is true in higher dimensions, the nodal structure of both the ground state and excited states is much more complicated and there is no guarantee that the nodes of the ground state wave function must be contained in the nodes of the excited state. A complication for calculating excitation energies in one dimension is the desire to calculate the full momentum resolved excitation spectrum. Using this method such a calculation would entail a separate QMC calculation for each excitation momentum. For this reason other methods are used in this dissertation.

7.2 Transient Estimate

The transient estimate method was originally proposed as an attempt to circumvent the fixed node approximation in Diffusion Monte Carlo calculations [93, 94]. This approach uses the imaginary time dynamics of the total energy to determine the ground state energy before the variance becomes too large. Depending on the quality of the trial wavefunction, this method could improve on the energy calculated within the fixed node approximation because it does not require the projection to converge, and could thus in principle use the small time data unspoiled by the sign problem to determine the energy.

The TE method was recently used by Yamamoto to calculate the momentum resolved excitation energies of a one dimensional electron gas on a lattice [88]. The central idea of this method is that it is possible to use the imaginary time behavior of a Monte Carlo calculation to extract the energy of the low lying excited states by comparing the imaginary time behavior of a wavefunction orthogonal to the ground state, $|\Psi_e\rangle$, to the imaginary time behavior of the ground state.

$$\frac{\langle\Psi_e|\, e^{-\tau H}\,|\Psi_e\rangle}{\langle\Psi_0|\, e^{-\tau H}\,|\Psi_0\rangle} = \sum_{i=1} |\langle\Psi_e|\Psi_i\rangle|^2\, e^{-\tau(\epsilon_i - \epsilon_0)}, \tag{7.1}$$

where $|\Psi_i\rangle$ is the wavefunction of the i'th excited state and ϵ_i is its energy. In practice, this can be found in a DMC or LRDMC calculation by using the forward walking technique [67]. In that technique, the trial wavefunction guiding the random walk is Ψ_T, and the configurations $\mathbf{R}$ are taken from the equilibrated part of the run. Using this procedure, the imaginary time behavior is found to be:

$$\sum_{i=1} \left|\langle\Psi_e|\Psi_i\rangle\right|^2 e^{-\tau(\epsilon_i-\epsilon_0)} = \sum_t \left\langle \frac{\Psi_e(\mathbf{R},t+\tau)}{\Psi_T(\mathbf{R},t+\tau)} \mathcal{W}(t,\tau) \frac{\Psi_e(\mathbf{R},t)}{\Psi_T(\mathbf{R},t)} \right\rangle_{\Psi_0\Psi_T} . \quad (7.2)$$

where $\mathcal{W}(t,\tau) = \Pi_{i=t}^{t+\tau} w_i$ is the product of each walker's weights between the time-step t and $t+\tau$ and $\Psi(\mathbf{R},t)$ is the wavefunction evaluated with configuration $\mathbf{R}$ at time-step t.

In practice this is useful because a single QMC calculation can be used to calculate the energies of excited states with several momenta $\{k\}$ simply by changing the wavefunction Ψ_e during the forward walking. In the case of the electron gas we used a wavefunction first proposed by Feynman in his work on liquid helium [95]. This wavefunction merely multiplies a density (or spin) oscillation onto the ground state of the interacting system

$$|\Psi_e\rangle = \rho(k)\,|\Psi_0\rangle\,, \quad (7.3)$$

where $\rho(k) = \sum_j e^{ikr_j}$. In this case as the projection time τ goes to infinity

$$\epsilon_k - \epsilon_0 = \lim_{\tau\to\infty} -\frac{\partial}{\partial\tau} \ln \frac{\langle\Psi_T|\,\rho(k)e^{-\tau H}\rho(-k)\,|\Psi_0\rangle}{\langle\Psi_T|\,e^{-\tau H}\,|\Psi_0\rangle}. \quad (7.4)$$

where ϵ_k is the energy of the lowest lying excited state with momentum k.

The primary difficulty with this method is that the noise in the forward walking grows exponentially with the projection time. Therefore, it can be difficult to take the limit $\tau \to \infty$. The rate of convergence of the energy in Eq. 7.4 with propagation time τ is governed by two factors. The first of these is that the energy converges faster when the overlap of the trial wavefunction (in this case Eq. 7.3) with the lowest energy excited state is large. The second condition is that the convergence of Eq. 7.4 is fastest when the gap between the lowest energy and second lowest energy excited states is large.

In our case, the Feynman ansatz is a better approximation to the lowest energy excited state wavefunction for long wavelength excitations causing our simulation to converge faster for these small k excitations. Also, governing the convergence is the gap between the lowest and next lowest energy excitations with a given momentum. In the thermodynamic limit there is a continuum of excitations for each momentum so the TE method would converge extremely slowly. However, in a finite system there is a gap between the energies of the excitations which is proportional $1/N$. This results in an increased rate of convergence for smaller systems whose usefulness is partially offset by a finite size bias that will be explored in detail in section 7.4.

7.3 Correlation Function Monte Carlo

This method is based on the idea that it is possible to compute the excitation spectrum of a system in a direct and variational way by projecting an initial set of basis functions in imaginary time to determine the lowest energy excitations of the system. As in section 7.2 this method utilizes a forward walking procedure to calculate the excited state energies from the distribution of configurations obtained via QMC for the ground state. In this method, rather than using the imaginary time dependence directly, the Hamiltonian and overlap matrices are calculated for a basis of trial excited states which are projected in imaginary time.

Our discussion of the CFMC method follows Ceperley and Bernu [89]. This method has its underpinnings in variational calculations of the excited state energies given a basis of known functions $\phi_i(\mathbf{R})$. Given this set of functions, the best estimate of the excited state energies of the Hamiltonian occurs at the stationary points of the Rayleigh quotient

$$\Lambda_i = \frac{\int d\mathbf{R} \sum_j a_{i,j}\phi_j(\mathbf{R})\hat{H}\sum_k a_{i,k}\phi_k(\mathbf{R})}{\int d\mathbf{R}\sum_{j,k} a_{i,j}a_{i,k}\phi_j(\mathbf{R})\phi_k(\mathbf{R})} \tag{7.5}$$

with respect to $a_{i,j}$. The approximate eigenvalues Λ_i determined by this procedure are upper bounds to the exact eigenvalues via MacDonald's theorem rendering the method variational [96].

The CFMC method builds on the above method by projecting the initial wave functions $\{\phi_i(\mathbf{R})\}$ in imaginary time with $e^{-\tau\hat{H}}$ and then solving the generalized eigenvalue problem in Eq. 7.5. We write this as a linear system of equations where the matrix N contains the overlap of the basis functions as they are projected

$$N_{j,i}(\tau) = \int d\mathbf{R}\, d\mathbf{R}'\, \phi_j(\mathbf{R}')\, \langle\mathbf{R}'|\, e^{-\tau\hat{H}}\, |\mathbf{R}\rangle\, \phi_i(\mathbf{R}), \tag{7.6}$$

and H the matrix element of the Hamiltonian with the projected basis functions,

$$H_{j,i}(\tau) = \int d\mathbf{R}\, d\mathbf{R}'\, \phi_j(\mathbf{R}')\, \langle \mathbf{R}'|\, \hat{H} e^{-\tau \hat{H}}\, |\mathbf{R}\rangle\, \phi_i(\mathbf{R}). \tag{7.7}$$

Now the estimates of the excited state energies are found by solving the generalized eigenvalue problem

$$\mathbf{H}(\tau)\vec{a}(\tau) = \Lambda(\tau)\mathbf{N}(\tau) \tag{7.8}$$

where $\vec{a}(\tau)$ are the coefficients of the projected basis functions and $\Lambda(\tau)$ is the eigenvalue.

Again for the 1D electron gas, we choose the Feynman ansatz at the trial state for each given momentum,[95] i.e. $\rho(k)|\Psi_0\rangle\ \forall k$ for the charge excitations and $\sigma(k)|\Psi_0\rangle\ \forall k$ for the spin excitations, where $\sigma(k) = \sum_j \sum_\sigma \sigma e^{ikr_j^\sigma}$ is the Fourier transform of the spin density. In the following we, work with the charge excitations, but the same applies for $\sigma(k)$. Since the basis set is orthogonal, the method in Ref. [89] is greatly simplified as every k component is decoupled. For each k we have to calculate

$$\frac{\langle \Psi_0|\, \hat{\rho}(k,\tau)\hat{H}\hat{\rho}(-k,0)\, |\Psi_0\rangle}{\langle \Psi_0|\, \hat{\rho}(k,\tau)\hat{\rho}(-k,0)\, |\Psi_0\rangle} = \frac{\sum_i \epsilon_k^i A_k^i e^{-\tau(\epsilon_k^i - E_0)}}{\sum_i A_k^i e^{-\tau(\epsilon_k^i - E_0)}}, \tag{7.9}$$

where $\hat{\rho}(k,\tau)$ is written in the Heisenberg representation with imaginary time evolution, $|\Psi_k^i\rangle$ is the i'th excited state with momentum k, ϵ_k^i is its energy, $A_k^i \equiv |\langle \Psi_k^i|\rho(-k)|\Psi_0\rangle|^2$ is the spectral weight of the eigenvalue expansion, and E_0 is the ground state energy. For large τ the ratio in the above equation will converge to the lowest energy ϵ_k^0 of a given k, provided A_k^0 is non zero. Another limitation is given by the exponentially small denominator, which will exponentially increase the statistical noise of the estimate as the projection time increases. Both the numerator and denominator in Eq. 7.9 are evaluated by means of the forward walking[67, 62] procedure based on the DMC or LRDMC sampling. Indeed, for large enough τ the left hand side of Eq. 7.9 can be rewritten as

$$\frac{\int \mathrm{d}\mathbf{R}\,\mathrm{d}\mathbf{R}'\ \rho(-k)G(\mathbf{R},\mathbf{R}',\tau)E_L(k,\mathbf{R}')\rho(k)P(\mathbf{R}')}{\int \mathrm{d}\mathbf{R}\,\mathrm{d}\mathbf{R}'\ \rho(-k)G(\mathbf{R},\mathbf{R}',\tau)\rho(k)P(\mathbf{R}')}, \tag{7.10}$$

where $E_L(k,\mathbf{R}) = \frac{H\rho(k)\Psi_T(\mathbf{R})}{\rho(k)\Psi_T(\mathbf{R})}$ is the local energy of $\rho(k)|\Psi_T\rangle$,

$$P(\mathbf{R}) = \Psi_T(\mathbf{R})\Psi_0(\mathbf{R}) \tag{7.11}$$

is the QMC mixed distribution, and

$$G(\mathbf{R},\mathbf{R}',\tau) = \Psi_T(\mathbf{R})\langle\mathbf{R}|e^{-\tau H}|\mathbf{R}'\rangle/\Psi_T(\mathbf{R}') \tag{7.12}$$

is the importance sampled Green's function.

7.4 Finite Size Errors

In contrast to the ground state case where the finite size errors are quite significant, the finite size effects in these excited state calculations tend to be rather small. The reason for this is that the excited state energies are calculated as a difference of energies of the excited and ground states of the system with the same number of electrons. For this reason the finite size errors in the energy cancel to a large degree. In fact one large contribution to the finite size errors of the ground state calculation, the single body kinetic terms, cancel exactly.

Additionally, the collective nature of the excitations and the use of the Feynman ansatz[95] to describe them also contributes to the relatively small finite size bias. The plasmons (and spin waves) are delocalized throughout the electron gas and thus the interaction of the plasmon with its periodic images is desirable. Furthermore, the plasmon at each momentum is commensurate with the cell and thus the finite size cell should not distort this excited state to a large degree. This is in marked contrast to excitations in semiconductors and insulators where the excitons are bound and localized in the sample. In that case, the interactions with the periodic images of the exciton cause a finite size bias and for supercells that are too small, and the exciton may not fit inside the cell and be distorted, causing further finite size effects [91].

In order to test the cancellation of the finite size errors in the momentum resolved charge excitation spectrum, the spectrum is calculated with very large datasets for $b = 0.1$, $r_s = 3.5$ and $N = 10, 14, 18$ and 22. The results of these calculations are presented in Fig. 7.1, which shows a very good agreement of the excitation energies calculated with different cell sizes.

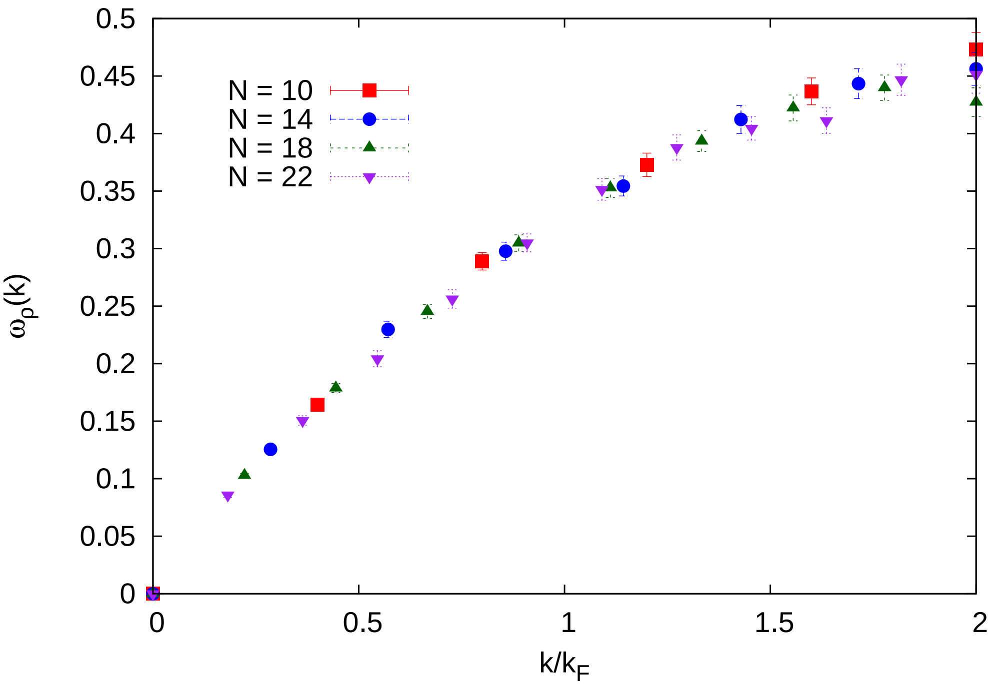

Figure 7.1: Charge excitation energy vs number of electrons in the simulation cell. $b = 0.1$ and $r_s = 3.5$. The different numbers of electrons preclude calculation of the energy at the same momenta, however the underlying spectrum is remarkably consistent for the different system sizes.

7.5 Comparison of Methods

There is one more consideration to be taken into account when calculating the excitations using forward walking. This is the lattice discretization error that is inherent in the LRDMC method. This lattice discretization error causes an approximation to the propagator. This can be contrasted with the Trotter error present in the short time propagator of a DMC calculation. In LRDMC, the kinetic energy term is given a shift ν to correct for the lattice discretization error when calculating the ground state energy (Eq. 4.23). This correction works well in ground state and CFMC calculations, however the propagator remains approximate and thus the transient estimate method which relies on the exact imaginary time dependence of the simulation is biased.

This bias is most evident at high densities where the kinetic energy is the dominant term in the total energy. Fig. 7.2 shows the errors in the excitations computed for $b = 1, r_s = 0.2$ using both DMC and LRDMC with the transient estimate method. The time-step for the DMC calculation is taken to have the same diffusion constant as the LRDMC calculation with $a = 1.1$. The unbiased value is determined using either the TE method with DMC or the CFMC method with the largest lattice spacing. The figure clearly shows that a rather large error is made for the excitation energies obtained within the TE method where the underlying propagation is LRDMC with a large time-step. This error is subsequently reduced as the lattice spacing is decreased.

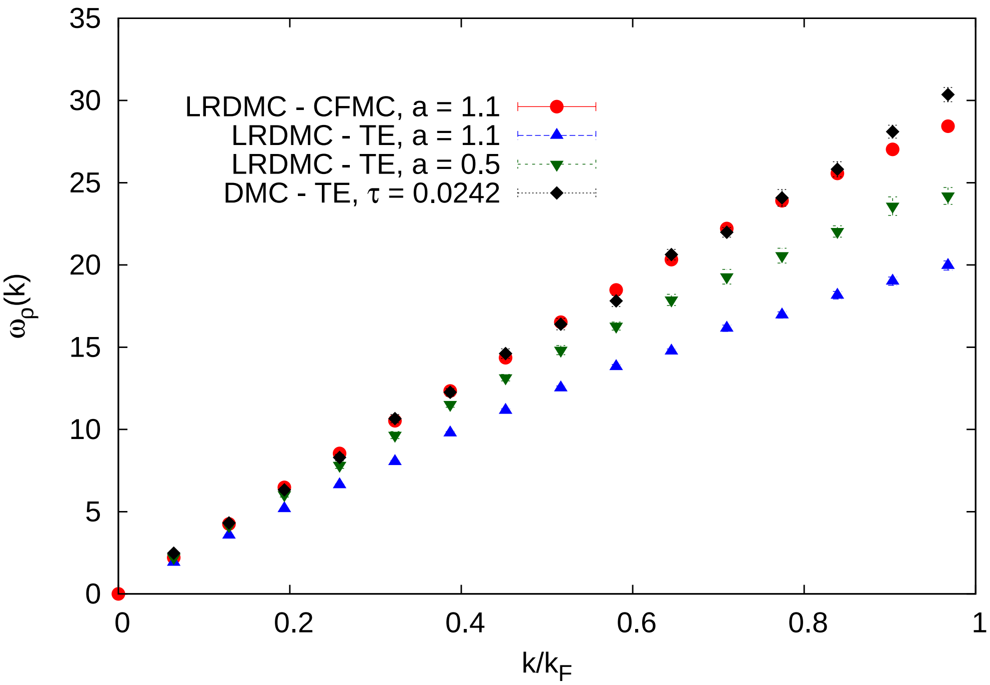

Figure 7.2: Charge excitation energy for $b = 1, r_s = 0.2$ calculated using the TE method with two different LRDMC lattice spacings and a DMC time-step yielding the same diffusion constant as a lattice spacing of 1.1. The energies are all converged as a function of imaginary time for $k/k_F < 0.5$. The results for the largest LRDMC lattice space are shown using the CFMC method for comparison, both this calculation and the DMC based TE calculation are converged with respect to the time-step or lattice size.

Chapter 8

Momentum Resolved Excitation Energies

In this chapter we will present results for the full momentum resolved charge and spin excitation spectrum for the unscreened wire as a function of density. These are the only excitations possible that conserve the continuous translational symmetry of the system. Numerically the sign problem makes it very difficult to calculate the lowest excited state energies for large momenta and for large numbers of electrons. However, it is possible to observe several properties of the electron gas using the results that we have been able to obtain.

8.1 Charge Excitations

Theory can provide some insights into the nature of the momentum resolved charge excitation energy of the 1D electron gas. Consider first a non-interacting system of electrons, which is sufficient at high density, since the kinetic terms become much larger than the interaction terms. For momentum $k < 2k_F$, where $k_F = \frac{\pi}{4r_s}$ is the Fermi momentum of the unpolarized electron gas, the lowest energy single particle excitation is a particle hole excitation where an electron with momentum $k_F - k$ is promoted to momentum k_F with a change of energy

$$\omega_\rho(k) = k_F k - \frac{k^2}{2}, \;\; k \leq 2k_F \tag{8.1}$$

For an infinite system the excitation energy vanishes at $k = 2k_F$; however, for a finite size cell with N electrons the values of the momentum k are discrete and are spaced by $\delta k = \frac{\pi}{Nr_s}$. Thus in the lowest particle hole excitation the electrons are promoted to the single particle state with momentum $k_F + \delta/2$

which is the lowest allowed unoccupied state. This changes Eq. 8.1 to

$$\omega_\rho(k) = (k_F + \frac{\delta}{2})k - \frac{k^2}{2}, \;\; k \leq 2k_F. \tag{8.2}$$

Therefore the minimum energy excitation for promoting an electron from a filled to an empty state is $\omega_\rho(2k_F) = \pi^2/2Nr_s$. This may also be viewed in a different way by noting that the minimum energy excitation for $k = 2k_F$ corresponds to simply shifting the momentum of each of the occupied states by $\delta k = \frac{\pi}{Nr_s}$ so that the energy change is the same as a change of the center of mass momentum by δk and a change of $\delta E = \pi^2/2Nr_s$ in agreement with the result above.

The arguments are actually much more general. The fact that change in energy is simply the center of mass kinetic energy is a consequence of Galilean invariance which requires that all other terms in the energy of the system do not change if it is viewed from a moving reference frame. Thus for an interacting system the relative positions and velocities of the particles do not change when viewed from a moving reference frame (in a non-relativistic system). Thus the conclusions apply to the interacting system as well: in all cases the excitation energy at $2k_F$ vanishes except for finite size effects.

The Galilean invariance also allows the energy of the modes with momentum $2nk_F$ where n is an integer to be determined in the interacting system. For these modes the trial wave function can be rewritten to have an overall phase factor $\exp\left\{i\frac{\pi}{Nr_s}\sum_i^N r_i\right\}$. This phase factor can be eliminated using the fixed phase approximation[97]. which allows the exact energy to be determined in 1D as does the fixed node approximation. This leaves the problem unchanged and the energy trivially equal to the ground state energy of the system up to a finite size correction of order $1/N$. The energy of these $k = 2nk_F$ excitations may be calculated using the forward walking technique and the Feynman ansatz trial wavefunction as before. However, as this is a poor wavefunction for this state a much easier approach is to use the ground state wavefunction multiplied by the phase factor above as the trial. The energy of these excitations as a function of imaginary time is plotted for both $2k_F$ and $4k_F$ at $_rs = 1, 2$ and 4 in Fig. 8.1. The data shows especially for $r_s = 1$ that convergence is difficult to achieve using the Feynman ansatz for the excitations. The line indicates the theoretically predicted gap for the finite size system at the given momentum. The values of these theoretical estimates have been checked using the trial wavefunction mentioned earlier in this paragraph.

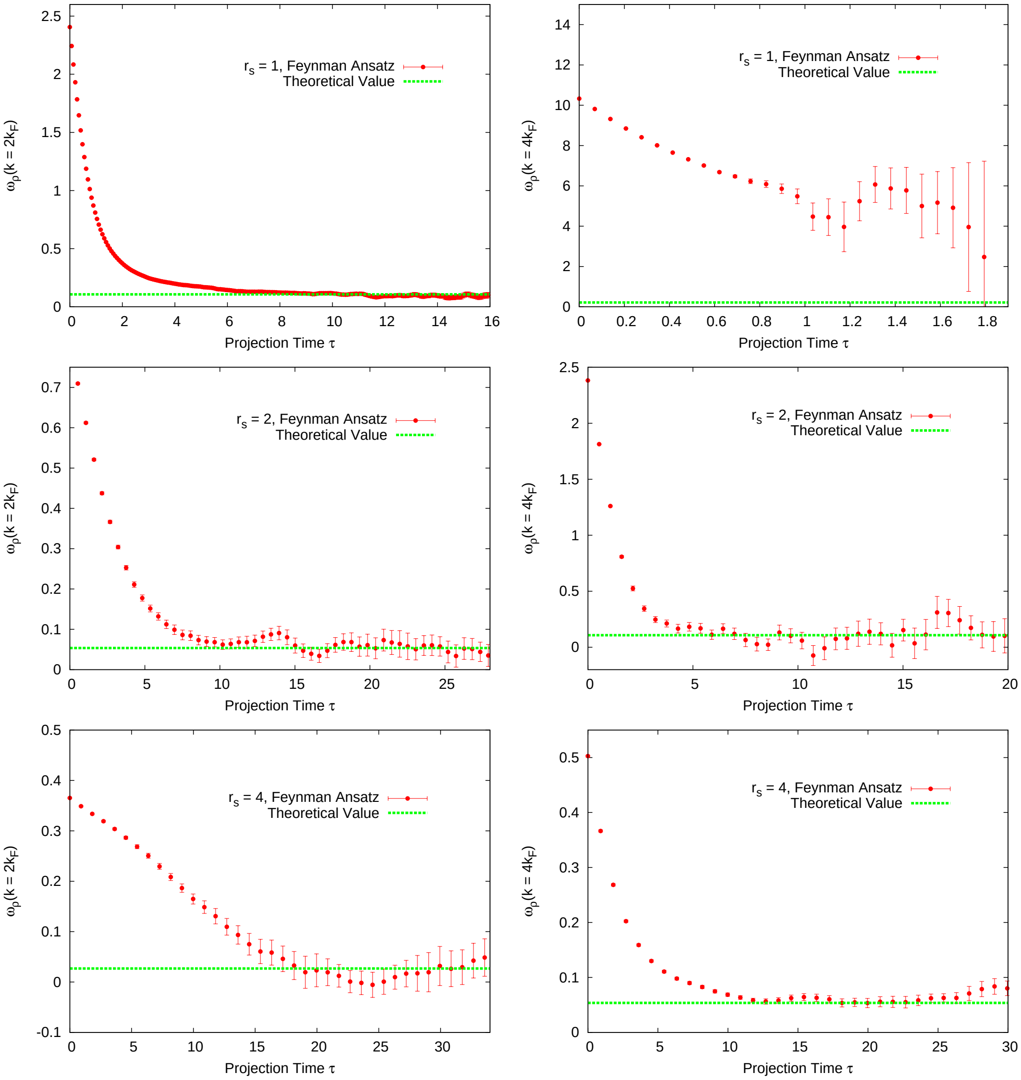

Figure 8.1: Charge excitation energy as a function of projection time for $b = 1$ and $r_s = 1, 2$ and 4. All calculations were performed with 46 electrons. The left column shows the convergence of the Feynman ansatz wavefunction in CFMC for $k = 2k_F$ where the converged energy is $\pi^2/(2Nr_s)$. The right column shows the same for $k = 4k_F$ where the converged energy is $\pi^2/(Nr_s)$.

Calculations of the full momentum resolved excitation spectrum have also been carried out for several values of the density. While the converged limit of these calculations is known, the approach to the limit has interest as well. This approach can in principle be used to study how the spectral function of the excitations for a given k changes as a function of the density of the system where the spectral function is defined as

$$A(k,\omega) = \sum_i \delta(\epsilon_k^i - \omega) \left\langle \Psi_k^i \right| \rho(k) \left| \Psi_0 \right\rangle \tag{8.3}$$

where $|\Psi_k^i\rangle$ is the $i'th$ excited state of the electron gas with momentum k and energy ϵ_k^i. As the forward walking projects this state in imaginary time for densities where the lower lying excited states have a larger overlap with the Feynman ansatz, the energy will converge more rapidly. Conversely, the energy will converge more slowly if the overlap with the low lying excited states is smaller. This situation is shown in Fig. 8.2. The calculations at $r_s = 1, 2$ and 6 are performed with a modest amount of data using the Feynman ansatz trial wavefunction and CFMC. In all cases the excited state energy at $k = 2k_F$ and $k = 4k_F$ should be nearly zero apart from $1/N$ terms. Instead the $4k_F$ mode has not converged for $r_s = 1$ and the $2k_F$ mode has not converged for $r_s = 6$. This can be attributed to the presence of the quasi Wigner crystal order at lower densities which makes the $4k_F$ density wave more accessible an excitation.

By changing the polarization of the electron gas from $\zeta = 0$ to $\zeta = 0.5$ it is possible to observe the physics behind the different soft modes. The charge excitation spectrum for $r_s = 2$ and $\zeta = 0, 0.5$ is shown in Fig. 8.3. The soft mode at $2k_F$ splits into two soft modes at k_F and $3k_F$ (where k_F is defined relative to the unpolarized gas). However, the $2k_F$ mode should still be gapless even for the $\zeta = 0.5$ system because of the continuous translational symmetry of the system. The splitting of the soft mode is explained by noting that those excitations are formed by moving an electron from one edge of the Fermi surface to the other. Whenever the polarization is changed, the Fermi surface splits into two nested surfaces: one for the up and one for the down electrons. The gapless excitation at $4k_F$ is unchanged by the change in polarization which is consistent with the interpretation that this is the excitation with the periodicity of the mean interparticle spacing and does not depend on the spin of the electrons.

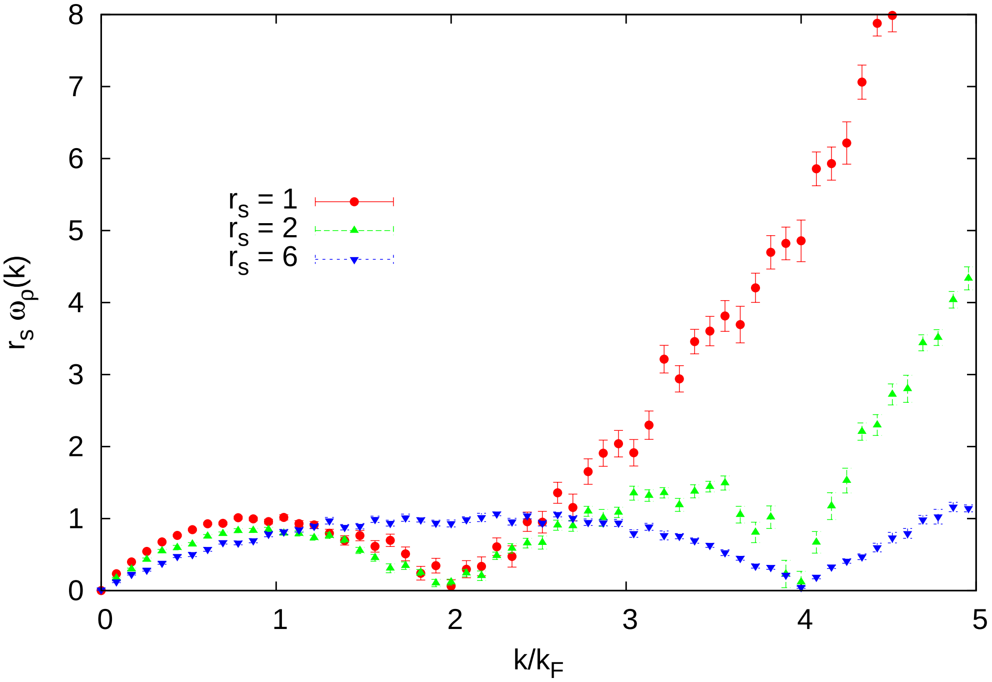

Figure 8.2: Charge excitation energy as a function of k for $b = 1$ and $r_s = 1, 2$ and 6. All calculations were performed with 46 electrons. This graph shows the a faster convergence of the $2k_F$ mode for higher densities and a faster convergence for the $4k_F$ mode at lower densities.

8.2 Spin Excitations

The spin excitation spectrum is more difficult to compute because at low density sampling the spin degrees of freedom becomes difficult due to the pseudo nodes. It is possible at high to moderate densities to compute the spin excitation spectrum and again there are a few theoretical predictions available to explain the behavior of the excitation spectrum. The Luttinger liquid theory with long range interactions predicts that the spin excitation spectrum at low energy will be linear. The LL theory predicts the excitation spectrum will be linear near $k = 0$[10]. Also again as for the charge excitations, the energy gap for excitations with momentum $2nk_F$ should be zero. Finally the limit of the low density excitations is known exactly because of the mapping from the spin degrees of freedom to the Heisenberg spin chain where the excitation spectrum is now

$$\omega_\sigma(q) = \pi J r_s \left| q \right|, \tag{8.4}$$

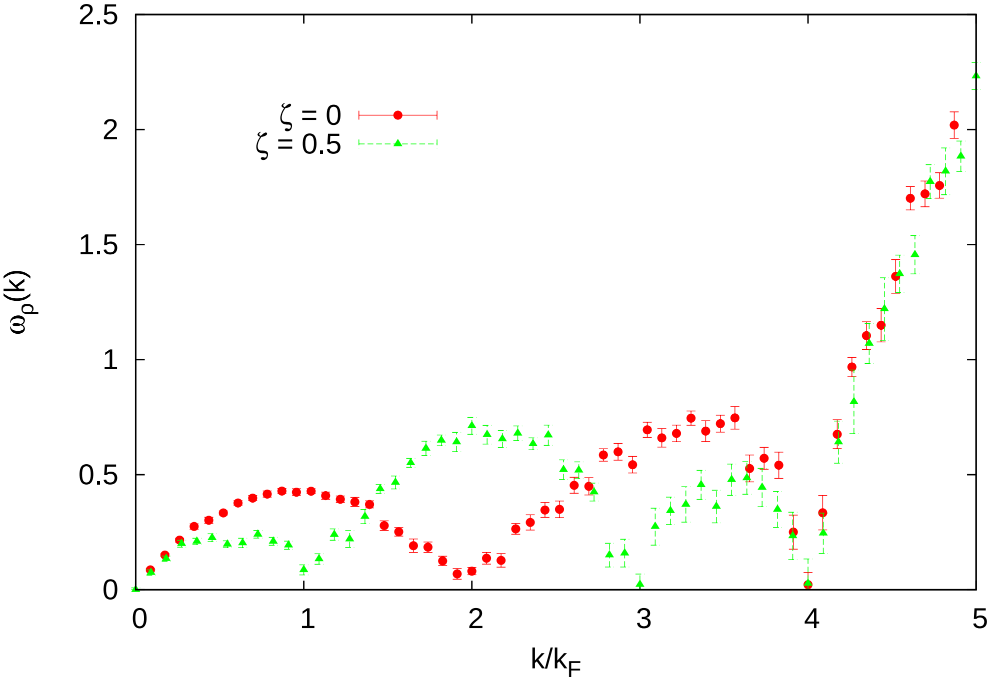

Figure 8.3: Charge excitation energy as a function of k for $b = 1$ and $r_s = 2$ with $\zeta = 0$ and $\zeta = 0.5$ The gapless excitation mode at $2k_F$ for the unpolarized system splits into two modes for the $\zeta = 0.5$ electron gas.

where J is the coupling constant in the effective Heisenberg Hamiltonian[80]

$$\hat{H}_\sigma = \sum_i J\hat{S}_l \cdot \hat{S}_{l+1}. \tag{8.5}$$

The full spin spectrum for $b = 1$, $r_s = 1$ is shown in Fig. 8.4. It exhibits the small gap at $q = 2k_F$ as well as a roughly linear dispersion at small q. Further details concerning the behavior of the long wavelength portion of this spectrum will be discussed in chapter 9.

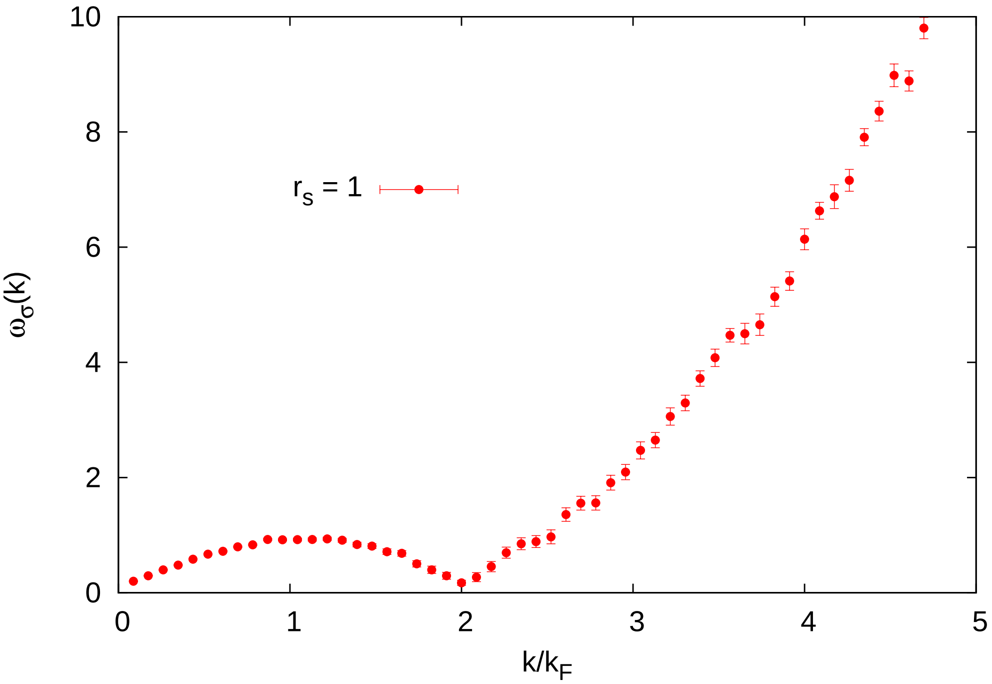

Figure 8.4: Spin excitation energy as a function of k for $b = 1$ and $r_s = 1$ obtained using the CFMC method. At this high density convergence is easy to obtain for the mode at $2k_F$. The spectrum is nearly linear for $k/k_F < 0.5$

Chapter 9

Long Wavelength Charge and Spin Excitations

The convergence of the excitation energies with propagation time may be difficult to obtain for a general k with the methods presented in chapter 7. However, for long wavelength excitations $\rho(k)\,|\Psi_0\rangle$ is a good approximation to the lowest excited state wave function with momentum k and the energies can be determined easily with a short projection time τ. Using sum rules, it is possible to derive a relation between the excitation spectrum at short range and the charge compressibility and spin susceptibility[98]. This chapter will explore the charge compressibility and spin susceptibility of the quasi one dimensional electron gas.

9.1 Charge Compressibility

Using sum rules it is possible to relate the spectrum of the long wavelength charge excitations to the charge compressibility, χ, [75, 99] yielding

$$\omega_\rho(k \to 0) = v_F|k|\sqrt{\rho_F V(k \to 0) + \frac{\chi_0}{\chi_\rho}}, \tag{9.1}$$

where $\omega_\rho(k)$ is the energy of the lowest charge excitation with momentum k, ρ_F is the density of states of the free electron gas at the Fermi energy, and $\chi_0 = 16r_s^3/\pi^2$ is its compressibility.

The form χ_0/χ_ρ is a particularly useful choice because it is related to the capacitance of the electron gas per unit length

$$\frac{1}{C} = \frac{1}{e^2}\frac{\partial\mu}{\partial N} = \frac{1}{e^2\rho_F}\frac{\chi_0}{\chi_\rho}, \tag{9.2}$$

where C is the capacitance per unit length and μ is the chemical potential[100, 101, 102]. This form is also useful in that it isolates the role of exchange and correlation in the compressibility from the noninteracting compressibility which is dominant at high densities.

We fit the charge excitation spectrum using this form for several densities and plot the results in Fig. 5.

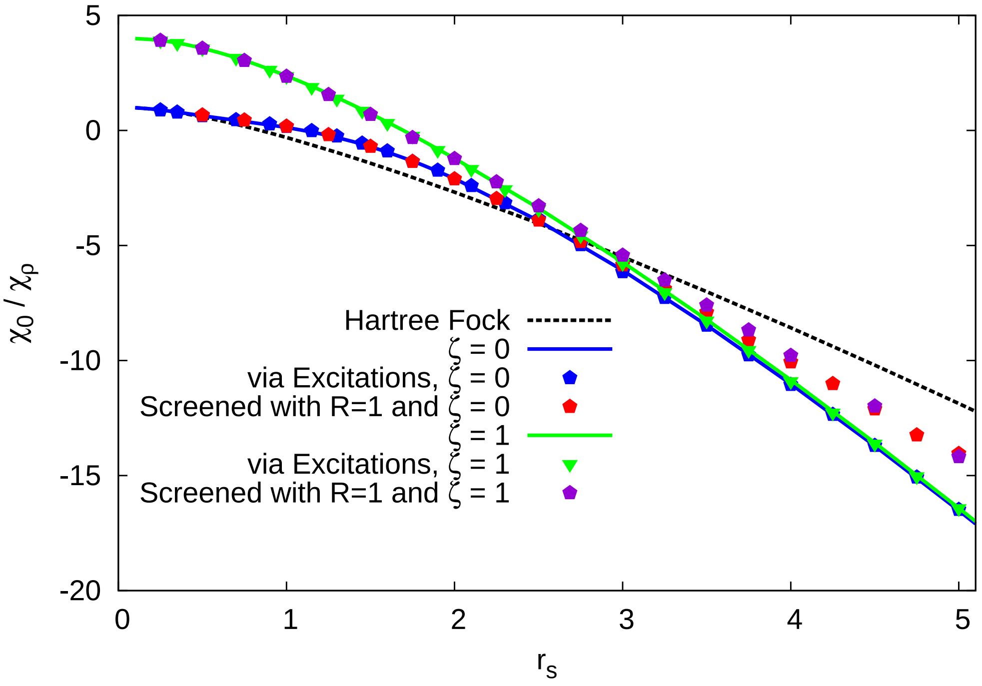

Figure 9.1: Inverse charge compressibility χ_0/χ_ρ of the unpolarized and fully polarized wire for $b = 0.1$, with both an interaction screened by a metallic plane as defined in section 3.3 ($R = 1$) and an unscreened interaction. Also the HF (dashed back line) charge compressibility is reported for the unpolarized wire. The solid lines are obtained from the second derivative of the energy parametrization explained in chapter 5, while the points are evaluated through the charge excitations.

As can be seen in Fig. 9.1, the charge compressibility is becoming *negative* as the density decreases. This phenomenon has been previously observed in calculations on carbon nanotubes using density functional theory (DFT)[103]. In that case they argue that that a small diameter nanotube can in fact over-screen an applied electric field. In our case, the negative capacitance is due to the compressibility of the background charge in the Jellium model which is neglected in the present formulation.

The knowledge of χ_ρ can shed more light on the properties of the electron gas a function of the density. By looking at the charge compressibility (Fig. 9.1) it is apparent that the role of the electron correlation is becoming increasingly important around $r_s = 0.75$ for $b = 0.1$, where there is significant discrepancy between the Hartree-Fock (HF) and QMC values of χ_ρ. In particular, the correlation makes the system *softer* than the HF. At even lower densities the charge compressibility of the unpolarized system is approaching that of a fully polarized (or spinless fermion) gas. The difference between the two is going exponentially to zero, and they almost overlap for $r_s > 4$ (with $b = 0.1$). This means that the energy of the spin excitations is getting smaller and smaller as the density decreases.

9.2 Spin Susceptibility

The exponentially small difference between the compressibility for the polarized and unpolarized electron gas may be better understood by considering the spin susceptibility χ_0/χ_σ of the one dimensional electron gas. Sum rules may also be used to relate the long wavelength spin excitation energies to the spin susceptibility as was done in the case of the charge compressibility. In this case the relation is:

$$\omega_\sigma(k \to 0) = v_F|k|\sqrt{\frac{\chi_0}{\chi_\sigma}}, \tag{9.3}$$

where $\chi_0 = \pi^2/16r_s^3$ is the spin susceptibility of the noninteracting electron gas.

This value becomes exponentially small at low densities, where it is difficult to get a statistically accurate QMC estimate, since the sampling of the spin is "frozen" by the presence of quasi nodes (pseudo nodes) between unlike spin electrons [43]. The strong interaction makes the electrons repel each other at short-range, and the corresponding wave function is very small at the coalescence points of electrons with opposite spin. Consequently the spin flip rate in the QMC sampling becomes small and the efficiency decreases. However, the charge properties do not seem to be affected by this slowing-down. The physical reason for the quasi nodes will become even more apparent in Sec. 9.3, when we will discuss the Tonks Girardeau physics of the screened wire. To determine the spin susceptibility in this density regime, it is useful to use the WKB approximation for determining the dynamical properties of the electron gas.

9.2.1 Spin Susceptibility via WKB

Following the example of Matveev[81] we use the WKB approximation to determine the rate at which two electrons exchange by calculating the energy barrier that they must overcome. Although fluctuations prevent the formation of a Wigner crystal, the equilibrium positions of the electrons are assumed to be equally spaced with periodicity $2r_s$. Central to the accuracy of this approximation is the fact that at low densities the tunneling is dominated by the effect of the potential and the statistics can be ignored. Furthermore, all electrons are treated as uncorrelated except for a single pair which is allowed to exchange. In contrast to Matveev's approach we assume that the other electrons are distributed about their equilibrium positions according to the harmonic approximation with a Gaussian spread instead of being fixed delta function point particles. Taking the initial positions of the two exchanging electrons to be at $x = 0$ and $x = 2r_s$, they feel a static potential given by

$$V_{WKB}(x) = \sum_{n \neq 0,1} \int_{-\infty}^{\infty} \rho(y) V(x - 2nr_s + y) dy, \tag{9.4}$$

where $\rho(y) = \sqrt{\alpha/\pi}\exp(-\alpha y^2)$ is the equilibrium charge density of the non exchanging electrons and $V(x)$ is the interparticle potential. The harmonic approximation gives $\alpha = \sqrt{m\frac{\partial^2 W(x)}{\partial x^2}}$, where $W(x)$ is the potential at a given lattice site due to an infinite array of electrons spaced as $2r_s$.

The WKB approximation provides a means of calculating the the energy barrier that the two exchanging electrons must overcome. Choosing the center of mass for the two exchanging electrons be at $x = r_s$ (which is half way between the equilibrium positions of the two electrons), and also switching to reduced coordinates where r is the distance between the two exchanging electrons, the total potential energy is:

$$V_{tunnel}(r) = V(r) - 2\int_{-\infty}^{\infty} \rho(y) \left[V(r_s - \frac{r}{2} - y) - \sum_{n=-\infty}^{\infty} V(r_s - \frac{r}{2} - 2nr_s - y) \right] dy \tag{9.5}$$

The problem is now reduced to determining the rate at which the reduced particle tunnels from the well with $r > 0$ to the well with $r < 0$.

We will now follow the standard solution for the tunneling rate of a particle through the barrier in a double well potential. This derivation is presented in numerous quantum mechanics texts, with this discussion following Griffiths [104]. The WKB approximation assumes that the potential is slowly varying on the scale of $\hbar$ (making it a better approximation when r_s is large in this case). Making the definition $p(r) \equiv \sqrt{2m(E - V(r))}$ it is possible to approximate the wave function in the region where the energy of the particle $E > V(r)$:

$$\Psi(r) \approx \frac{C}{\sqrt{p(r)}}\, e^{\pm i p(r) r}. \tag{9.6}$$

Similarly the wave function in the region where $E < V(r)$ can be approximated as

$$\Psi(r) \approx \frac{C}{\sqrt{\kappa(r)}}\, e^{\pm \kappa(r) r}, \tag{9.7}$$

where $\kappa \equiv \sqrt{2m(V(r) - E)}$.

Strictly speaking the WKB approximation is not valid at the classical turning point, but it is possible to connect these wave functions at this point via several different methods. The method presented in Griffiths is to linearize the potential around the turning point and then to use the exact solution to Schrödinger's equation in terms of Airy functions. These solutions can be used to provide connection conditions for the wavefunction in the classically allowed and forbidden regions (Eqns. 9.6 and 9.7).

To construct a wave function for this tunneling potential using the WKB approximation, note that the wave function must be exponentially decaying as r increases in region III and be continuous at the boundaries between the regions I, II, and III. This wavefunction will have the form:

$$\psi(r) = \begin{cases} \frac{C}{\sqrt{\kappa(r)}} \left[2\cos\theta\, e^{\frac{1}{\hbar}\int_r^{r_1} \kappa(r')dr'} + \sin\theta\, e^{-\frac{1}{\hbar}\int_r^{r_1} \kappa(r')dr'} \right] & r \in I \\ \frac{2C}{\sqrt{p(r)}} \sin\left[\frac{1}{\hbar}\int_r^{r_1} p(r')dr' + \frac{\pi}{4} \right] & r \in II \\ \frac{C}{\sqrt{\kappa(r)}} e^{-\frac{1}{\hbar}\int_{r_2}^{r} \kappa(r')dr'} & r \in III \end{cases} \tag{9.8}$$

where $\theta(E) \equiv \frac{1}{\hbar}\int_{r_1}^{r_2} p(r')dr'$ and $r = r_1$ at the boundary between regions I and II and $r = r_2$ at the boundary between regions II and III. The two lowest energy states will be the even and odd wave functions above with the fewest nodes. The necessary condition for the wave function to be odd in this case is that $\psi(r = 0) = 0$, leading to the relation $\tan\theta(E) = -2e^{\phi(E)}$, where

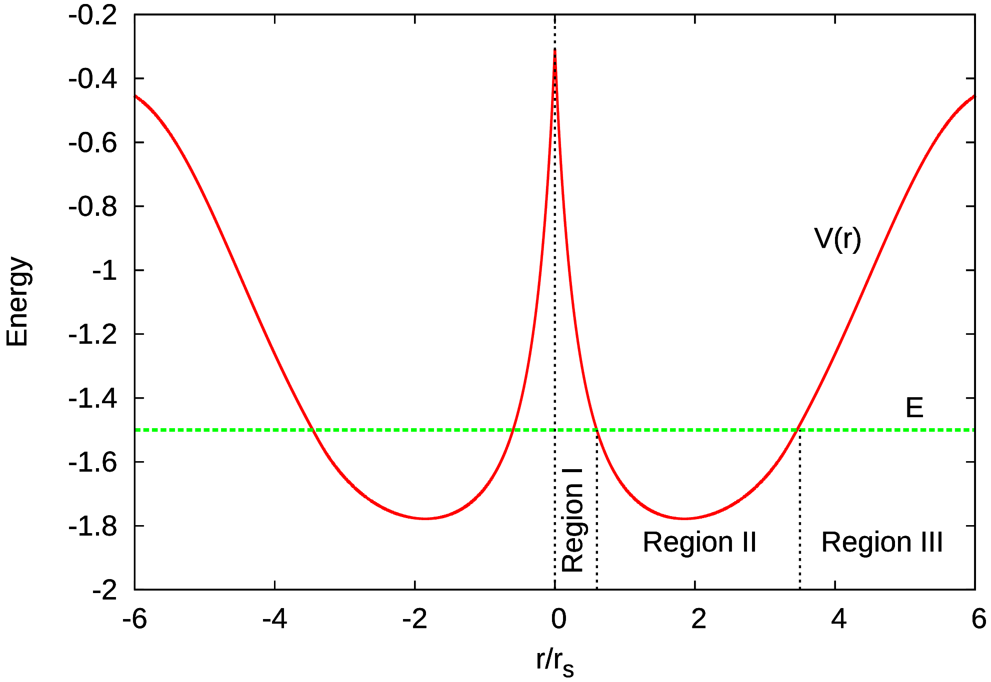

Figure 9.2: Tunneling potential for center of mass in WKB calculation. Equilibrium positions are at $2k_F$ and $-2k_F$. The right hand side is separated into three regions for a given trial energy E. There are two classically forbidden regions (I and III), and one classically allowed region (II).

$\phi(E) \equiv \frac{1}{\hbar}\int_0^{r_1}\kappa(r')dr'$. Likewise for even solutions, the wave function must have a zero derivative at $r = 0$ leading to the relation $\tan\theta(E) = 2e^{\phi(E)}$. Assuming the the wavefunctions for the lowest even and odd states are very similar in region II apart from a sign (a good approximation if the value of the potential in region I is large compared to E), it is possible to construct a wavefunction that (up to a choice of phase) is almost entirely in either the right or left wells:

$$\Psi_{\text{right,left}} = \frac{1}{\sqrt{2}}(\Psi_{\text{even}} \pm \Psi_{\text{odd}}) \tag{9.9}$$

where $+$ is for the right well and $-$ is for the left well. The energy barrier separating these two states is then just $E_{\text{odd}} - E_{\text{even}}$, which is the energy barrier for two electrons to exchange within the WKB approximation.

At low densities the electrons behave as a spin chain obeying the Heisenberg Hamiltonian where the spin flips are mediated by an exchange of nearest neighbor electrons, so the spin susceptibility can be determined from the energy barrier computed within the WKB approximation by analogy with the

Heisenberg Hamiltonian in 1D as shown by Matveev [81]. The spin velocity of the equivalent Heisenberg spin chain can be found from the Bethe ansatz solution[105, 106], yielding $v_\sigma = \pi J r_s$ where J is the size of the energy barrier in the WKB approximation. This gives the susceptibility through Eq. 9.3.

Where the density is large enough that QMC reliably samples the spin exchanges Fig. 9.3 shows the spin susceptibility computed using the forward walking techniques agrees well with the WKB estimate only after the smearing of the electron sites given by the harmonic approximation. It is therefore important to use the potential in Eq. 9.4 to have an accurate estimate of the exchange at intermediate densities. This agreement and the fact that the dynamical many-body corrections to the WKB estimate are very small at low density[107] justify the use of WKB for dilute systems where it is difficult to extract information from the QMC calculations. In addition, the exponential decay of v_σ as a function of $\sqrt{r_s}$ obtained in this way is in agreement with previous results [81, 108, 109] for potentials where they can be compared.

9.3 Tonks Girardeau Gas and Fogler Prediction

Fig. 9.3 summarizes our findings for the unscreened wire. The liquid-to-quasi-crystal crossover is shifted to higher densities for thinner wires, while the spin susceptibility is always significantly different from zero in the crossover region for the values of the confinement taken into account. The smallest b we studied ($b = 0.0001$) corresponds to one of the thinnest confinements realized experimentally [110, 111]. The spin exchange is still sizable in the crossover region due to the not-so-long localization length of the electrons and not-so-thin width of the wire.

Fogler predicted the existence of a so called Coulomb Tonks behavior where the electrons behave as spinless fermions what still feel the normal coulomb repulsion. Our study does not therefore find any signature of the Coulomb-Tonks gas phase in between the liquid and quasi Wigner crystal, which was claimed by Fogler for ultrathin wires [31]. However, the structure factor plotted in Fig. 6.3 reveals the tendency for electrons to approach the noninteracting spinless fermion behavior as the wire width decreases. The fundamental difference with respect to the noninteracting spinless picture is

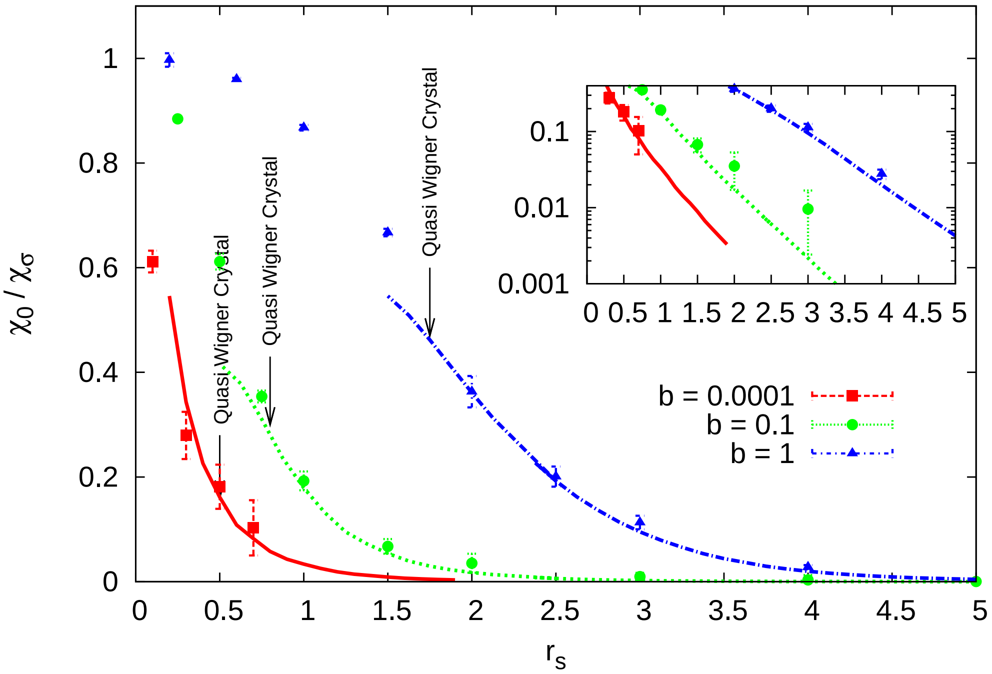

Figure 9.3: Inverse spin susceptibility χ_0/χ_σ for different thicknesses. The dependence on r_s is shown. The points are the QMC calculations, while the lines are the WKB estimates. The arrows indicate the liquid-to-quasi-Wigner-crystal crossover determined by the appearance of a $4k_F$ peak in the structure factor. This crossover happens between $r_s = 0.4$ and 0.8 for $b = 0.0001$, between $r_s = 0.6$ and 1.0 for $b = 0.1$ and between $r_s = 1.5$ and 2 for $b = 1$.

the pronounced peak at $4k_F$, which characterizes the Coulomb long-range interactions at low density.

The low density limit with screened interactions is particularly interesting as the screening introduces a new feature. At low densities the electron-electron repulsion at short range makes exchanges between electrons virtually impossible, corresponding to the limit $U \to \infty$. As a result for the ultra-thin wire with strong screening ($b \ll 1$ and $r_s \gg 8R^2/\pi$), the mapping of the interaction to the potential in Eq. 6.7 becomes *exact*. In this situation not only do the electrons behave as spinless fermions, but the charge velocity approaches that of *noninteracting* spinless fermions ($v_\rho = 2v_F$). This is analogous to the case of bosons with infinite repulsive contact interactions, (or impenetrable particles) where the system can be mapped into a noninteracting Fermi gas [29]. The impenetrable Bose system is often called a

Tonks-Girardeau gas. In our case the situation is analogous, namely the fermions become impenetrable due to an effective infinite contact repulsion and so they behave as if they were noninteracting and spinless. We refer to this behavior as Tonks-Girardeau regime. One of its features is the presence of nodes in the wave function at the coalescence of unlike spin pairs. This is the extreme case when the pseudo nodes that complicate the ergodicity of Monte Carlo calculations at low density as discussed in Sec. 4.2 become actual nodes.

While this effect has been discussed in the literature [81, 31, 30], our work provides quantitative predictions for the onset of the noninteracting spinless behavior. Fig. 9.4 shows the charge velocity in the limit of low density for different values of the screening in the thinnest wire we studied ($b = 0.0001$). We found that in order for the Tonks-Girardeau behavior to manifest itself, the distance to the gate R must be less than 0.1 and the density must be lower than $r_s = 1$. For R larger than 0.1, at low density the charge velocity does not converge to the noninteracting spinless fermion limit ($2v_F$), but saturates at a larger value.

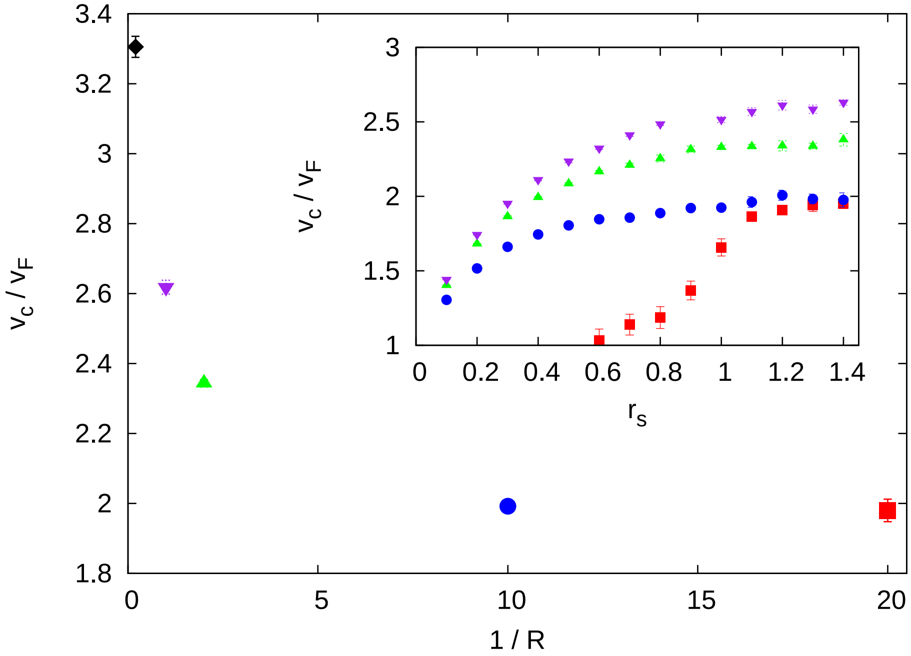

Figure 9.4: Asymptotic large r_s values of the charge velocity in units of v_F vs. inverse screening length for ultrathin wire ($b = 0.0001$) from $R = 0.05$ to $R = 5$. In the inset we report the full dependence of the charge velocities on r_s at different R.

It is possible to see the transition of the screened electron gas to the noninteracting spinless fermion behavior more directly by analyzing the static structure factor, as was done in the unscreened case. In Fig. 9.5, the $S(k)$ is plotted at different densities for the ultrathin wire with $b = 0.0001$ and gate located at $R = 0.1$ from the wire. Contrary to the case of the unscreened wire (Fig. 6.3 lower panel), at low densities the peak at $4k_F$ is absent and the structure factor approaches that for noninteracting spinless fermions quite closely. Notice that at the same time the charge velocity approaches the value of $2v_F$ (see Fig. 9.4).

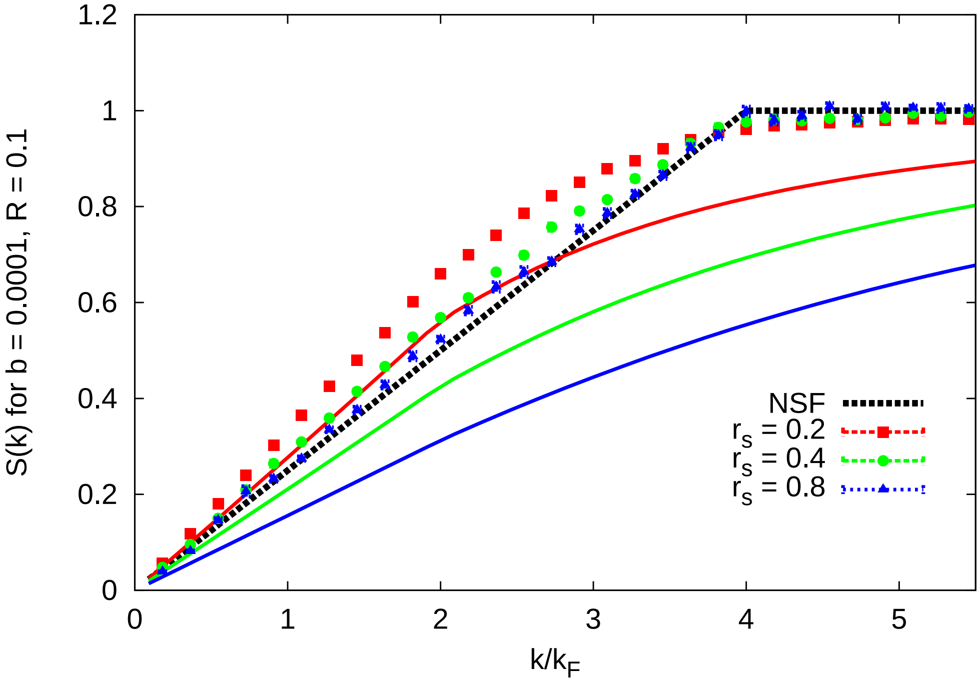

Figure 9.5: Static structure factor for the screened wire with $b = 0.0001$ and $R = 0.1$, plotted for three values of the density, $r_s = 0.2$,0.4 and 0.8. The solid lines correspond to the MSA prediction for each density, and the black line is the structure factor for noninteracting spinless fermions (NSF).

The same study was repeated for the wire with $b = 0.1$. Here the short-range behavior of the potential is much less repulsive than in the $b = 0.0001$ case and the same value R for the screening. The result of this is that the charge velocity does not converge to $2v_F$ even for a gate as close as $R = 0.1$, which equals the width of the wire and thus represents the geometric limit of validity for the uncorrelated inter-wire interaction. Therefore for $b = 0.1$ and thicker wires whose widths are realizable in semiconducting nanostructures, we did not find the Tonks-Girardeau behavior in our calculations.

Chapter 10

Experimental Observation of 1DEG via Momentum Resolved Tunneling

A recent series of experiments by Auslaender *e*t al. have pioneered a new technique for measuring the excitation spectrum of one dimensional semiconductor quantum wires [35, 36, 37, 38, 39, 40, 41]. This chapter will endeavor to present some of their most impressive results and will provide a backdrop against which the calculations of chapter 11 will be set.

10.1 Experimental Setup

The principal innovation that made the experiments by Auslaender *e*t al. possible was the realization that much more could be learned about the electron gas by creating a spatially extended tunnel junction rather than a quantum point contact. To this end they designed a device where two quasi one dimensional wires fabricated using the cleaved edge overgrowth technique are grown parallel to each other separated by a thin but highly insulating barrier. They were then able to measure the current of electrons flowing from one wire to the other through the barrier. This device is shown schematically in Fig. 10.1.

Tunneling an electron from one wire to the other leaves the system in an excited state. Energy is conserved in this process so in the experiment an electric field provides a bias favoring the tunneling. In this experiment a gate produces a bias voltage V, shifting the relative energy of the states in the two wires by eV. Additionally, the geometry of the sample preserves the translational symmetry along the wires and as a consequence the momentum of the electrons is conserved in the tunneling process. A magnetic field is also applied perpendicular to the plane of the wires. This has the effect of giving the electrons a momentum boost equal to $k_B = eBd/\hbar$ as they tunnel between the two wires where B is the strength of the magnetic field and d is the distance between the wires. This freedom allows precise control of the

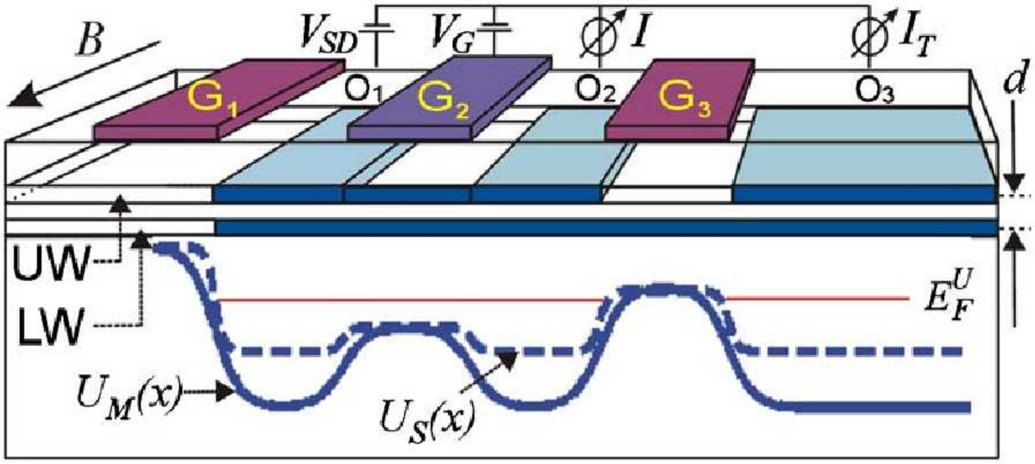

Figure 10.1: Schematic of device for momentum resolved tunneling of electrons. The device is shown with the cleaved edge parallel to the figure. The magnetic field B is perpendicular to the plane. Two quantum wires are shown a distance d apart with the upper wire (UW) being 20 nm thick and the lower wire (LW) 30 nm wide. Figure is reproduced from Steinberg *et al.* [41] .

momentum and the energy of the electrons tunneling between the two wires and thus provides a means to measure the excitation spectrum of the electron gas in a one dimensional quantum wire.

In order to understand this spectroscopy it is first useful to recall that although Luttinger Liquids do not have a discontinuity in occupation at the Fermi surface, they nevertheless do have a well defined Fermi surface. Given the existence of a Fermi surface it is possible to determine both the density in the wires and their excitation spectrum. Experimentally this is accomplished by varying the magnetic field with a constant bias. The tunneling current will initially be very small if the density of the electron gas in the wires is not equal. As the magnetic field is increased the tunneling current will remain small until it increases to a large value at

$$B_1 = \frac{|k_{F,u} - k_{F,l}|}{ed}, \tag{10.1}$$

where $k_{F,u}$ is the Fermi momentum in the upper wire. This corresponds to the point at which unoccupied states in the wire with the lower density become available for tunneling. As the magnetic field increases the tunneling current again becomes small as all of the states available for the tunneling become unoccupied. Finally when the magnetic field is equal to

$$B_2 = \frac{|k_{F,u} + k_{F,l}|}{ed} \tag{10.2}$$

the tunneling current again increases because the electrons traveling in opposite directions can tunnel between the two wires. Knowledge of these two values of the magnetic field, B_1 and B_2 allow the Fermi momentum in each wire to be determined and thus the density in each wire is known.

10.2 Spin Charge Separation

The potential of the momentum resolved tunneling experiments are in no way limited to determining the density in the wires. By scanning the bias voltage and the magnetic field, it is possible to map out the spectral functions of the interacting electrons in both wires. Graphically this is presented in a figure by Zülicke (Fig. 10.2) that shows how the spectral functions for two noninteracting one dimensional wires may be determined in this experiment [112].

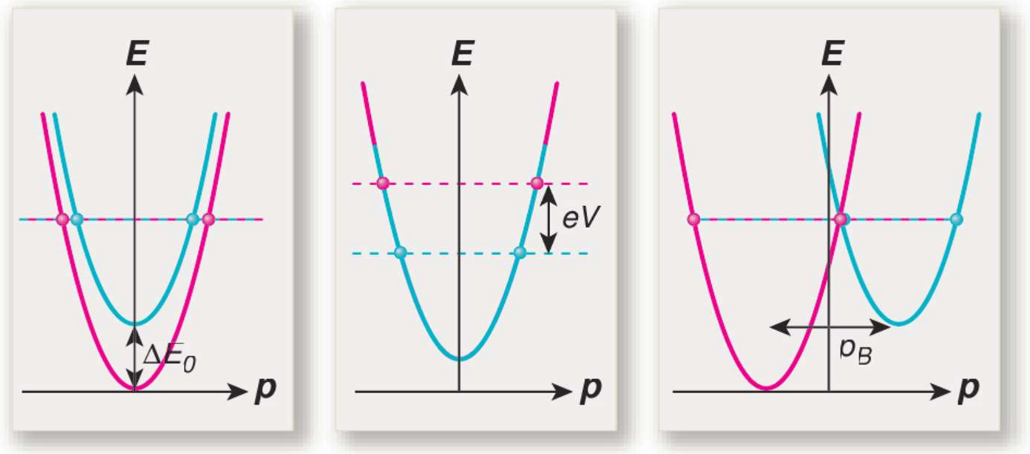

Figure 10.2: The figure on the left shows the noninteracting dispersion curves as a function of momentum for two wires. The Fermi energy for the wires are indicated by dashed horizontal lines which are coincident in this case. The center figure shows the effect of a finite voltage V that provides a relative shift of the curves. This situation would correspond to a large tunneling current between the two wires. Finally, the curve on the right shows the effect of an applied magnetic field B which shifts the curves relative to each other by momentum $p_B = eBd/\hbar$. This figure is due to Zülicke [112].

A more complete description of the tunneling between the wires is found by studying the properties of the single particle spectral functions in the quantum wires. There are two possible behaviors for the spectral function in the quantum wires. They may have the characteristics of a Fermi liquid, exhibiting a delta function peak in the spectral function corresponding to a quasiparticle state. On the other hand if the wires are successful realizations of Luttinger Liquids, they will instead have singularities in the spectral function $A(k, E)$ at $E = v_\sigma q$ and $E = v_\rho q$ where $q = k - k_F$ for k near k_F and $q = k + k_F$ for k near $-k_F$. These singularities are due to the spin and charge collective excitations into which an incoming electron is decomposed [113].

The tunneling current between these wires is proportional to a convolution of the spectral functions of the wires. Auslaender *et al.* have observed how this tunneling current changes a function of momentum and polarization [35]. For a small momentum k the slopes of the differential conductance may be used to determine the velocities of the elementary excitations of the wire. The results of such measurements are presented in Fig. 10.3

After performing an analysis involving the capacitance of the wires, these velocities are mapped to the spin and charge velocities of the two wires in the sample. These velocities are assigned to the spin and charge excitations in the wires and being unequal they provide evidence of spin charge separation.

10.3 Localization Transition

In addition to measuring the charge and spin velocities of the electron gas as a function of the density, Auslaender *et al.*[39] found that a peculiar phenomenon occurred whenever the density in the upper wire decreased below $20\mu m^{-1}$ a phenomenon that was further explored by Steinberg *et al.* [41]. Their results for the differential tunneling conductance as a function of bias voltage and magnetic field are shown in Fig. 10.4.

They found that when the density decreased the peaks in the tunneling conductance broadened, corresponding to a state that is localized in real space. They also measured the conductance along the top quantum wire and found that the conductance was quantized and ballistic, meaning that this localization was not an impurity effect. We will delay further discussion of this phenomenon to Section 11.3.

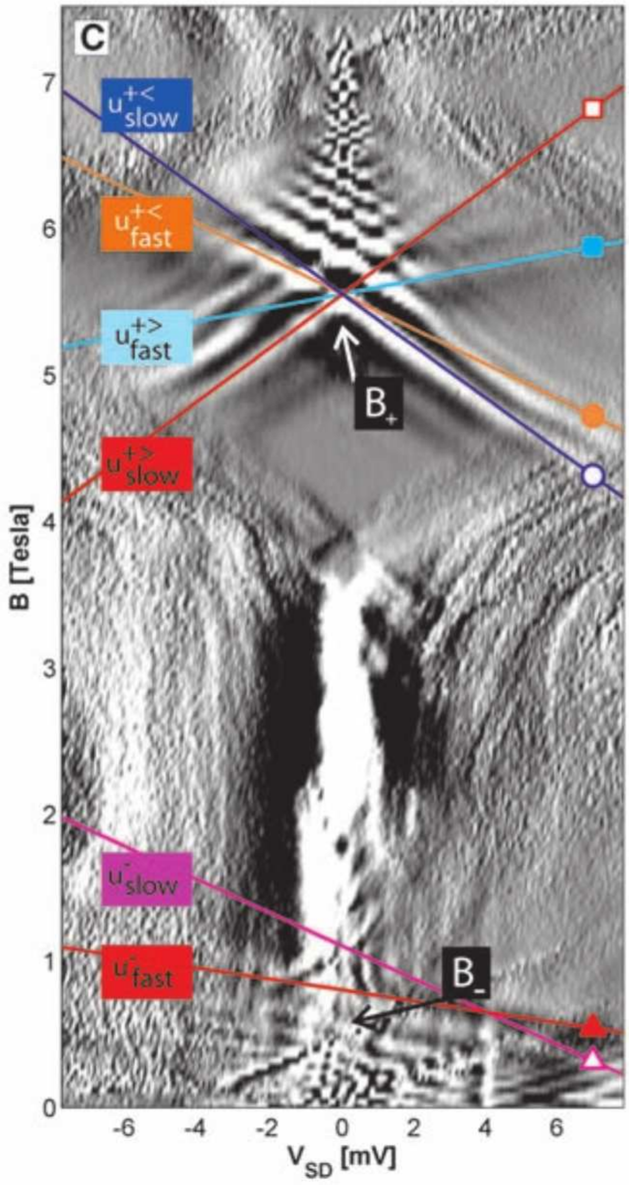

Figure 10.3: This figure shows the differential tunneling current. This velocities of six different modes are found. Figure is from Auslaender *et al.* [39]

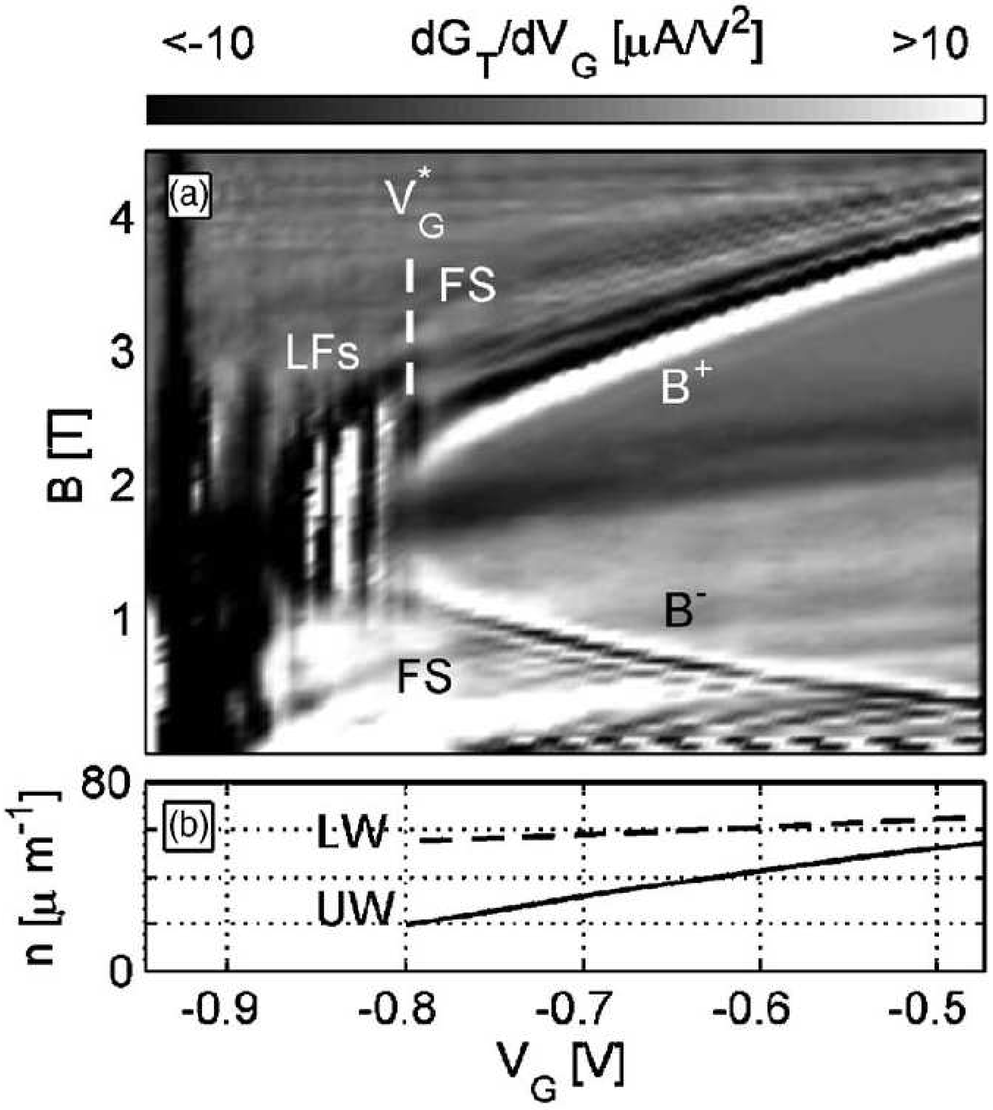

Figure 10.4: Differential tunneling current as a function of the bias voltage and the applied magnetic field. The figure clearly indicates a change in behavior as the bias voltage decreases below $V_G^\star$. The inset at the bottom shows the densities of the upper and lower wires as a function of the gate voltage. This figure is due to Steinberg *et al.* [41].

Chapter 11

Localization Transition: Comparison of Theory and Experiment

In this chapter we present the results of calculations that are designed to provide insight to the experiments described in chapter 10. To this end we assume that the correlation of the electrons between the two wires are weak and that the properties of the electrons in each wire can be calculated by using the approximation that the other wire is a screening medium. Within this model we use the techniques presented earlier in this thesis to calculate the velocities of the charge and spin modes in each wire. Additionally we calculate the density for the localization transition to occur and find a remarkable agreement with the experimentally determined density of $20\mu m^{-1}$.

11.1 Model

The results presented in chapter 6 offer an avenue to explore the role of the electron correlation in the transition observed in the experiment. As the density in the wire decreases the strength of the potential increases relative to the kinetic energy. One effect of this increased relative strength is that exchanges between the electrons are suppressed, causing the system to develop a strong local crystalline order. To better quantify the importance of this effect in the experimental system, in this section we take into account a more realistic potential, assuming the electrons are screened by the lower wire instead of an infinite metallic gate. To construct an interaction potential suitable for this calculation, we neglect the correlation between the wires and treat the screening effects coming from the electrons in the lower wire within the linear response theory. We write the potential in Fourier space

$$V(k,R) = V_b(k) + V_{int}(k,R)\chi(k)V_{int}(k,R), \tag{11.1}$$

where $V_b(k)$ and $V_{int}(k, R)$ defined in Eq. 3.12 are the intra- and inter- wire potentials respectively. $V_{int}(k, R)$ is evaluated by assuming that the thickness of the two wires is the same (and equal to the upper wire). This significantly simplifies the form and the calculation of the inter-wire interaction. $\chi(k)$ is the static density-density response function of the lower wire taken in the RPA:

$$\chi_{RPA}(k) = \frac{\chi_0(k)}{1 - V_{b'}(k)\chi_0(k)} \tag{11.2}$$

where $\chi_0(k) = \frac{1}{\pi k} \ln \left| \frac{k-2k_F}{k+2k_F} \right|$ is the static response function for a one dimensional noninteracting Fermi gas and b' is the width of the lower wire. The experimental geometry sets the parameters in our quasi one dimensional interaction $V(k, R)$.

The confinement potential for the upper wire is chosen so that the electrons are constrained to be inside the $10nm$ thick wire. Specifically, we require that the radial root mean squared displacement is equal to the lithographic thickness yielding $b = 0.707(\approx 1/\sqrt{2})$ for the upper wire. The choice of confinement also agrees well with the experimental observation that a second mode becomes populated at $n = 80\mu m^{-1}$ [35]. Similarly, the lower wire's thickness is given by $b' = 1.061(\approx 1.5/\sqrt{2})$. The distance between the wires is $R = 3.0$, while the Fermi momentum in the RPA response function for the lower wire is set by the density $r_s = 0.83$.

Our screened potential in Eq. 11.1 is similar to that used by Fiete *et al.*[114], who chose a perfect metal response function which is valid when the screening wire is at very high densities. Here we use the RPA which depends on the experimental density of the lower wire through the value of the Fermi momentum k_F. We notice that our screened potential equals that in Ref. [114] at $k = 2k_F$ and in the limit of small k, namely the long-range tail is the same, decaying approximately as $1/x^{\frac{5}{4}}$.

11.2 Spin and Charge Velocities

We determine the charge and spin velocities by means of the QMC method explained in Sec. 7 and the effective J coupling via the WKB approach. We computed those quantities close to the transition for the homogeneous wire with $r_s = 1.25$ ($40\mu m^{-1}$). The charge velocity turns out to be $v_\rho = 2.33 v_F$. The corresponding LL parameter $g = v_F/v_\rho = 0.43$ is in agreement with previous estimates[114] and comparable to the experimental $g \approx 0.5$, measured at the density of $40\mu m^{-1}$.[39] At the same density the experimental value for v_F/v_σ is in the range of $1.1 - 1.6$, while we found $v_F/v_\sigma = 1.24$ at $40\mu m^{-1}$.

In Fig. 11.1 we plot the full dependence of the spin velocities on the density computed with the perturbative generalized RPA (GRPA),[14] WKB and the exact QMC methods. Although the GRPA is poor near the localization transition, it agrees with the QMC at high density. As noted above the experimentally measured spin velocities are also in rough agreement with the QMC estimate in a range of densities around $n = 40\mu m^{-1}$. To show the importance of the microscopic details of the interaction in reproducing the measured values we also display in Fig. 11.1 the GRPA prediction based on a different model potential which assumes a screening due to a metallic gate at $R = 50$.[39] This latter model gives virtually unrenormalized spin velocities ($v_\sigma \approx v_F$) up to $n = 40\mu m^{-1}$ in contrast with the strong suppression of the values found in the experiment and in our calculations.

Last but not least, our WKB estimate of J turns out to be of the order of the experimental temperature ($T = 0.25K$) around $n = 10\mu m^{-1}$. This means that at least the first few Coulomb blockade peaks in the experiment should be in a spin incoherent regime, where the Temperature is greater than the energy to excite a spin excitation. In this case the LL description by Fiete *et al.* applies, although in the vicinity of the transition the spin degrees have a sufficiently high energy that they should not be dominated by the thermal broadening.

11.3 Localization Transition

We first analyze the homogeneous system and then explicitly include a longitudinal confinement in our simulations to quantify the finite-length impact on the properties of the system, and more closely reproduce the experimental situation. In the homogeneous system of electrons interacting via the potential in Eq. 11.1, we observe the appearance of a $4k_F$ peak in the $S(k)$ around $r_s = 2.2$. As shown in Fig. 11.3, it is clearly visible for $r_s > 2.6$, whereas no peak is discernible for $r_s \leqslant 1.9$. This crossover is similar to that found for long range $1/x$ interactions. However, the important difference here is that

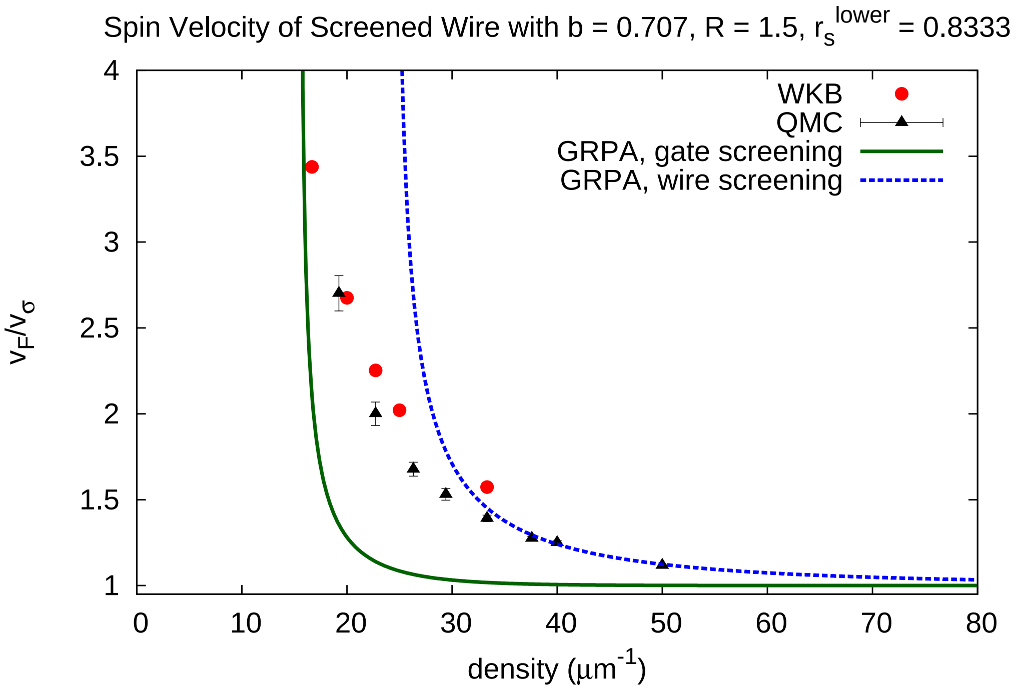

Figure 11.1: Inverse spin velocity of the infinite wire. The red circles indicate estimates from the WKB approximation, whereas the black triangles are determined using the QMC method described in chapter 7. The two lines are estimates due to the perturbative generalized random phase approximation (GRPA)[14]: $v_F/v_\sigma^{GRPA} = 1/\sqrt{1 - V(2k_F)/(\pi v_F)}$. The green line for the gated wire (with $R = 50$) uses the potential described by Auslaender *et al.*[39] whereas the dotted blue line uses the potential (Eq. 11.1) screened by the lower wire.

the quasi long-range order is not present in this case. Indeed, as in section 6.2 we have made a systematic study of the scaling with size, and the height of the peak converges to a finite value in the thermodynamic limit for all densities taken into account. This behavior is consistent with the decay of the screened interaction found in section 6.3, which is *faster* than $1/x$ [10]. Therefore, the crossover is between a high-density liquid to one with strong $4k_F$ correlations, whose onset can be related to the transition occurring in the experimental system.

11.3.1 Confined Electrons

The above treatment of the upper wire as infinite and homogeneous can be improved to resemble the experiments more closely. In the study of the

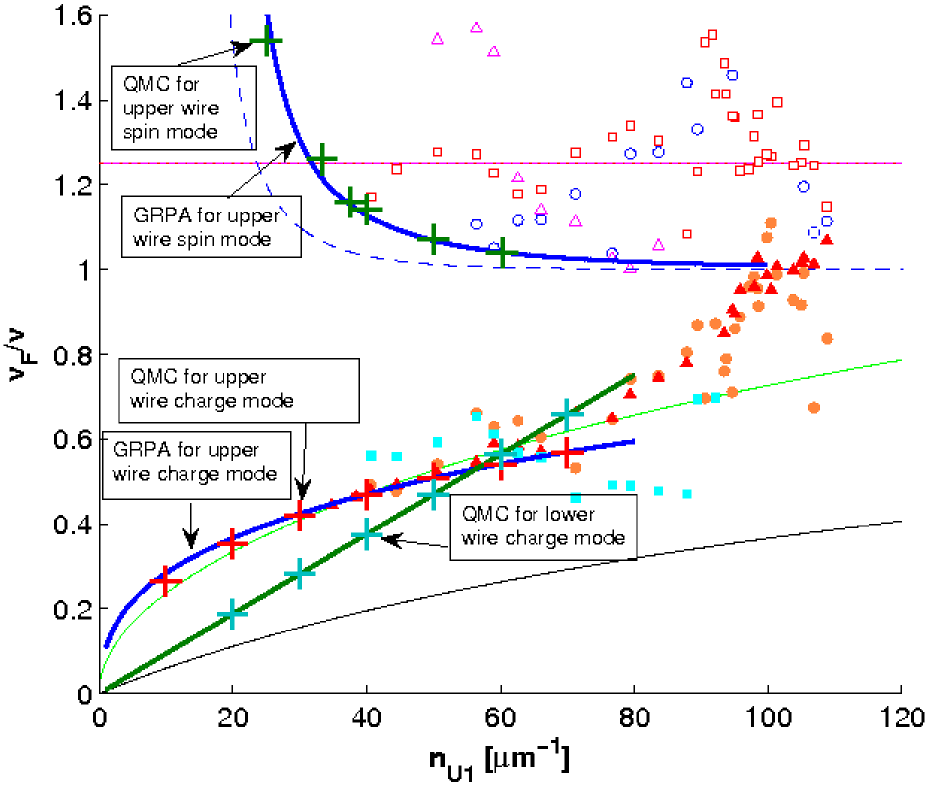

Figure 11.2: Inverse charge and spin velocity of the infinite wire. The calculations were performed with an upper wire thickness $b = 1$ and a lower wire thickness $b = 1.5$. Points from both experiments by Auslaender et. al. and our QMC calculations. Graph was produced in collaboration with O. Auslaender

1DEG there are strong effects due to any perturbation that breaks the translational invariance of the system. For instance, Tserkovnyak *et al.* showed that the asymmetry in the oscillations of the conductance as a function of the momentum transferred between the two wires can be explained at the WKB level by having a soft confinement potential for the upper wire.[36] In a later paper they accurately determined the functional form of the longitudinal confinement by fitting its parameters to reproduce the period of those oscillations as a function of the magnetic field applied to the sample.[37] The potential that provided a good fit to their data reads

$$V(x) = E_F \left(\frac{2x}{L}\right)^8, \tag{11.3}$$

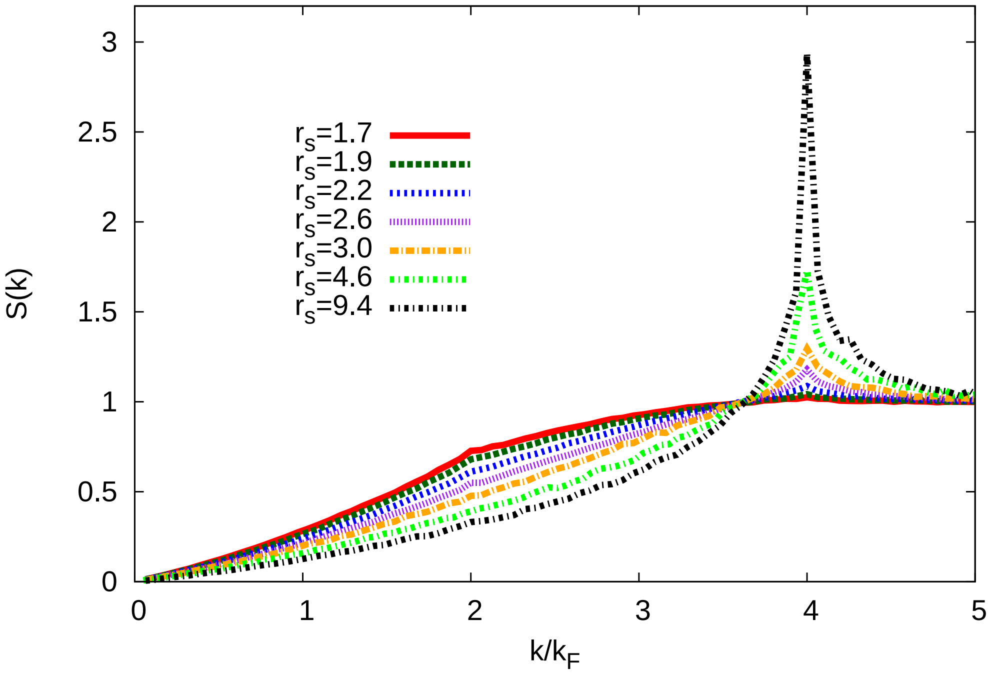

Figure 11.3: Static structure factor for a homogeneous wire with $b = 0.707$ interacting with the effective potential in Eq. 11.1, which includes the screening by another homogeneous wire with $r_s = 0.83$, $b = 1.061$, and $R = 3$. The structure factor is plotted for several values of the upper wire density, with r_s ranging from 1.7 to 9.4. The calculations have been converged to the thermodynamic limit, requiring $N = 62$ for $r_s \leq 3.0$ and $N = 78$ subject to periodic boundary conditions for $r_s = 4.6$ and 9.4.

where E_F is the Fermi energy of the upper wire, and L is approximately 1.5 times the lithographic length of the upper wire, namely $L = 300$ in $a_0^\star$ units.

We used the above potential together with the interparticle potential in Eq. 11.1 to study the effect of the confinement on the transition. Although in principle diffusion Monte Carlo yields an unbiased ground state energy in one dimension even for a confined system, (the nodes being exactly determined by the coalescence conditions just as in the infinite homogeneous wire) in practice it is necessary to improve the guidance wave function to reduce the variance of our estimates. The Jastrow factor used in the homogeneous system (Eq. 4.10) is replaced by a more sophisticated factor including one-, two-, and three-body terms, fully optimized by means of the stochastic reconfiguration (SR) algorithm,[115, 116] while the Slater part is kept the same as in Eq. 4.7. The one-body Jastrow $\exp(J_1)$ is needed to localize the electrons in the finite system. It reads

$$J_1 = \sum_{i=1}^{N} \left(-\alpha x_i^4 - \beta x_i^5 \right) , \tag{11.4}$$

where α is a free parameter and $\beta = \sqrt{E_u}(2/L)^4/5$ is fixed to cancel the contribution of the potential to the local energy at the leading order in the large distance expansion. The two-body $\exp(J_2)$ and three-body $\exp(J_3)$ Jastrow factors are given by

$$J_2 = \sum_{(i\sigma)<(j\sigma')} u_2^{\sigma\sigma'}(x_{ij}), \tag{11.5}$$

and

$$J_3 = \sum_{(i\sigma),(j\sigma'),(k\sigma'')} u_3^{\sigma\sigma'}(x_{ij})\; u_3^{\sigma'\sigma''}(x_{jk}), \tag{11.6}$$

where x_{ij} is the interparticle distance. Since the finite system with screened interactions is dominated by short-range correlations, we chose $u_n(x)$ to have a simple Gaussian form

$$u_n^{\sigma\sigma'}(x) = \delta_n^{\sigma\sigma'} \exp\left(-x^2/\gamma_n^{\sigma\sigma'} \right) , \tag{11.7}$$

with $\delta_n^{\sigma\sigma'}$ and $\gamma_n^{\sigma\sigma'}$ variational parameters. Energy minimization improves the quality of the variational wave function and stabilizes the forward walking estimate[62] of the expectation values on the DMC projected state.

Again the static structure factor is determined for different densities of electrons in the upper wire. In contrast to the calculations for the homogeneous system, the density of the electrons is not a direct input to the calculation. Instead, we control the number of electrons in the wire which are then free to relax according to the external potential. An average density can be determined by considering the locations of the $2\tilde{k}_F$ and $4\tilde{k}_F$ peaks of the structure factor and comparing their value to those of an infinite array of electrons, $2\tilde{k}_F = \frac{\pi}{2\tilde{r}_s}$ and $4\tilde{k}_F = \frac{\pi}{\tilde{r}_s}$, $\tilde{r}_s$ being the effective density in the system. Using these conventions, the structure factor for several different numbers of electrons is plotted in Fig. 11.4.

In addition to the formation of a broad peak in the $S(k)$ at $4k_F$ around $N = 80$, which corresponds to $\tilde{r}_s = 2.3$, the density profile $n(x) = \langle \sum_i \delta(x -$

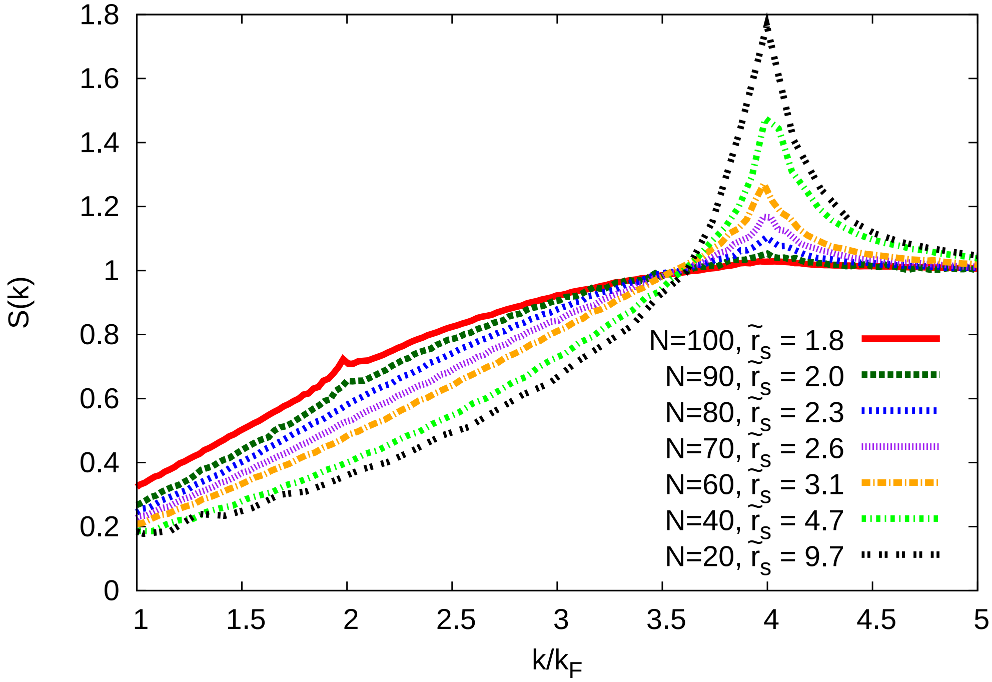

Figure 11.4: Static structure factor for a wire as in Fig. 11.3, but with finite length $S(k)$ is plotted for 20, 40, 60, 70, 80, 90 and 100 electrons. The corresponding effective densities $\tilde{r}_s$ are reported in the legend.

$x_i)\rangle$ of the electrons also shows a clear cut sign of the transition. At low densities, the electrons are distributed in order to minimize the interparticle repulsion. This leads to N oscillations in the density profile of the wire, a configuration also called "Wigner molecule",[117] which corresponds to the $4k_F$ peak in the $S(k)$. When the density is increased, the number of peaks in the density profile is reduced by a factor of two, the Pauli exclusion principle between like spin particles being the only factor that prevents the electrons form crossing each other. At the same time the $4k_F$ peak in the $S(k)$ disappears and only a $2k_F$ singularity is present. The density is plotted in Fig. 11.5 for half of the wire as the system is symmetric under inversion around its center. This plot also suggests a transition near $N = 80$.

Surprisingly, the calculations with the confinement potential and the infinite wire give very similar structure factors in the vicinity of the transition, suggesting that the interparticle correlations are not strongly affected by the external confinement at those densities. At lower densities the peak at $4k_F$ is much larger for the homogeneous system because of the limited number of

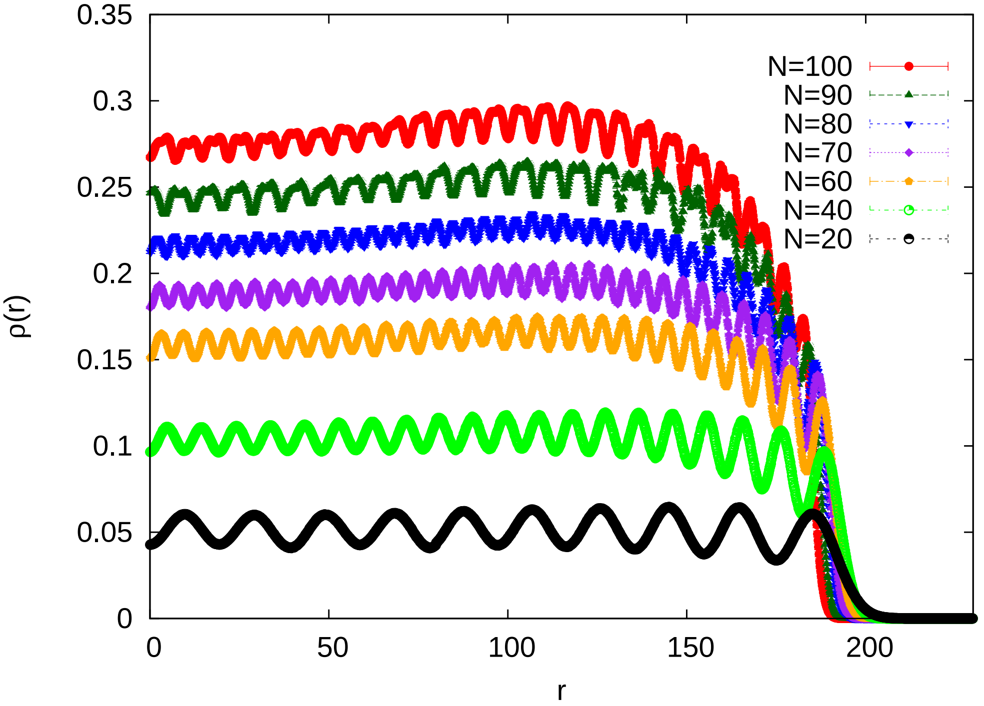

Figure 11.5: Density profile for electrons in the finite wire as in Fig. 11.4, plotted for half of the wire length. $N = 20$, 40, 60, 70, 80, 90 and 100 are considered.

particles in the finite wire. Both the infinite and finite wires show a transition from a system with $2k_F$ correlations to a state where correlations have a $2r_s$ periodicity. The crossover occurs around $r_s = 2.3$, which corresponds to the density of $22\mu m^{-1}$ in a GaAs heterostructure. This is very close to the density found by Steinberg *et al.* ($20\mu m^{-1}$) for the localization transition in wires where one subband is occupied.

11.4 Refinements

It seems that in the experiment the localization involves only few particles (up to 12 in the highest density localized state), i.e. only a section of the wire takes part in the transition. This is an important difference with respect to our calculations where the transition takes place throughout the system in a quite homogeneous way. A non homogeneous behavior is found at the edge of the wire where the confining potential in Eq. 11.3 turns upward. There the transition happens at higher densities, as one can see in Fig. 11.5. This can be understood in terms of a local mean field description. At the edge of the wire the effective chemical potential $\mu_0 - V(x)$ is smaller, corresponding locally to a fluid at much lower density.

Apart from these features, we did not find any Wigner correlated patch embedded in a liquid-like system, which seems to be the experimental outcome. Therefore a more detailed analysis of the experimental setup is required to understand better the experiment. For instance, one of the top metallic gates used to tune the upper wire density could induce a plateau in the external potential, nucleating a Wigner region as suggested by Mueller.[118] On the other hand, the role of disorder is not clear. Although in the liquid phase the system is in a ballistic regime, when the conductance is quantized the disorder could take over in the localized phase and affect the charge distribution in the wire. AlAs wires, where the disorder is stronger, revealed conductance resonances explained in terms of Coulomb blockade (CB) physics.[119] CB behavior has also been found in the localized phase of GaAs wires.[41]

Even if there are features that still need explanation, our calculations show that the electronic correlation plays a very important role at the experimental conditions, as the $2k_F$-to-$4k_F$ correlations transition takes place exactly in the proximity of the critical density for localization found in the experiment.

Chapter 12

Conclusions

This dissertation has presented several contributions to the interface between theory and experimental realizations one dimensional phenomena. Chapter 3 presented a model whereby the quantitative properties of a quasi one dimensional electron gas could be calculated. Within this model an understanding of the behavior of the total energy of the electron gas as a function of density and polarization is developed, culminating in extensive and exact QMC calculations of the energy. Two parameterizations of these energies are presented in the appendix with a potential application in the density functional theory of low dimensional electrons.

Considerable attention was paid to the properties of the one dimensional gas with long range $1/x$ interactions. These interactions were known to cause quasi Wigner Crystal behavior from previous theoretical work. To our knowledge this is the first qualitative study to analyze the onset of this quasi Wigner crystal behavior in a continuous system. Our study showed that these correlations become important in a crossover from a liquid like state that favors $2k_F$ correlations to a quasi Wigner Crystal state favoring $4k_F$ correlations as the interaction strength increases (decreasing density in the case of the electron gas). This crossover was marked by the formation of a peak in the static structure factor at $4k_F$ as the density was decreased. Additionally the charge compressibility of the gas softened in the vicinity of this transition.

The introduction of screening is crucial for the understanding of experimental realizations of quasi one dimensional electrons. Schulz predicted that any screening would destroy the long range correlations of the electron gas[10], a finding that we confirmed. There was however a local $4k_F$ correlation that formed as the density decreased analogously to the unscreened case. As the density decreased even further, interactions suppressed the exchange of the electrons (which is primarily governed by short range repulsion). When the density was decreased to a low enough value, the electrons behaved as spinless fermions. For a sufficiently strong screened interaction these spinless fermions began to appear noninteracting, a situation that has strong parallels to the fermionization of ultra cold boson gases as predicted by Tonks and Girardeau.

The onset of the short range density oscillations proved to be a useful lens through which a localization transition in quantum semiconductor wires could be examined. Our work found that correlations could be responsible for the localization transition observed by Steinberg *et al.* [41]. This is an important confirmation as scattering off impurities can also cause such a localization transition. Indeed impurities have dominated the properties of earlier quantum semiconductor wires [119]. Furthermore, we predicted the density at which this transition occurs to be $22\mu m^{-1}$ in remarkably good agreement with the observed transition at $20\mu m^{-1}$. Additionally the charge and spin velocities of the wire were calculated from the long wavelength charge and spin excitation energies and found to be in agreement with the experiments.

Appendix A

Parameterizations of the Energy for LSDA Calculations

This appendix will present two parameterizations of the energy of the quasi one dimensional electron gas with $b = 1$. The successes and failures of the two parameterizations will be discussed.

A.1 Correlation Functional

This section presents a parameterization of the correlation energy of the electron gas. Use of this parameterization assumes that the exchange and one body kinetic energies are calculated separately using Eq.5.3 and Eq.5.2.

The following is the form for this parameterization:

$$\epsilon_c(r_s,\zeta) = \epsilon_c(r_s,0) - Cr_s^2\zeta^2(1+\zeta^2) + \frac{2\zeta^2(\epsilon_c(r_s,1) - \epsilon_c(r_s,0) + Cr_s^2(1+\zeta^2))}{1+e^{(1-|\zeta|)^\gamma/t(r_s)}} \tag{A.1}$$

$$\epsilon_c(r_s,0) = -\frac{r_s + a_0r_s^2}{b_0 + c_0r_s + d_0r_s^2 + e_0r_s^3}\ln(1 + 2b_0Cr_s + \alpha_0r_s^{\beta_0}) \quad \text{with } \beta_0 > 1 \tag{A.2}$$

$$\epsilon_c(r_s,1) = -\frac{r_s + a_1r_s^2}{b_1 + c_1r_s + d_1r_s^2 + e_1r_s^3}\ln(1 + \frac{1}{4}b_1Cr_s + \alpha_1r_s^{\beta_1}) \quad \text{with } \beta_1 > 1 \tag{A.3}$$

$$t(r_s) = t_1r_se^{-r_s/t_3} + t_2(1 - e^{-r_s/t_3})/\ln(1 + \frac{t_4}{r_s^3}) \tag{A.4}$$

$$C = \frac{\int_0^\infty zv^2(z)dz}{2\pi^4b^2} \approx \frac{4.9348}{2\pi^4b^2} \tag{A.5}$$

Equations A.2 and A.3 have a functional form similar to the one previously chosen in the parameterization of the correlation energy for the unpolarized wire.[43]. The second order Pade used in that work is replaced here with a third order form to allow for a more flexible fit. Notice that the r_s

dependence of the correlation energy

$$\epsilon_c(r_s,\zeta) - \epsilon_c(r_s,0) = \epsilon_x(r_s,0) - \epsilon_x(r_s,\zeta) = -\frac{\zeta^2}{2}\frac{\ln r_s}{r_s} + O\left(\frac{1}{r_s}\right). \tag{A.6}$$

at high density is fulfilled exactly by this functional form (Eq. 5.16), while in the low density limit these functional forms have the guessed leading order behavior ($\frac{\ln r_s}{r_s}$).

Eq. A.1 is constructed so that at $\zeta = 0$ and $\zeta = 1$ it reduces to $\epsilon_c(r_s, 0)$ and $\epsilon_c(r_s, 1)$ respectively. Furthermore, it allows for the spin dependence to be interpolated between the discontinuous behavior at small r_s and the low density behavior given by Eq. A.6. This is realized via the inclusion of the exponential function in the denominator, which accounts also for the abrupt change of the ζ dependence in the high density limit. Eq. A.4 is derived from assuming the functional form of Eq. A.1 and requiring the validity of Eq A.6 up to $O\left(\frac{1}{r_s}\right)$.

In the limit of a high density and with $\zeta \neq 1$, $t(r_s) \propto r_s$ and the parameterization has the following limiting behavior

$$\begin{aligned}\lim_{r_s\to 0} \epsilon_c(r_s,\zeta) &= \lim_{r_s\to 0} \epsilon_c(r_s,0) - Cr_s^2\zeta^2(1+\zeta^2) \\ &= -Cr_s^2(2+\zeta^2+\zeta^4).\end{aligned} \tag{A.7}$$

Around $\zeta = 0$, this is equivalent to the RPA result of $Cr_s^2(1+\frac{1}{1+\zeta^2})$.

In the limit of low density, Eq. A.4 is proportional to r_s^3, so the RPA inspired terms in the fit, $Cr_s^2\zeta^2(1+\zeta^2)$, cancel exactly and the correlation energy becomes

$$\begin{aligned}\lim_{r_s\to\infty} \epsilon_c(r_s,\zeta) &= \lim_{r_s\to\infty} \zeta^2\epsilon_c(r_s,1) + (1-\zeta^2)\epsilon_c(r_s,0)) \\ &= -\left[\zeta^2\frac{a_1\beta_1}{e_1} + (1-\zeta^2)\frac{a_0\beta_0}{e_0}\right]\frac{\ln r_s}{r_s}\end{aligned} \tag{A.8}$$

We have assumed in this work that the correlation energy is independent of the polarization at low density, so this equation is combined with Eq. A.6 to produce a constraint on the values of the parameters used in the fit:

$$\frac{a_0\beta_0}{e_0} - \frac{a_1\beta_1}{e_1} = \frac{1}{2} \tag{A.9}$$

Therefore, there are a total of 18 free parameters in the fit.

A.1.1 Correlation Functional Fit for b = 1

This section gives the values of the various parameters that are obtained by fitting the LRDMC values of the correlation energy obtained at 17 different densities ranging from $r_s = 0.1$ to $r_s = 50$. From $r_s = 0.1$ to $r_s = 1.5$ nine values of the polarization were used equally spaced from $\zeta = 0$ to $\zeta = 1$. For $r_s > 1.5$, five polarizations $\zeta = 0, \frac{1}{4}, \frac{1}{2}, \frac{3}{4}$, and 1 were used. These parameters produce a fit that has a reduced χ^2 of 4.3325.

a_0	9.63896e-05
b_0	30.29814
c_0	4.310638
d_0	7.698245
e_0	0.001316096
α_0	0.2004351
β_0	4.1671072

Table A.1: Parameter Values for the Fit of $\epsilon_c(r_s, 0)$

a_1	1.240455e-10
b_1	1046.83128
c_1	104.26146
d_1	66.70879
e_1	0.0825241
α_1	162.42691
β_1	3.29819

Table A.2: Parameter Values for the Fit of $\epsilon_c(r_s, 1)$

t_1	0.9147124
t_2	6.777327
t_3	0.675004
t_4	17.43468

Table A.3: Parameter Values for the Fit of t(r_s)

γ	0.8714030

Table A.4: Value of Exponent in Eq. A.1

A.1.2 Validation of Correlation Functional

Aside from the high quality fit as determined by the reduced chisquared, it is important to ask if the functional form determined above satisfies the constraints derived in section 5.1. The correlation energy vs ζ is plotted a high density in Fig. A.1. This shows hallmarks of the RPA dependence of the energy on the polarization (Eq. 5.16).

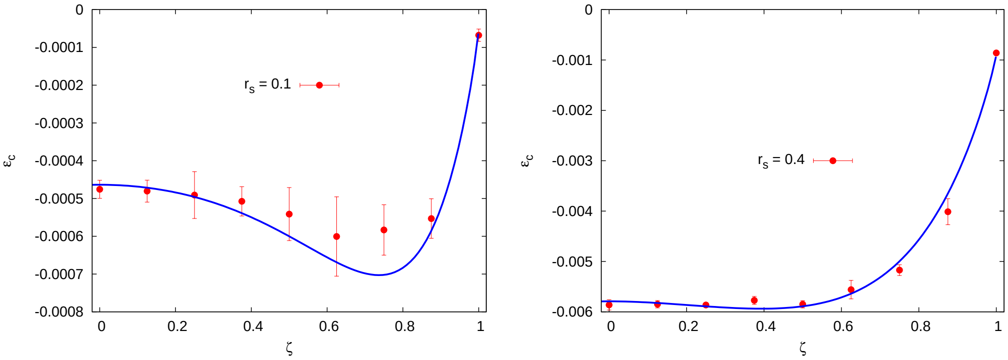

Figure A.1: Correlation energy ϵ_c vs the polarization ζ at high density. The solid line comes from the parameterization while the points come from QMC calculations.

The situation at low density is not as encouraging. The total energy as a function of the polarization is plotted in Fig. A.2. Although the QMC calculations agree with the Lieb-Mattis theorem requiring the total energy to be a monotonically increasing function of the polarization, the energies derived from the parameterization do not. This calls into question the validity of the functional for densities less than $r_s \approx 4$.

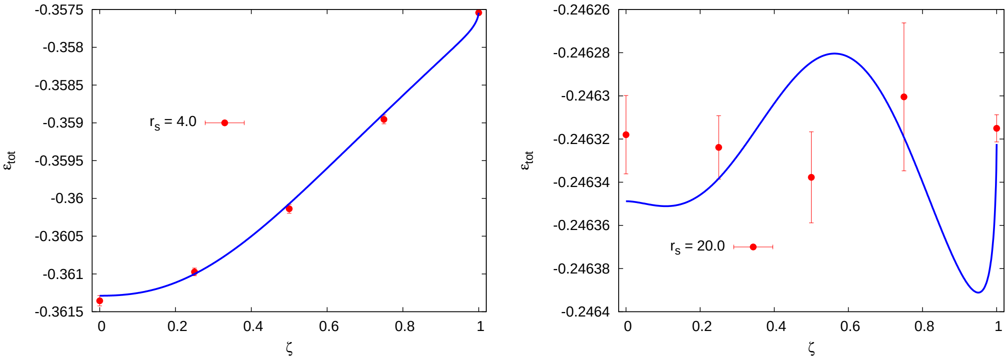

Figure A.2: Total energy ϵ_t vs the polarization ζ at low density. The solid line comes from the parameterization while the points come from QMC calculations.

A.2 Exchange Correlation Functional

This section presents a parameterization of the exchange correlation energy that is derived in such a way as to reproduce the low density spin dependence of the electron gas given in Sec. 5.1.2. This parameterization includes both the exchange and correlation energies and so there is no need to calculate Eq. 5.3. This functional form is:

$$\begin{aligned}\epsilon_{xc}(r_s,\zeta) &= \epsilon_{xc}^{\mathrm{con}}(r_s,0) + h_z(r_s,\zeta) - c_z(r_s,\zeta) + \frac{1}{1+e^{t(r_s)(1-\zeta)^{\gamma}}} \\ &\quad [2(a(r_s)\zeta^2 + (1-a(r_s))\zeta^4)(\epsilon_{xc}(r_s,1) - \epsilon_{xc}^{\mathrm{con}}(r_s,0)) - 2(h_z(r_s,\zeta) - c_z(r_s,\zeta))]\end{aligned} \tag{A.10}$$

$$\epsilon_{xc}(r_s,1) = \frac{a_1 + b_1 r_s + c_1 r_s^2}{1 + d_1 r_s + e_1 r_s^2 + f_1 r_s^3} + \frac{g_1 x \ln[x + t_1 x_1^u]}{1 + h_1 r_s^2} \tag{A.11}$$

$$\epsilon_{xc}(r_s,0) = \frac{a_0 + b_0 r_s + c_0 r_s^2}{1 + d_0 r_s + e_0 r_s^2 + f_0 r_s^3} + \frac{g_0 x \ln[x + t_0 x_0^u]}{1 + h_0 r_s^2} \tag{A.12}$$

$$\epsilon_{xc}^{\mathrm{con}}(r_s,0) = \frac{\epsilon_{xc}(r_s,0)}{1+e^{-\frac{r_s-o}{r r_s}}} + \left(1 - \frac{1}{1+e^{-\frac{r_s-o}{r r_s}}}\right)(\epsilon_{xc}(r_s,1) - \ln(2)J(r_s) + \frac{\pi^2}{16 r_s^2}) \tag{A.13}$$

$$t(r_s) = \frac{t_1 e^{-t_2 r_s}}{r_s} + t_3(1 - e^{-t_2 r_s}) \log\left(1 + \frac{e^{-t_4 r_s}}{r_s^5}\right) \tag{A.14}$$

$$a(r_s) = 1 - \left(\frac{p_1}{r_s} + 1\right) e^{-p_2 r_s} \tag{A.15}$$

$$h_z(r_s,\zeta) = \frac{r_s \log(1-\zeta^2)}{b^2\pi^2},\ c_z(r_s,\zeta) = C r_s^2 \left(\frac{1}{1-\zeta^2} - 1\right), \tag{A.16}$$

where $C = \frac{\int_0^\infty z v^2(z) dz}{\pi^4 b^2} \approx \frac{4.9348}{\pi^4 b^2}$ and $J(r_s) = \frac{j_1}{(2r_s)^{1.25}} e^{-j_2\sqrt{2r_s}}$ At first inspection this parameterization looks considerably more complex than the correlation functional of section A.1. However many of these terms are constrained by theory and the resulting form has only 23 free parameters compared to the 18 in the correlation function parameterization.

The form of Eq. A.10 was chosen to constrain the parameterization to attain energies determined by the exchange correlation energy from equations A.13 and A.11. This allows the parameterization to in principle satisfy the non analytic behavior of the correlation energy at high density. The energy for $\zeta = 0$ was constrained using the difference between the fully polarized and unpolarized states of the antiferromagnetic spin chain with coupling constant $J(r_s)$ which is determined using the WKB approximation. This constraint is enforced upon the $\zeta = 0$ fit ϵ_{xc}^{con} because the QMC calculations converge most rapidly for $\zeta = 1$ and thus it is a natural choice for the reference. Finally $h_z(r_s, \zeta)$ and $c_z(r_s, \zeta)$ are the high density expansions of the exchange energy and the RPA correlation energy.

A.2.1 Exchange Correlation Function Fit for b = 1

This section gives the values of the various parameters that are obtained by fitting the LRDMC values of the exchange correlation energy obtained at 17 different densities ranging from $r_s = 0.1$ to $r_s = 50$ as in section A.1.1. From $r_s = 0.1$ to $r_s = 1.5$ nine values of the polarization were used equally spaced from $\zeta = 0$ to $\zeta = 1$. For $r_s > 1.5$, five polarizations $\zeta = 0, \frac{1}{4}, \frac{1}{2}, \frac{3}{4}$, and 1 were used. These parameters produce a fit that has a reduced χ^2 of 7.97.

a_0	-0.8862269
b_0	-0.5599325
c_0	-0.5031898
d_0	1.03571
e_0	0.930169
f_0	0.672727
g_0	-0.200759
h_0	0.722865
t_0	0.0897963
u_0	3.81785
r	9.39712
o	8.23353

Table A.5: Parameter Values for the Fit of $\epsilon_{xc}^{con}(r_s, 0)$

a_1	-0.8862269
b_1	-0.3884956
c_1	-0.1833389
d_1	0.716571
e_1	0.400009
f_1	0.178259
g_1	-0.101321
h_1	0.289932
t_1	0.0888642
u_1	2.96153

Table A.6: Parameter Values for the Fit of $\epsilon_{xc}(r_s, 1)$

t_1	18.0322
t_2	8.67834
t_3	0.927153
t_4	0.0732567

Table A.7: Parameter Values for the Fit of $t(r_s)$

p_1	0.944023
p_2	0.192086

Table A.8: Parameter Values for the Fit of $a(r_s)$

j_1	184.53
j_2	-2.84968

Table A.9: Parameter Values for the Fit of $J(r_s)$

γ	1.82183

Table A.10: Value of the Exponent in Eq. A.10

A.2.2 Validation of Exchange Correlation Functional

As was the case with the correlation functional of section A.1, it is important to understand the ability of the functional to satisfy the constraints derived in section 5.1. The exchange correlation energy is plotted at several values of the density in Fig. A.3.

The exchange correlation energy is in good agreement with the parameterization at all densities. However, upon subtracting the exchange energy, the agreement is not convincing at high densities as shown in figure A.4. For this reason this functional is recommended only for low densities or if high densities must be obtained the polarization should be small.

A.3 Exchange Correlation Energies

This section will provide the underlying data that was fit to produce the functionals proposed in the previous sections. In all cases the energy reported is the exchange correlation energy per electron extrapolated to the thermodynamic limit. This energy is defined as the total energy from the calculation minus the contribution of the single particle kinetic energy determined from

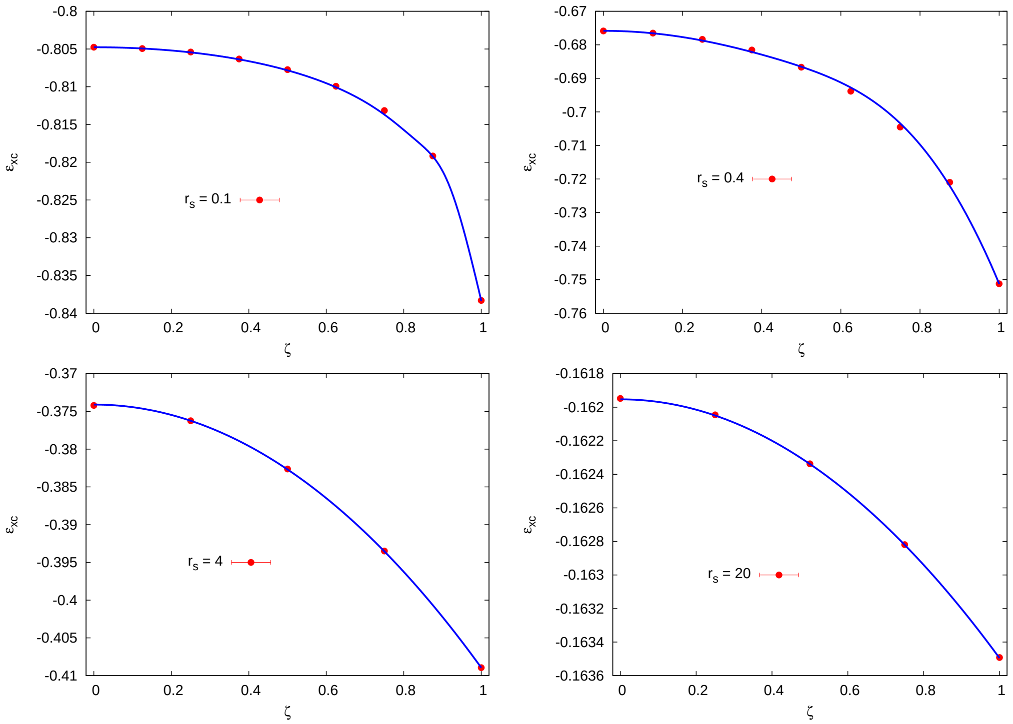

Figure A.3: Exchange Correlation energy ϵ_{xc} vs the polarization ζ at high density. The solid line comes from the parameterization while the points come from QMC calculations.

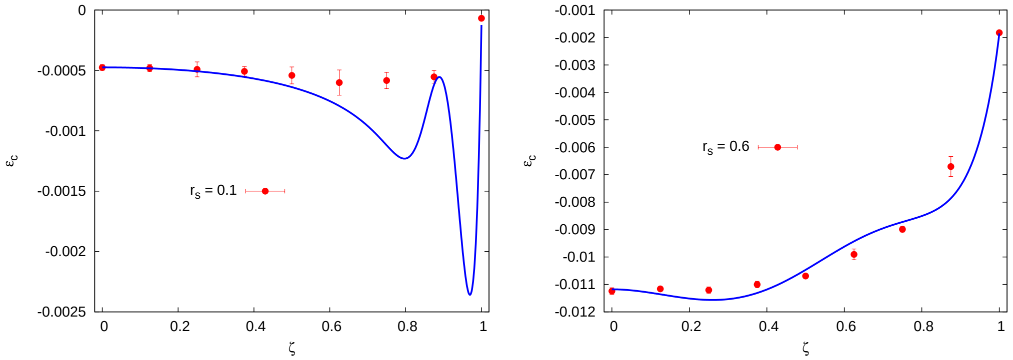

Figure A.4: Correlation energy ϵ_c vs the polarization ζ at high density. The solid line comes from the parameterization while the points come from QMC calculations.

the noninteracting electron gas

$$\epsilon_{xc}(r_s,\zeta) = \epsilon_t(r_s,\zeta) - \frac{(1+3\zeta^2)\pi^2}{48r_s^2} \tag{A.17}$$

The energy is reported in Rydberg with the uncertainty in the value due to the statistical nature of the Monte Carlo simulations indicated in parenthesis.

r_s	$\zeta = 0$	$\zeta = 0.25$	$\zeta = 0.5$	$\zeta = 0.75$	$\zeta = 1$
0.1	-0.804765(12)	-0.805401(31)	-0.807729(35)	-0.813154(33)	-0.838308(8)
0.2	-0.752136(39)	-0.753397(25)	-0.757934(31)	-0.768287(33)	-0.804550(15)
0.4	-0.675868(51)	-0.678375(88)	-0.686673(36)	-0.704528(53)	-0.751223(17)
0.6	-0.621040(61)	-0.624448(57)	-0.635422(39)	-0.658171(50)	-0.708706(18)
0.8	-0.579283(49)	-0.583094(51)	-0.595971(43)	-0.621683(89)	-0.672996(12)
1.0	-0.546296(49)	-0.550512(48)	-0.564459(61)	-0.591776(62)	-0.642186(14)
1.5	-0.488602(37)	-0.493120(38)	-0.507758(80)	-0.535145(85)	-0.579987(21)
2.0	-0.452376(31)	-0.456625(34)	-0.470079(40)	-0.49431(11)	-0.531848(28)
3.0	-0.407230(30)	-0.410357(34)	-0.419772(34)	-0.436404(36)	-0.460531(8)
4.0	-0.374206(34)	-0.376233(25)	-0.382627(29)	-0.393491(30)	-0.408946(11)
6.0	-0.320707(16)	-0.321747(17)	-0.324883(28)	-0.330111(16)	-0.337458(6)
8.0	-0.279824(8)	-0.280427(9)	-0.282223(13)	-0.285210(25)	-0.2894199(57)
10.0	-0.248374(9)	-0.248766(7)	-0.249936(11)	-0.251826(17)	-0.2545471(31)
15.0	-0.195149(3)	-0.195322(5)	-0.195834(7)	-0.196689(5)	-0.1978972(23)
20.0	-0.161948(2)	-0.162046(3)	-0.162338(5)	-0.162819(3)	-0.1634919(18)
35.0	-0.109642(1)	-0.109672(1)	-0.109768(1)	-0.109926(2)	-0.1101496(7)
50.0	-0.0842848(8)	-0.0842984(5)	-0.0843405(8)	-0.0844203(6)	-0.0845317(5)

Table A.11: Exchange Correlation Energies for $b = 1$

References

[1] J. M. Luttinger, J. Math. Phys. **4**, 1154 (1963).

[2] S. Tomonaga, Prog. Theor. Phys. **5**, 554 (1950).

[3] J. Voit, Rep. Prog. Phys. **58**, 977 (1995).

[4] A. M. Chang, Rev. Mod. Phys. **75**, 1449 (2003).

[5] T. Giamarchi, *Quantum Physics in One Dimension*, Clarendon Press, Oxford, 2004.

[6] P. Phillips, *Advanced Solid State Physics*, Westview Press, Boulder, CO, 2003.

[7] G. F. Giuliani and G. Vignale, *Quantum Theory of the Electron Liquid*, Cambridge University Press, Cambridge, 2005.

[8] D. C. Mattis and E. H. Lieb, J. of Math. Phys. **6**, 304 (1965).

[9] J. V. José, L. P. Kadanoff, L. P. Kirkpatrick, and D. R. Nelson, Phys. Rev. B **16**, 1217 (1977).

[10] H. J. Schulz, Phys. Rev. Lett. **71**, 1864 (1993).

[11] N. Mermin and H. Wagner, Phys. Rev. Lett. **17**, 1133 (1966).

[12] N. Mermin, Phys. Rev. **176**, 250 (1968).

[13] W. Häusler, L. Kecke, and A. H. MacDonald, Phys. Rev. B **65**, 085104 (2002).

[14] C. E. Creffield, W. Häusler, and A. H. MacDonald, Europhys. Lett. **53**, 221 (2001).

[15] H. Grabert and M. H. Devoret, editors, *Single Charge Tunneling: Coulomb Blockade Phenomena in Nanostructures*, Plenum Press, New York, 1992.

[16] X. G. Wen, Phys. Rev. B **41**, 12838 (1990).

[17] A. M. Chang, Rev. Mod. Phys. **75**, 1449 (2003).

[18] M. Grayson, D. C. Tsui, L. N. Pfeiffer, K. W. West, and A. M. Chang, Phys. Rev. Lett. **80**, 1062 (1998).

[19] S. Roddaro et al., Phys. Rev. Lett. **90**, 046805 (2003).

[20] M. S. Dresselhaus, G. Dresselhaus, and P. C. Eklund, *Science of Fullerenes and Carbon Nanotubes*, Academic Press, San Diego, CA, 1995.

[21] Z. Yao, H. W. C. Postma, L. Balentz, and C. Dekker, Nature **402**, 273 (1999).

[22] M. Bockrath et al., Nature **397**, 598 (1999).

[23] V. V. Deshpande and M. Bockrath, Nature Phys. **4**, 314 (2008).

[24] H. Feshbach, Ann. Phys. **5**, 357 (1958).

[25] U. Fano, Phys. Rev. **124**, 1866 (1961).

[26] S. Inouye et al., Nature **392**, 151 (1998).

[27] B. Paredes et al., Nature **429**, 277 (2004).

[28] T. Kinoshita, T. Wenger, and D. S. Weiss, Science **305**, 1125 (2004).

[29] M. Girardeau, J. Math. Phys. **1**, 516 (1960).

[30] M. Fogler, Phys. Rev. Lett. **94**, 056405 (2005).

[31] M. Fogler, Phys. Rev. B **71**, 161304 (2005).

[32] P. Kakasvili, S. G. Ghongale, H. Pu, and C. J. Bolech, cond-mat **0804.1144**.

[33] L. N. Pfeiffer et al., Appl. Phys. Lett. **56**, 1697 (1990).

[34] R. Schuster et al., Phys. Stat. Sol. C **1**, 2028 (2004).

[35] O. M. Auslaender et al., Science **295**, 825 (2002).

[36] Y. Tserkovnyak, B. Halperin, O. Auslaender, and A. Yacoby, Phys. Rev. Lett. **89**, 136805 (2002).

[37] Y. Tserkovnyak, B. Halperin, O. Auslaender, and A. Yacoby, Phys. Rev. B **68**, 125312 (2003).

[38] O. M. Auslaender et al., Sol. Stat. Comm. **131**, 657 (2004).

[39] O. M. Auslaender et al., Science **308**, 88 (2005).

[40] A. Yacoby et al., Phys. Stat. Sol. B **243**, 3593 (2006).

[41] H. Steinberg et al., Phys. Rev. B **73**, 113307 (2006).

[42] W. I. Friesen and B. Bergesen, J. Phys. C **72**, 045315 (2005).

[43] M. Casula, S. Sorella, and G. Senatore, Phys. Rev. B **74**, 245427 (2006).

[44] M. Casula and G. Senatore, ChemPhysChem **6**, 1902 (2005).

[45] M. P. Allen and D. J. Tildesley, *Computer simulation of liquids*, Clarendon, Oxford, 1987.

[46] J. D. Jackson, *Classical Electrodynamics*, Wiley, New York, 3rd edition, 1998.

[47] W. Häuseler and B. Kramer, Phys. Rev. B **47**, 16353 (1996).

[48] K. Jauregui, W. Häuseler, and B. Kramer, Europhys. Lett. **24**, 581 (1993).

[49] K. Jauregui, W. Häuseler, D. Weinmann, and B. Kramer, Phys. Rev. B **53**, R1713 (1996).

[50] F. Mila and K. Penc, J. Elec. Spectrosc. Rel. Phenom. , 451 (2001).

[51] G. Xianlong, M. Polini, R. Asgari, and M. P. Tosi, Phys. Rev. A **73**, 033609 (2006).

[52] N. Metropolis, A. E. Rosenbluth, M. N. Rosenbluth, and A., H. Teller, J. Chem. Phys. **21**, 1087 (1953).

[53] T. Gaskell, Proc. Phys. Soc. **77**, 1182 (1961).

[54] P. J. Reynolds, D. M. Ceperley, B. J. Alder, and W. A. Lester, J. Chem. Phys. **77**, 5593 (1982).

[55] C. J. Umrigar, M. P. Nightingale, and K. J. Runge, J. Chem. Phys. **99**, 2865 (1993).

[56] W. M. C. Foulkes, L. Mitas, R. J. Needs, and G. Rajagopal, Rev. Mod. Phys. **73**, 33 (2001).

[57] J. Moskowitz, K. Schmidt, M. Lee, and M. Kalos, J. Chem. Phys. **77**, 349 (1982).

[58] H. F. Trotter, Proc. Am. Math. Soc. **10**, 545 (1959).

[59] M. Suzuki, Commun. Math. Phys. **51**, 183 (1976).

[60] M. Casula, C. Filippi, and S. Sorella, Phys. Rev. Lett. **95**, 100201 (2005).

[61] D. F. B. ten Haaf, H. J. M. van Bemmel, J. M. J. van Leeuwen, W. van Saarloos, and D. M. Ceperley, Phys. Rev. B **51**, 13039 (1995).

[62] M. Calandra Buonaura and S. Sorella, Phys. Rev. B **57**, 11446 (1998).

[63] S. Sorella and L. Capriotti, Phys. Rev. B **61**, 2599 (2000).

[64] J. Anderson, J. Chem. Phys. **65**, 4121 (1976).

[65] D. M. Ceperley and B. J. Alder, J. Chem. Phys. **81**, 5833 (1984).

[66] D. M. Ceperley, J. Stat. Phys. **63**, 1237 (1991).

[67] K. X. Liu, M. H. Kalos, and G. V. Chester, Phys. Rev. Lett. **86**, 870 (2001).

[68] R. Assaraf, M. Caffarel, and A. Khelif, Phys. Rev. E **61**, 4566 (2000).

[69] S. Chiesa, D. M. Ceperley, R. M. Martin, and M. Holtzman, Phys. Rev. Lett. **97**, 076404 (2006).

[70] C. Lin, F. H. Zong, and D. M. Ceperley, Phys. Rev. E **64**, 016702 (2001).

[71] D. Bohm and D. Pines, Phys. Rev. **92**, 609 (1953).

[72] R. Jastrow, Phys. Rev. **98**, 1479 (1955).

[73] L. Calmels and A. Gold, Phys. Rev. B **56**, 1762 (1997).

[74] L. Calmels and A. Gold, Europhys. Lett. **39**, 539 (1997).

[75] P. Nozières and D. Pines, *The Theory of Quantum Liquids*, Perseus, Cambridge, MA, 3rd edition, 1999.

[76] M. Gell-Mann and K. A. Brueckner, Phys. Rev. **106**, 364 (1957).

[77] A. K. Rajagopal and J. C. Kimball, Phys. Rev. B **15**, 2819 (1977).

[78] S. Chesi and G. F. Giuliani, Phys. Rev. B **75**, 153306 (2007).

[79] Y. Wang and J. P. Perdew, Phys. Rev. B **43**, 8911 (1991).

[80] J. H. Jefferson and W. Häusler, Phys. Rev. B **54**, 4936 (1996).

[81] K. A. Matveev, Phys. Rev. B **70**, 245319 (2004).

[82] R. B. Griffiths, Phys. Rev. **133**, A768 (1964).

[83] L. Hulthen, Arkiv. Mat, Astron. Fysik. **26A**, 11 (1938).

[84] E. P. Wigner, Phys. Rev. **46**, 1002 (1934).

[85] L. I. Glazman, I. M. Ruzin, and B. I. Shklovskii, Phys. Rev. B **45**, 8454 (1992).

[86] T. Giamarchi and H. J. Schulz, Phys. Rev. B **39**, 4620 (1989).

[87] A. Gold and L. Calmels, Solid State Comm. **96**, 101 (1995).

[88] S. Yamamoto, Phys. Rev. Lett. **75**, 3348 (1995).

[89] D. M. Ceperley and B. Bernu, J. Chem. Phys. **89**, 6316 (1988).

[90] J. E. Vincent, J. Kim, and R. M. Martin, Phys. Rev. B **75**, 045302 (2007).

[91] A. J. Williamson, *Quantum Monte Carlo Calculations of Electronic Excitations*, PhD thesis, Robinson College, Cambridge, Cambridge, England, 1996.

[92] L. Mitas and R. M. Martin, Phys. Rev. Lett. **72**, 2438 (1994).

[93] D. Arnow, M. Kalos, M. Lee, and K. Schmidt, J. Chem. Phys. **77**, 5562 (1982).

[94] Y. Kwon, D. M. Ceperley, and R. M. Martin, Phys. Rev. B **53**, 7376 (1996).

[95] R. P. Feynman and M. Cohen, Phys. Rev. **102**, 1189 (1956).

[96] J. K. L. MacDonald, Phys. Rev. **43**, 830 (1933).

[97] G. Ortiz, D. M. Ceperley, and R. M. Martin, Phys. Rev. Lett. **71**, 2777 (1993).

[98] A. Gold and L. Calmels, Phys. Rev. B **58**, 3497 (1998).

[99] N. Iwamoto and D. Pines, Phys. Rev. B **29**, 3924 (1984).

[100] T. P. Smith, W. I. Wang, and P. J. Stiles, Phys. Rev. B **34**, 2995 (1986).

[101] V. Mosser, D. Weiss, K. von Klitzing, K. Ploog, and G. Weimann, Solid State Commun. **58**, 5 (1986).

[102] S. V. Kravchenko, V. M. Pudalov, and S. G. Semenchinsky, Phys. Lett. A **141**, 71 (1989).

[103] L. Latessa, A. Pecchia, A. Di Carlo, and P. Lugli, Phys. Rev. B **72**, 035455 (2005).

[104] D. J. Griffiths, *Introduction to Quantum Mechanics*, Prentice Hall, New Jersey, 1994.

[105] J. des Cloizeaux and J. J. Pearson, Phys. Rev. **128**, 2131 (1962).

[106] L. D. Faddeev and L. A. Takhtajan, Phys. Lett. A **85**, 375 (1981).

[107] A. D. Klironomos, R. R. Ramazashvili, and K. A. Matveev, Phys. Rev. B **72**, 195343 (2005).

[108] M. Fogler and E. Pivovarov, Phys. Rev. B **72**, 195344 (2005).

[109] M. Fogler and E. Pivovarov, J. Phys: Condens. Matter **18**, L7 (2006).

[110] A. Javey et al., Nat. Mater. **1**, 241 (2002).

[111] B. M. Kim et al., Appl. Phys. Lett. **84**, 1946 (2004).

[112] U. Zülicke, Science **295**, 810 (2002).

[113] B. Halperin, J. Appl. Phys. **101**, 081601 (2007).

[114] G. A. Fiete, J. Qian, Y. Tserkovnyak, and B. I. Halperin, Phys. Rev. B **72**, 045315 (2005).

[115] S. Sorella, Phys. Rev. B **64**, 024512 (2001).

[116] M. Casula, C. Attaccalite, and S. Sorella, J. Chem. Phys. **121**, 7710 (2004).

[117] W. Häusler and B. Kramer, Phys. Rev. B **47**, 16353 (1993).

[118] E. J. Mueller, Phys. Rev. B **72**, 075322 (2005).

[119] J. Moser et al., Phys. Rev. B **74**, 193307 (2006).

Author's Biography

Luke Shulenburger was born in Lawrence, KS on December 18, 1979. He received Bachelor of Science degrees in Physics and Mathematics from the Massachusetts institute of Technology in 2002 under the guidance of Dr. Nicola Marzari. Luke pursued his graduate physics studies at the University of Illinois at Urbana-Champaign. In collaboration with Dr. Richard M. Martin, his doctoral advisor, and Dr. Michele Casula he worked on the electronic structure of the quasi one dimensional electron gas. He received his M. S. in Physics from the University of Illinois in 2004.